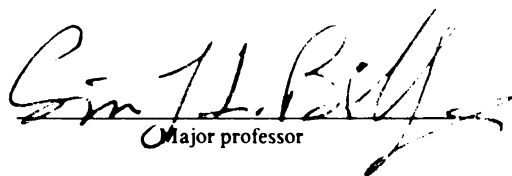This is to certify that the

dissertation entitled

LOCAL STRUCTURE AND DYNAMICS OF III-V SEMICONDUCTOR ALLOYS
BY HIGH RESOLUTION X-RAY PAIR DISTRIBUTION FUNCTION ANALYSIS

presented by

IL-KYOUNG JEONG

has been accepted towards fulfillment
of the requirements for

Ph.D. degree in Physics and Astronomy

Major professor

Date 02/12/01

PLACE IN RETURN BOX to remove this checkout from your record.
TO AVOID FINES return on or before date due.
MAY BE RECALLED with earlier due date if requested.

DATE DUE	DATE DUE	DATE DUE

LOCAL STRUCTURE AND DYNAMICS OF III-V SEMICONDUCTOR ALLOYS

BY HIGH RESOLUTION X-RAY PAIR DISTRIBUTION FUNCTION ANALYSIS

By

IL-KYOUNG JEONG

A DISSERTATION

Submitted to
Michigan State University
in partial fulfillment of the requirements
for the degree of

DOCTOR OF PHILOSOPHY

DEPARTMENT OF PHYSICS AND ASTRONOMY

2001

ABSTRACT

LOCAL STRUCTURE AND DYNAMICS OF III-V SEMICONDUCTOR ALLOYS
BY HIGH RESOLUTION X-RAY PAIR DISTRIBUTION FUNCTION ANALYSIS

By

IL-KYOUNG JEONG

In semiconductor alloys such as $In_{1-x}Ga_xAs$, the energy band gap as well as
the lattice parameter can be engineered by changing the concentration, x. Due to
these properties, semiconductor alloys have found wide applications in optoelectronic
devices. In these alloys, local structure information is of fundamental importance in
understanding the physical properties such as band structure.

Using the high real-space resolution atomic Pair Distribution Function, we ob-
tained more complete structural information such as bond length, bond length dis-
tributions, and far-neighbor distances and distributions. From such experimental
information and the Kirkwood model we studied both local static displacements and
correlations in the displacements of atoms. The 3-dimensional As and (In,Ga) atom
iso-probability surfaces were obtained from the supercell relaxed using the Kirkwood
potential. This shows that the As atom displacements are very directional and can
be represented as a combination of $\langle 100 \rangle$ and $\langle 111 \rangle$ displacements. On the contrary,
the (In,Ga) atom displacements are more or less isotropic. In addition, the single
crystal diffuse scattering calculation of the relaxed supercell shows that the atomic
displacements are correlated over longer range along [110] directions although the
displacements of As atoms are along $\langle 100 \rangle$ and $\langle 111 \rangle$ directions.

Besides the local static displacements, we studied correlations in thermal atomic
motions of atom pairs from the PDF peak width changes as a function of atom pair

distance. In the PDF the near-neighbor peaks are sharper than those of far-neighbors due to the correlation in near-neighbor thermal motions. We also determined bond stretching and bond bending force constants of semiconductor compounds by fitting the nearest neighbor and far-neighbor peak widths to the lattice dynamic calculations using the Kirkwood model.

To my family, my wife Eunhee and daughter Haein

ACKNOWLEDGMENTS

Contents

List of Tables

List of Figures

Chapter 1

Introduction and Motivation

1.1 Introduction

The discovery of semiconductors has brought significant advances in modern technologies. From the elemental semiconductors to the semiconductor compounds, these materials have been used in computers, telecommunications and optical devices [1]. Recently, semiconductor alloys, in which electronic structure and material properties can be controlled, have found wide applications in optoelectronic devices. As in other interesting materials such as colossal magnetoresistance materials and high T_c superconductors, local structure information is very important in understanding the physical properties of semiconductor alloys. In pseudobinary semiconductor alloys ($A_{1-x}B_xC$), the electronic structure as well as their enthalpies of formation are strongly affected by the change of concentration, x. These examples show that the local structural information is one of the key parameters in understanding physical properties of these materials. In these disordered semiconductor alloys, however, the local structure is very different from the average structure, which is determined from the Rietveld analysis of powder diffraction pattern.

Besides local static displacements of atoms, thermal atomic motions are important in understanding structural phase transitions [2, 3] and carry information about the

interatomic potential in a crystal. The most detailed information about thermal atomic motions can be obtained from inelastic neutron scattering [4]. Using suitable models for the interatomic interactions, the force constants can be determined by fitting a lattice dynamic model to the experimental phonon dispersion relations.

One of the ways to study the local atomic structure as well as the thermal atomic motions in a crystal is the total scattering powder diffraction measurement. Here the total scattering means 'Bragg peaks + diffuse scattering'. Although directional information is lost, it is still possible to extract significant information about local structure [5]. In powder diffraction, diffuse scattering is evident especially in high-Q space. One way to extract the information stored in the diffuse scattering is to obtain the atomic pair distribution function (PDF) via a sine Fourier transform of total scattering data [6]. The resultant PDF is a measure of the probability of finding atoms at a distance r from a reference atom: PDF peak positions measure pair separations, the areas under the peaks give the coordination numbers and PDF peak widths measure bond-length distributions (static and thermal). Therefore, from the PDF analysis, it is possible to obtain both local structural information as well as thermal atomic motion.

In this dissertation, we present the application of PDF analysis to the local structure of $In_xGa_{1-x}As$ semiconductor alloys and correlated atomic motion in semiconductor compounds.

1.2 Properties of Semiconductors

Semiconductors are one of the actively studied subjects and many reviews and useful textbooks are available about semiconductors [7, 8, 9, 10] and semiconductor alloys [11, 12]. Here we briefly review some of the semiconductor properties related

to the structure. The energy band gap, E_g, between the lowest point of the conduction band (conduction band edge) and the highest point of the valence band (valence band edge) is a useful concept in understanding conductivity in a material. At T=0, a material with an energy gap will be nonconducting unless the applied field is strong enough to overcome the energy gap. However, at T$\neq$0, there are some probabilities that electrons will be thermally excited across the energy gap into the conduction bands. This probability critically depends on the size of the energy gap and is roughly of order $e^{-E_g/2k_BT}$ where k_B is the Boltzman's constant. At room temperature k_BT is around 0.025 eV; therefore, depending on the energy gap, E_g, some electrons can be excited over the energy gap and observable conduction will occur at room temperature.

Semiconductors are generally classified by their energy band gaps with values around 0.1~2 eV at room temperature. Depending on the size of the energy gap, semiconductors can emit from infrared to blue lights. The energy band gap can be either direct or indirect. In direct gap semiconductors, the conduction band edge occurs at the same point in k-space as the valence band edge, whereas in indirect gap cases the band edges occur at different points in k-space. GaAs is an example of a direct band gap semiconductor and silicon is an example of an indirect band gap semiconductor. In indirect gap semiconductors, the efficiency of light emission is not as good as in direct gap semiconductors since the transition requires emission or absorption of a phonon to conserve crystal momentum.

One of the most important parameters of semiconductors at temperature T is the number of carrier densities: electron or hole densities. In intrinsic semiconductors where impurity contributions are negligible, all carriers come from thermal excitations and electron density is equal to hole density. In extrinsic semiconductors, impurities

contribute a significant fraction of the carrier density. In this case, electron density is not equal to the hole density. Thus when impurities provide the major source of carriers, one or the other type of carrier will be dominant. An extrinsic semiconductor is called "n-type" or "p-type", according to whether the dominant carriers type are electrons or holes, respectively.

Silicon and germanium are the most important semiconductors. These semiconductors have perfect covalent bonding. In addition to the column IV elemental semiconductors, compounds made up of elements from columns III and V of the periodic table form III-V semiconductors. GaAs and InAs are examples. In III-V semiconductors, some electron transfer occurs between the two types of atoms. This uneven electron distribution increases the Coulomb interaction between the ions. The contribution of ionic character in the bond can be represented using the fractional ionic character, f_i [7]. Most III-V compounds have f_i around $0.2 \sim 0.4$. This ionicity becomes even larger and more important in the II-VI compounds. In the II-VI compounds, the ionicities are in the range of $0.6 \sim 0.8$ and the bonding between atoms is a strong ionic as well as a covalent. For this reason, III-V and II-VI semiconductors are referred to as polar. They are known as polar semiconductors.

1.2.1 Structure of Semiconductors

Most semiconductors crystallize in diamond, zincblende, and wurtzite structures. As shown in Figure 1.1(a), the diamond structure consists of two interpenetrating face-centered cubic (fcc) sublattices displaced by $a/4(\hat{x}, \hat{y}, \hat{z})$, where a is the lattice constant and $\hat{x}, \hat{y}, \hat{z}$ are the unit vectors along x, y, z axes. The diamond lattice is not a Bravais lattice. The underlying Bravais lattice is the fcc lattice and the diamond structure is obtained with the two-atom basis $(0,0,0)$ and $a/4(\hat{x}, \hat{y}, \hat{z})$. In the diamond structure, each atom has four nearest neighbor atoms, forming a tetrahedron.
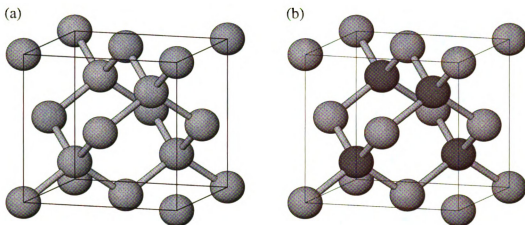
Figure 1.1: (a) Diamond structure, (b) zincblende structure. In the zincblende structure, anions occupy one sublattice and cations the other.

Most column IV elements, C, Si, Ge, α-Sn, of the periodic table have this structure. The zincblende structure has the same lattice as the diamond structure. However, in this case, the anions occupy one sublattice and the cation the other. Many important III-V and II-VI semiconductor compounds such as GaAs and CdTe have this structure.

The wurtzite structure (Figure 1.2(a)) is a variation of the zincblende structure. Both structures are tetrahedrally coordinated and the cohesive energy of the wurtzite structure is very close to that of the zincblende structure [8]. As a result some III-V and II-VI compounds crystallize in both the zincblende and the wurtzite structures. In the wurtzite structure, the underlying Bravais lattice is a hexagonal. It is interesting to note that only a few crystals among the III-V compounds crystallize in the wurtzite structure as a stable phase. This is in clear contrast to the II-VI counterparts where about half have the wurtzite structure. This is strongly related to the higher ionicity of II-VI compounds [13]. These diamond, zincblende and wurtzite structures become unstable under the high pressure and a phase transition to β-Sn or NaCl structure
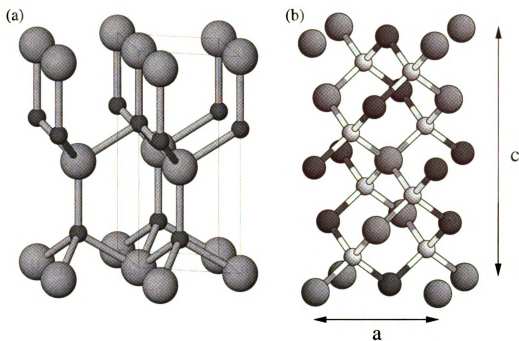
Figure 1.2: (a) Wurtzite structure, (b) Chalcopyrite structure.

occurs depending on the ionicity [14].

Another crystal structure closely related to the semiconductors is a chalcopyrite structure [15, 16]. This structure is found in ordered ternary compounds such as $CdGeAs_2$ (ABX_2). As shown in Figure 1.2(b), the chalcopyrite structure is similar to the zincblende structure. It has nearly the same anion arrangement as the zincblende structure but has two cations arranged periodically on one of the sublattices. In the 'ideal chalcopyrite' structure, the ratio of the unit cell lengths c to a is equal to two. However, in most real chalcopyrite crystals, the ratio c/a is less than two by as much as 12%. In general cases, the structure has a tetragonal symmetry and the anions are displaced from their fcc sites along (100) or (010) directions. The anion displacements result in two different bond lengths $R_{AX} \neq R_{BX}$. This is very similar to the bond alternation in $In_xGa_{1-x}As$ alloys. Therefore the chalcopyrite structure has been used to explain the local atomic displacements in $In_{0.5}Ga_{0.5}As$ alloy [15].

6

1.2.2 Pure Semiconductors

Silicon and Germanium are the prototype of a large class of semiconductors. The crystal structure of Si and Ge is the diamond structure. Both Si and Ge have indirect band gaps. Thus the optical absorption and emission of Si is much weaker than a direct band gap material such as GaAs. However, Si is the material of choice for photodetection because of the high quantum efficiency, high degree of uniformity, well established technology and low price.

1.2.3 Semiconductor Compounds

Semiconductor compounds made from the elements of the groups III and V (GaAs) or II and VI (ZnTe) of the periodic table have properties very similar to the elemental semiconductors. Most III-V compounds crystallize in the cubic zincblende structure though the wide band gap nitride (GaN, InN) have the hexagonal wurtzite structures. In II-VI compounds, some crystals like ZnS and CdS have both zincblende and wurtzite structure as stable phases. Many of the III-V compounds have direct band gaps that facilitate an optical emission process [17]. Therefore, III-V compounds have been used in light emitting devices (LED) and lasers [1]. GaAs also has better properties in electron saturation velocity and electron mobility than those of Si. However, it is not widely used in computer chips because of the low cost of Si.

The energy band gap of II-VI compounds covers wide ranges from few meV to a few eV. Wide band gap II-VI compounds such as ZnSe are used in lasers and LEDs, while narrow band gap compounds such as CdTe are used in solar cells, optical devices, and infrared detector and emitters [17].
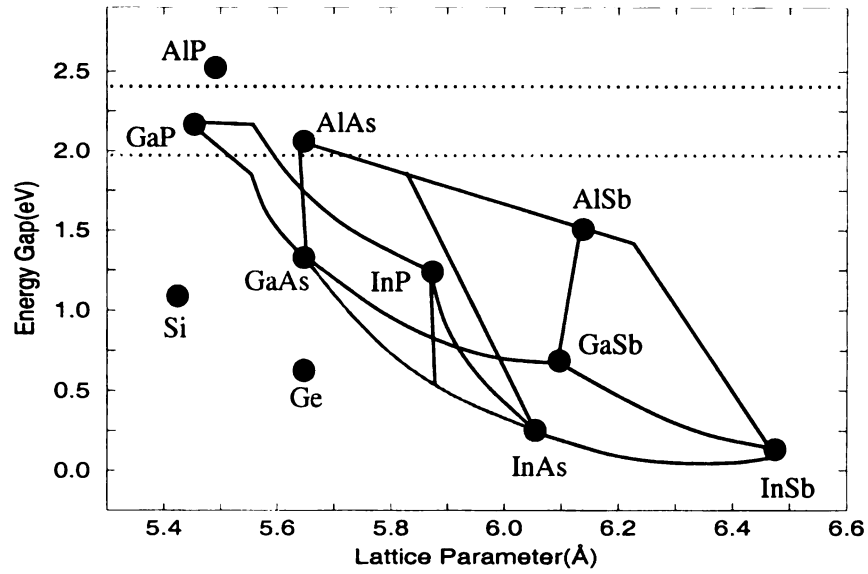
Figure 1.3: A plot of the energy gap as a function of the lattice parameter for several III-V semiconductors. The lines that connect points on the graph show how the band gap and the lattice parameter vary for mixtures of the binary compounds and for the quaternary compounds to which the points correspond [18].

1.2.4 Semiconductor Alloys

By mixing two binary semiconductor compounds or two elemental semiconductors, it is possible to make semiconductor alloys. In these alloys, the energy band gap as well as the lattice parameter can be engineered by changing the concentration as shown in Figure 1.3. This opens up many new applications [18, 19]. For example, GaAs electronic integrated circuits are dominant in optoelectronic applications. However, GaAs generates light near 0.88 μm in the near infrared and the optical loss of optical fiber is minimum at the wavelength of λ=1.5 μm. This wavelength is achievable from GaAs-InAs or InP-GaAs alloys by choosing an optimum concentration [12]. The Si-Ge alloy is an another example. By adding Ge to Si, it is possible to improve the mobilities of the charge carrier and design electronic devices which are faster than Si [19].
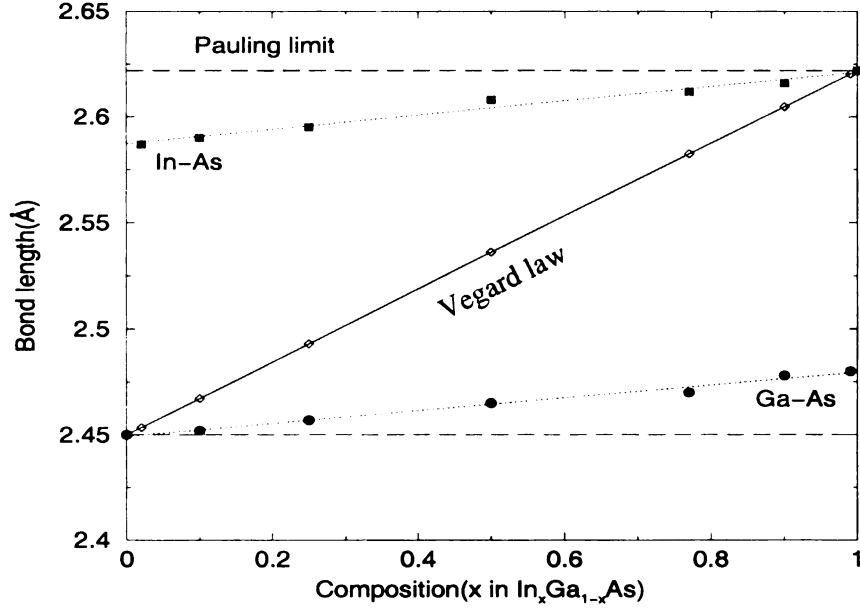
Figure 1.4: Composition dependence of the bond lengths in $In_xGa_{1-x}As$ alloys [25]. Also shown are bond lengths in Pauling and Vegard limits. See text for details.

In the alloys, however, due to the presence of disorder, the band structure calculations based on the average crystal structure do not work and the local structure should be taken into account to obtain accurate electronic structure determinations [20, 21]. In $A_{1-x}B_xC$ pseudobinary alloys, two possibilities concerning the composition dependence of the bond lengths $d_{AC}(x)$ and $d_{BC}(x)$ in an alloy are suggested. First, the atomic radii are considered as conserved quantities and, hence, are transferable [22, 23] between materials. Based on this idea ("Pauling limit"), bond lengths $d_{AC}(x)$ and $d_{BC}(x)$ in the alloys are assumed to be composition independent. However, many x-ray diffraction experiments on semiconductor [24] alloys showed that the average structure is preserved in the alloys and the lattice parameter is given by the composition weighted average of the pure end-members ("Vegard law"). In the Pauling limit, the structure is assumed to be very floppy and complete relaxation occurs. Therefore, in this limit, two distinct bond lengths exist in an alloy. Conversely, in the Vegard
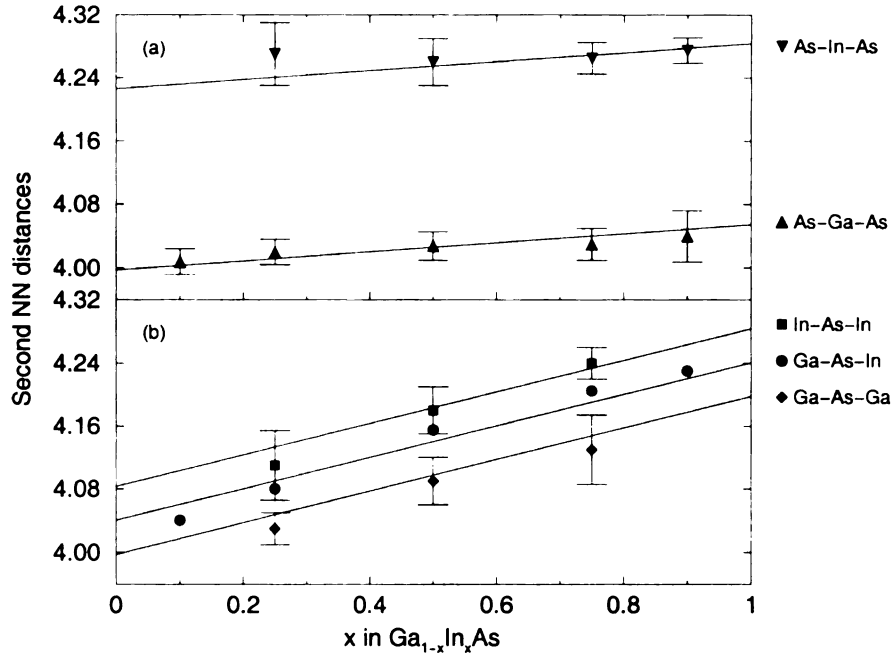
Figure 1.5: Symbols are EXAFS experimental data [15] and solid lines [26] are corresponding theoretical calculations based on Kirkwood potential. (a) As-As second-neighbor distances. As-In-As bond (triangle down), As-Ga-As bond (triangle up). (b) In-As-In (square), Ga-As-In (circle), and Ga-As-Ga (diamond) second-neighbor distances.

limit, the lattice is rigid and no relaxation occurs, hence the alloy has only a single average bond length.

The first experimental determination of bond lengths in $In_xGa_{1-x}As$ alloys is made by Mikkelson and Boyce [25]. Figure 1.4 shows the composition dependence of bond lengths in $In_xGa_{1-x}As$ alloys obtained using the extended x-ray absorption fine structure (XAFS) method [25]. As shown, the individual nearest neighbor (NN) Ga-As and In-As distances in the alloys are rather closer to the pure Ga-As and In-As distances. In addition, it shows that the local bond lengths differ from the average bond length by as much as 0.1 Å. Figure 1.5 shows the second-neighbor distances in the $In_xGa_{1-x}As$ alloys. The As-As second-neighbor distances have two distinct bond lengths; the As-In-As bond (closed squares) is longer than the As-Ga-As bond (closed

10

circles). It also shows that the As-As bond distances are almost completely relaxed. However, In-In, Ga-Ga, and Ga-In distances are closer to the composition weighted average value. Further XAFS experiments showed that this is quite general behavior for many zincblende type alloy systems [27, 28, 29]. However, the XAFS information is limited to the nearest and next nearest neighbor distances and no bond-length distribution is available. This limited information makes it difficult to establish in detail how the alloys accommodate the local distortions due to the alloying.

1.2.5 Modeling of Semiconductor Alloy Structures

One of the simple and useful phenomenological models of semiconductors is the Valence force filed (VFF) model [12]. The most common forms of VFF are the Keating and Kirkwood models. The Keating and Kirkwood potentials are very similar to each other. These VFF potentials depend on only two parameters: the bond stretching and bond bending force constants. The following shows the Kirkwood potential:

$$V = \sum_{<ij>} \frac{\alpha_{ij}}{2} \left(L_{ij} - L_{ij}^o\right)^2 + L_e^2 \sum_{<ij,ik>} \frac{\beta_{ijk}}{8} \left(cos\theta_{ijk} + \frac{1}{3}\right)^2. \tag{1.1}$$

Here L_{ij} is the bond length between atoms i and j, L_{ij}^0 is the natural bond-length, and L_e is the average bond length given by Vegard's law. The potential contains bond stretching force constants α_{ij} and bond bending force constant β_{ijk} that couple to the change in the angle θ_{ijk} between adjacent nearest neighbor bonds. Under a uniform expansion, these force constants have a simple relationship to the elastic constants of cubic crystals [30],

$$
\begin{aligned}
B &= \frac{1}{3a}(C_{11} + 2C_{12} \\
C_{11} &= \frac{1}{3a}\left[\alpha + 8/3\beta\right] \\
C_{12} &= \frac{1}{3a}\left[\alpha - 4/3\beta\right] \\
C_{44} &= \frac{1}{3a}\left[\frac{4\alpha\beta}{\alpha + \beta + 7\beta/9}\right].
\end{aligned}
\tag{1.2}
$$

Here C_{11}, C_{12}, and C_{44} are the elastic constants, B is the bulk modulus and a is the lattice constant. The force constants in the Kirkwood model can be determined to fit either the elastic constant C_{11} and the bulk modulus $B = 1/3(C_{11} + 2C_{12})$ or to fit C_{11} and C_{12}. However, the force constants chosen to fit C_{11} and B result in errors in C_{44} and the zone center optic phonon frequency around 15 % $\sim$ 30 % for most semiconductor compounds [26] and vice versa.

Using the Kirkwood model, the rigidity of the $A_{1-x}B_xC$ semiconductor alloy can be determined using a topological rigidity parameter, a^{**} [26], which can be fit by the following function:

$$a^{**} = \frac{1 + 1.25(\beta/\alpha)}{1 + 3.6(\beta/\alpha) + 1.17(\beta/\alpha)^2}. \tag{1.3}$$

The topological rigidity parameter, a^{**} depends on the ratio of the β and α. It can vary from 0 to 1. $a^{**}=1$ corresponds to the floppy structure (Pauling limit) and $a^{**}=0$ to the rigid structure (Vegard limit). The ratio of β_{AC}/α_{AC} is around 0.2 in most III-V compounds and 0.1 in II-VI compounds. Therefore II-VI compounds ($a^{**} \sim 0.8$) are expected to be more floppy than III-V compounds ($a^{**} \sim 0.7$). And the slopes of the composition dependence of NN bond lengths are flatter in II-VI compounds.

1.3 Measuring Correlated Thermal Motion

A familiar effect of thermal motions of atoms is the reduction of x-ray scattering intensities. The decrease in the intensities is represented by e^{-2W} where W is the Debye-Waller factor, given as $W = 8\pi^2 \bar{u}_s^2 \sin^2\theta/\lambda^2$. Here $\bar{u}_s^2$ is the mean-square displacement of a lattice point in a direction perpendicular to the reflection planes, 2θ is the scattering angle, λ is the incident x-ray wavelength. Therefore from the decrease of x-ray intensities as a function of scattering angle, the $\bar{u}_s^2$ which measures uncorrelated thermal motion (Figure 1.6(a)), can be determined.
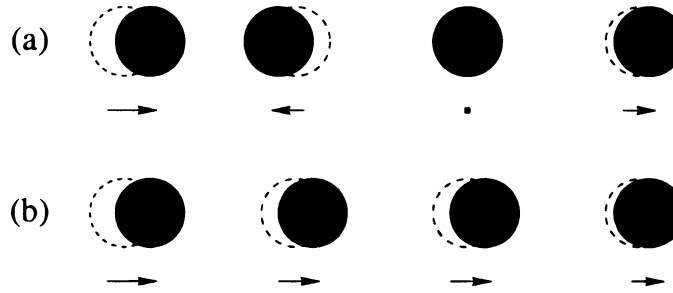
Figure 1.6: Schematic representation of (a) uncorrelated and (b) correlated thermal motions of atoms.

However, atoms in a crystal are coupled together by the interatomic forces and the atomic motions are correlated (Figure 1.6(b)). In general, near-neighbor atoms tend to move in-phase with each other and far-neighbors move independently. This coupling of the atomic motion results in diffuse scattering and provides information about the interatomic forces. For example, atomic motions in a covalently bonded material will be more strongly correlated than those in a metallic bond system. In addition, the degree of correlation will be different depending on atom separation as well as pair direction [31]. Therefore, from the details of correlated atomic motion, it is possible to determine empirical interatomic potential parameters.

Since PDF peak widths measure mean-square relative displacements of an atom pair, their width gives information about the correlation in atomic motions. If the motion is completely correlated, the peak should be given by a delta-function. And for the completely independent relative motions, the PDF peak will be broad and the width is given by the mean-square displacements of atom pairs. Therefore, the analysis of PDF peak width as a function of atom separation gives information about the degree of correlation between atoms [32, 33]. For example, the nearest neighbor PDF peak width depends primarily on the bond stretching force and the far-neighbor peak width is determined by the bond bending force.

13

1.4 PDF Analysis

In the pure crystalline material, all the structural information are contained in a unit cell and can be extracted using Rietveld-type refinement of diffraction patterns. However, for non-crystalline materials, such an approach does not work due to the lack of periodicity. The atomic pair distribution function has long been used to characterize the structure and properties of non-crystalline materials such as liquids, glasses and amorphous materials. Nice introduction to the PDF method and its application to the non-crystalline materials are given by many authors [34, 35, 36, 37, 38]. The atomic pair distribution function measures the probability of finding another atom at a distance r from the reference atom. Therefore, the PDF provides important information about structure of materials such as bond length and bond length distributions. Besides the total PDF, differential PDFs have been used to obtain chemical specific structural information [38]. Application of PDF analysis to crystalline materials has been relatively recent. The use of the PDF technique to the crystalline materials has been described in a number of recent publications [39, 40]. In the case of disordered crystalline materials, obtaining high real-space resolution PDF is very important in order to obtain local structural information [41, 42, 43]. The real-space resolution of PDF is mainly determined by the maximum momentum transfer, Q_{max}. And it is necessary to collect data up to $Q_{max} \simeq 40 \text{\AA}^{-1}$ to obtain reasonable real-space resolution. However, in conventional x-ray scattering the maximum obtainable Q_{max} is around 20 $\text{\AA}^{-1}$ [37] limiting the real-space resolution. In addition, the scattering intensity is very weak in high-Q region due to the atomic scattering factor. These limitations in the conventional x-ray are overcome with the high energy high intensity synchrotron x-rays and pulsed neutron sources. In particular, the advent of the third generation synchrotron radiation make it possible to collect data beyond $Q_{max}=40\text{\AA}^{-1}$. In order

to use the high energy synchrotron x-rays to the PDF analysis and to study the local structure of disordered crystalline materials, we developed high energy x-ray PDF technique and data analysis program. The high real-space resolution PDFs allowed us to obtain information on the local structure of the $In_xGa_{1-x}As$ semiconductor alloys. The details of the high energy x-ray PDF technique are discussed in Chapter 2 and Appendix A.

1.5   Layout of Dissertation

In Chapter 2, we discussed the high energy x-ray PDF technique. The general introduction to the PDF is given in Section 2.2 and the details of data analysis procedures is described in Section 2.3. The application of the PDF method to correlated atomic motions in semiconductor compounds is discussed in Chapter 3. In Section 3.4 we compared correlated thermal motions of atoms in two different interatomic force systems: Ni and InAs. The experiments are compared to the lattice dynamical calculations using the Kirkwood potential. Also, we discussed the possibility of obtaining the interatomic force constants from the PDF. The Correlated Debye model of thermal motions is given in Section 3.5, The application of PDF method to the $In_xGa_{1-x}As$ alloys is described in Chapter 4. In Section 4.2 we present the first complete solution of the distorted local structure of the important III-V semiconductor alloy system $In_{1-x}Ga_xAs$ using the PDF analysis of powder diffraction data. The modeling of the local structure of $In_xGa_{1-x}As$ alloys are given in Section 4.3. And the correlations in static displacements of atoms are described in Section 4.4. Finally, the summary and discussion is given in Chapter 5.

Chapter 2

Atomic Pair Distribution Function from x-ray Powder Diffraction

2.1   Introduction

X-ray diffraction has long been used to characterize the structure of a crystalline material [44]. By analyzing the intensities and positions of the Bragg peaks, one can obtain the average structure information of a crystal using Rietveld-type refinement method [45]. The success of Bragg law and crystallographic methods is based on the three dimensional periodicity of a crystalline material. Therefore, for a material with disorder (local deviation from the average structure), the crystallographic methods do not reveal the local structural information properly. Any deviation from a strict long-range order gives rise to diffuse scattering. Therefore, in order to obtain the local structural information, one has to analyze diffuse scattering [46]. Diffuse scattering due to local disorder is relatively weak compared to Bragg diffraction and widely spread in reciprocal space. This often makes the diffuse scattering experiments on single crystal intensity-limited and very time-consuming [47]. An alternative way to study diffuse scattering is powder diffraction. Although directional information is lost, it is still possible to extract significant information about local structure [5]. In conventional crystallographic method, only Bragg peaks are used for the refine-

ment and data are usually terminated around $Q = 14$ Å^{-1} due to the overlap of the Bragg peaks beyond this value. However, for a disordered material, high-Q space contains significant information of local structure as a form of diffuse scattering [6]. The information stored in high-Q space cannot be extracted by the crystallographic method. One way to extract information stored in the diffuse scattering is to obtain the atomic pair distribution function (PDF) via a sine Fourier transform of the diffraction data [6].

The atomic pair distribution function (PDF) has long been used for the study of amorphous materials, glasses, and liquids [34]. Its widespread application to crystalline materials such as semiconductor alloys is relatively recent [48]. In Section 2.2 we briefly review the formalism of PDF and it's characteristics. In Section 2.3, we give a short introduction to synchrotron radiation. And then the data collection and analysis procedures are described.

2.2 Atomic Pair Distribution Function

In x-ray diffraction experiments, the quantity measured is the scattered intensity of x-rays. This intensity from a material can be represented in the following way:

$$
\begin{aligned}
I_{eu}(Q) &= \left| \sum_m f_m e^{i(\mathbf{k}' - \mathbf{k}) \cdot \mathbf{r_m}} \right|^2 \\
&= \sum_m f_m e^{i(\mathbf{k}' - \mathbf{k}) \cdot \mathbf{r_m}} \sum_n f_n{}^* e^{-i(\mathbf{k}' - \mathbf{k}) \cdot \mathbf{r_n}} \qquad (2.1) \\
&= \sum_{m,n} f_m f_n{}^* e^{i(\mathbf{k}' - \mathbf{k}) \cdot \mathbf{r_{mn}}},
\end{aligned}
$$

where f_m, f_n are the atomic scattering factors of atom m, n and '*' represents a complex conjugate. $\mathbf{k}, \mathbf{k}'$ are wavevectors of the incident and scattered x-rays and $\mathbf{r_{mn}} = \mathbf{r_m} - \mathbf{r_n}$ is the vector connecting atoms, m and n. For powder samples, we

17
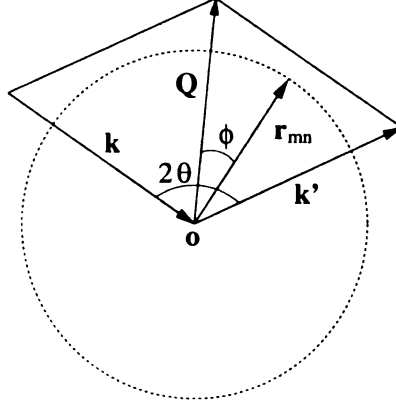
Figure 2.1: Illustration of the scattering event in the powder sample. The dotted circle shows possible positions of $\mathbf{r_{mn}}$ in powder sample.

can assume that the vector $\mathbf{r_{mn}}$ may have the equal probabilities in all directions as is shown in Figure 2.1. In this case, we can take a spatial average of the exponential term in Eq. 2.2 and obtain what is known as the Debye [49] scattering equation,

$$I_{eu}(Q) = \sum_{m,n} f_m f_n \frac{\sin Q r_{mn}}{Q r_{mn}}, \tag{2.2}$$

where $Q = |\mathbf{k}' - \mathbf{k}| = \frac{4\pi}{\lambda} \sin \theta$. Here 2θ is the angle between $\mathbf{k}'$ and $\mathbf{k}$. It is useful to introduce a density function, $\rho_m(r_{mn})$ such that $\rho_m(r_{mn})dV_n$ gives the number of atoms in the volume element dV_n at a distance r_{mn} from atom m. Using the density function $\rho_m(r_{mn})$, for a monoatomic material, Eq. 2.2 can be expressed as the following:

$$I_{eu}(Q) = \sum_m f^2 + \sum_m f^2 \int \rho_m(r_{mn}) \frac{\sin Q r_{mn}}{Q r_{mn}} dV_n. \tag{2.3}$$

For an atom pair distance, $r_{mn} = r$, let $\rho(r) = \langle \rho_m(r_{mn}) \rangle$, where $\langle \cdots \rangle$ means the average over all atoms, m at a distance r from an atom in the sample. Then, adding and subtracting the average density, ρ_o, we can rewrite Eq. 2.3 as

$$I_{eu}(Q) = \sum_m f^2 + \sum_m f^2 \int 4\pi r^2 [\rho(r) - \rho_o] \frac{\sin Qr}{Qr} dr + \sum_m f^2 \int 4\pi r^2 \rho_o \frac{\sin Qr}{Qr} dr. \tag{2.4}$$

The third term of Eq. 2.4 is the self scattering and is finite only at small angles close to the primary beam and can be neglected [36]. Therefore we drop this term here,

then we have

$$I(Q)_{eu} = Nf^2 + Nf^2 \int_0^\infty 4\pi r^2 \left[\rho(r) - \rho_o\right] \frac{\sin Qr}{Qr} \, dr, \qquad (2.5)$$

where N is the total number of scattering atoms in the sample. We can rearrange Eq. 2.5 to have the simple form of

$$Q\left[S(Q) - 1\right] = \int_o^\infty 4\pi r \left[\rho(r) - \rho_o\right] \sin Qr \, dr, \qquad (2.6)$$

where $S(Q)$ is the 'total scattering structure function' defined as $S(Q) = I(Q)_{eu}/Nf^2$. For a polyatomic material, $S(Q)$ can be generalized to have $S(Q) = [I(Q)_{eu}/N - (\langle f^2 \rangle - \langle f \rangle^2)]/\langle f \rangle^2$ [34, 35, 36]. In Eq. 2.6, if we define 'atomic pair distribution function', $G(r)$ as $G(r) = 4\pi r[\rho(r) - \rho_o]$, then we can obtain $G(r)$ from the inverse sine Fourier transform of the experimental reduced total structure function, $F(Q) = Q[S(Q) - 1]$,

$$G(r) = \frac{2}{\pi} \int_o^\infty Q[S(Q) - 1] \sin Qr \, dQ. \qquad (2.7)$$

In a real experiment, the upper limit of the integration in Eq. 2.7 is not infinity but the maximum measured magnitude of momentum transfer, Q_{max}. If we consider this finite Q_{max} effect (termination effect), the experimental PDF will be given by the convolution of the PDF obtained with $Q_{max} = \infty$ by the Sinc function [50],

$$G_{exp}(r) = \frac{1}{\pi} \int_0^\infty G(r') \left[\frac{\sin Q_{max}(r - r')}{r - r'} - \frac{\sin Q_{max}(r + r')}{r + r'}\right] dr', \qquad (2.8)$$

where, $G(r)$ is the PDF obtained with $Q_{max} = \infty$ and $G_{exp}(r)$ is the experimentally determined PDF. The effect of convolution with finite Q_{max} is clearly shown in Figure 2.2. This Figure shows the nearest neighbor peak of $In_{0.5}Ga_{0.5}As$ PDF with different Q_{max}. This peak is a doublet made up of two closely separated peaks. With Q_{max} higher than 40Å^{-1}, the two components are well resolved. However, for Q_{max} around 30Å^{-1}, the splitting is not clear and only a shoulder is noticeable. This shows that the larger Q_{max}, the higher is the real-space resolution.

19
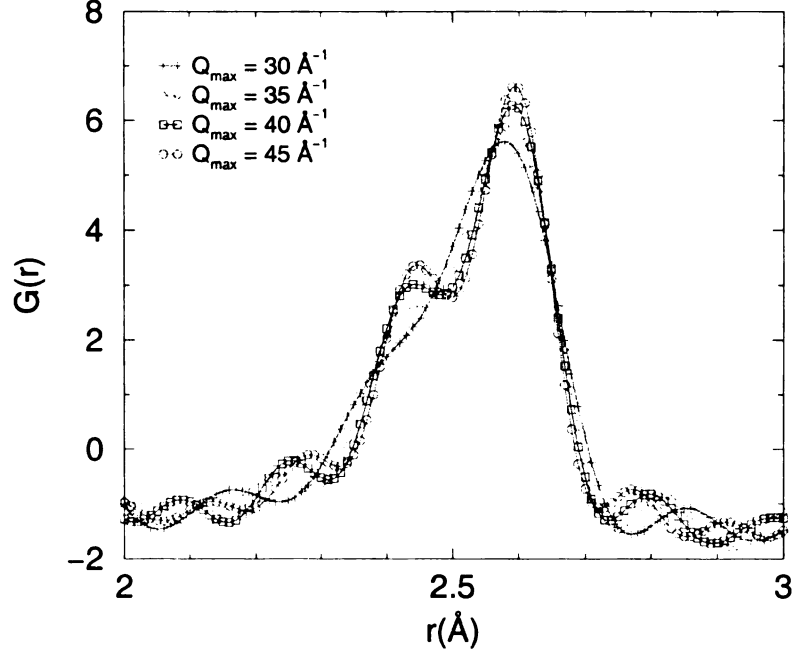
Figure 2.2: Real-space resolution of $In_{0.5}Ga_{0.5}As$ NN PDF peak. Symbols show NN PDF peak obtained with different Q_{max} . (plus) $Q_{max}=30Å^{-1}$, (diamond) $Q_{max}=35Å^{-1}$, (square) $Q_{max}=40Å^{-1}$, and (circle) $Q_{max}=45Å^{-1}$.

In N-component materials, the total scattering structure function, S(Q) is given by the weighted sum of the N(N+1)/2 partial structure functions, $S_{mn}(Q)$:

$$S(Q) = \sum_{m,n} \omega_{mn} S_{mn}(Q), \tag{2.9}$$

where $S_{mn}(Q)$ is a partial structure function and $\omega_{mn} = c_m c_n f_m f_n^*/\langle f \rangle$, c_m, c_n are concentration of atom type m and n. Partial structure functions contain chemical specific information involving element pair (m,n) and differential structure function yields an element resolved structural information. Therefore, the corresponding PDF of total structure function is a weighted average of partial pair distribution functions. When the difference in bond lengths between atom pairs is very small, they cannot be resolved in the total PDF making determination of bond lengths between specific atom pairs very difficult. In this case, having partial and/or differential PDFs helps to obtain specific bond length information. Chemical specific partial and differential
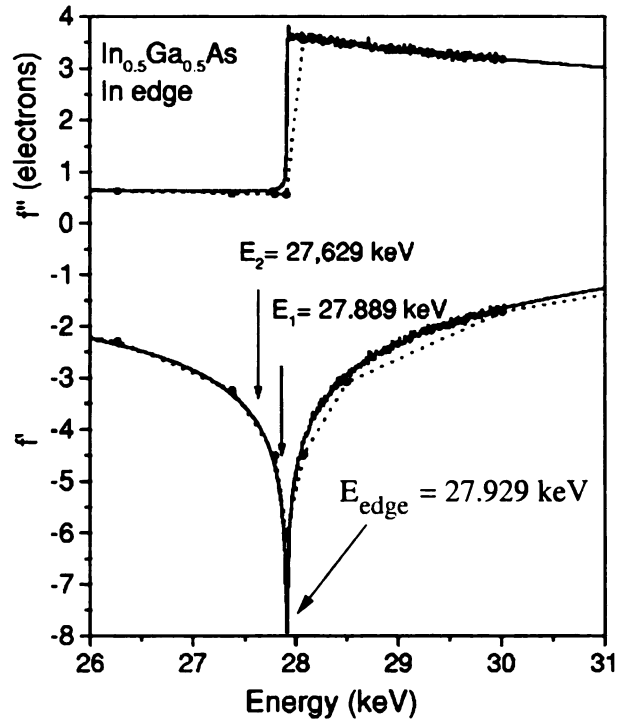
Figure 2.3: Energy dependence of the anomalous scattering of indium [51]. Symbols: theoretical data. The dotted line through the symbols is a guide to the eye. Full line is an experimental data. The two energies below the In edge are marked by arrows.

pair distribution information can be obtained using resonant anomalous x-ray scattering [51, 52, 53]. Resonant x-ray scattering utilizes the energy dependence of the atomic scattering factor near the absorption edge,

$$f(Q, E) = f_0(Q) + f'(E) + if''(E),$$ (2.10)

where $f_0(Q)$ is the usual atomic scattering factor and $f'(E)$ and $f''(E)$ are the anomalous scattering terms depending on the x-ray photon energy E. Figure 2.3 shows energy dependence of the anomalous scattering terms of indium [51]. The $f'(E)$ changes rapidly within $\approx$ 100 eV around the absorption edge. By taking the difference between two data sets measured just below (few eV) the absorption edge and a few hundred eV from the edge, we obtain a differential structure function which con-

21
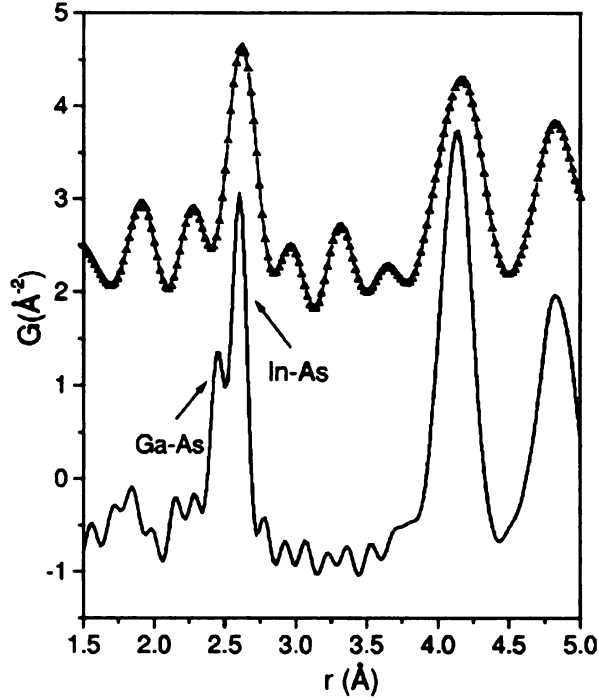
Figure 2.4: The total (full line) and In differential (symbols) atomic pair distribution functions of $In_{0.5}Ga_{0.5}As$ alloy [51]. The In-differential PDF is significantly broader than the total-PDF due to the lower Q_{max}.

tains contributions only from the target atom. The corresponding Fourier transform of the differential structure function gives pair correlations involving just the target atom. Figure 2.4 shows the total PDF and In-differential PDF of $In_{0.5}Ga_{0.5}As$. The In-differential PDF shows only atom pairs involving indium such as In-As and In-In.

2.2.1 Real space and Q-space representations of local structure

The PDF, $G(r)$, defined in Eq. 2.7, is a sine *Fourier transform* of experimentally measurable 'reduced structure function', $Q[S(Q-1]$. Therefore it contains equivalent information to the powder diffraction data. However, the PDF emphasizes the diffuse
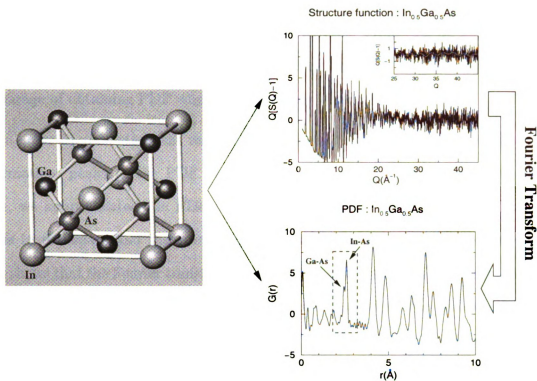
Figure 2.5: The illustration of $In_{0.5}Ga_{0.5}As$ structure and resulting structure function, and PDF. The high-Q oscillating diffuse scattering contains the local structure information. This is confirmed by the back-Fourier transform of the PDF NN peak which reproduces the oscillating diffuse scattering in momentum-space.

scattering through the Fourier transform and reflects the local structure more directly. Figure 2.5 shows the model structure of $In_xGa_{1-x}As$ at $x = 0.5$. The In and Ga atoms share one sublattice and As sits on the other sublattice in the zinc-blende structure. As Ga substitutes for In, arsenic can have two different neighbors: In and Ga. Since Ga-As and In-As bond lengths are different, the substitution of In by Ga builds up strain energy. Therefore in order to minimize the strain energy, the As atom displaces from its average position and the tetrahedron distorts locally. The local disorder introduced by alloying is evident in powder diffraction as enlarged effective Debye-Waller factor and Bragg peaks disappear at much lower Q than those of pure In-As and Ga-As. Instead, diffuse scattering shows up in the high-Q region. The

corresponding PDF of the structure function shows clearly resolved nearest neighbor peak at the position of Ga-As and In-As bond lengths. From this we know that the alloy sustains two distinct Ga-As and In-As bond lengths. This clearly shows the advantage of obtaining PDF when a material has disorder.

In order to understand the relationship between real-space and momentum-space information, peaks in the PDF are Fourier transformed to the momentum-space. Here, we approximated the PDF peak as a Gaussian. Figure 2.6 shows Gaussian peaks in real-space and the corresponding representation in the momentum-space. This shows that the Fourier transform of the Gaussian function is a damped oscillating function. The damping in momentum-space is determined by the peak width of the Gaussian function. Broad peaks in the PDF damp out faster in Q-space so high Q-space contains information about the sharp (nearest neighbor) peak. The position of nearest neighbor peak can be determined from the wavelength of the oscillation via $r_c = 2\pi/\lambda_Q$ where r_c is a peak position and λ_Q is the wavelength of oscillation in Q-space. In $In_{0.5}Ga_{0.5}As$, the NN peak has two sharp peaks corresponding to Ga-As and In-As bonds. These sharp peaks generate two oscillating waves with very small difference in wavelength in Q-space. The oscillating signal in high-Q region shows a beat from these two waves.

2.3 Data Collection and Analysis

2.3.1 X-ray scattering and synchrotron radiation

As we discussed in section 2.2, the high-Q space stores significant local structural information. In addition, if Q_{max} is larger, the real-space resolution becomes better. And $Q_{max} \geq 40$ Å^{-1} is required to resolve small bond length difference (≈ 0.17 Å) in $In_xGa_{1-x}As$ alloys. We can obtain the powder diffraction pattern using either x-ray
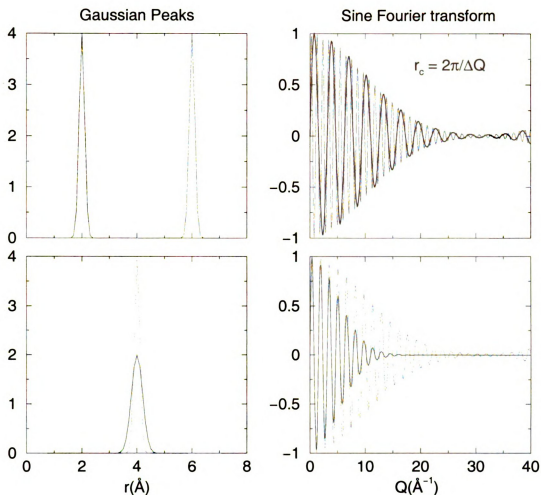
Figure 2.6: Relationship between real-space and momentum-space information. The Fourier transform of a Gaussian function is represented as a damped oscillating function. The damping in momentum-space is determined by the peak width of the Gaussian function and from the frequency of the oscillation, the Gaussian peak position is obtained via $r_c = 2\pi/\lambda_Q$ where r_c is peak center and λ_Q is a wavelength of oscillation in Q-space.

or neutron scattering. In neutron scattering, however, an indium nuclear-absorption resonance in neutron scattering limits Q_{max}. Conventional x-ray scattering also has a serious limitation in obtaining high Q_{max}. In x-ray scattering, the incident beam is scattered by the electron clouds which are spread throughout the atom. This leads to phase differences in x-rays scattered from different parts of the atom. Therefore,
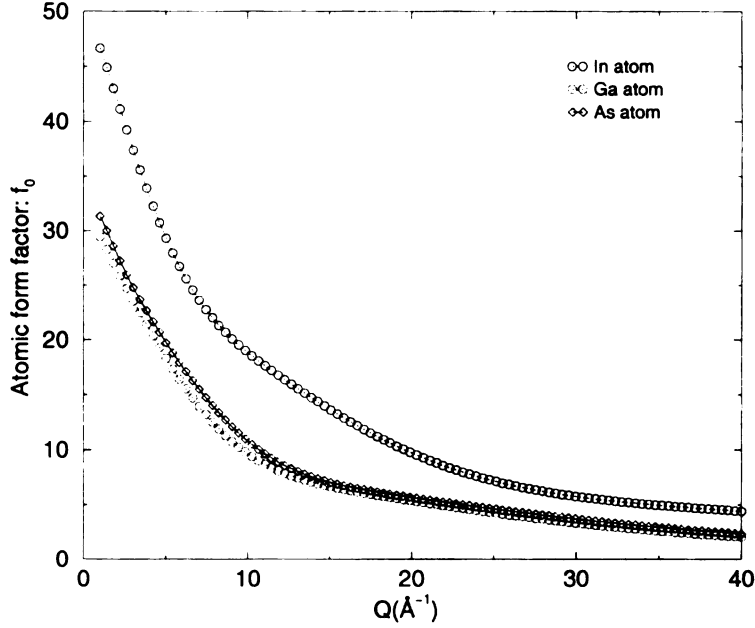
Figure 2.7: Atomic scattering factors of In, Ga, and As atoms

the scattered intensity for the atom decreases as the scattering angle increases [37].

This decrease in scattered intensity is expressed by the atomic scattering factor, f.

Figure 2.7 shows atomic scattering factors of In, Ga, and As atoms as a function

of Q calculated using the analytical formula with nine coefficients developed by D.

Waasmaier & A. Kirfel [54]. It is clear that the scattering factor decreases signif-

icantly as the wavevector, Q, increases and beyond Q=20 Å it is almost 10 times

smaller than the value at Q=0. Due to this decreasing atomic scattering factor, x-ray

scattering has not been considered as a suitable choice for obtaining high-Q space

data. In addition, there is another limitation in using conventional x-rays for obtain-

ing high-Q space data. Since the momentum transfer is given by $Q = 4\pi \sin\theta/\lambda$,

short wavelength (high energy) incident x-rays are required to get high momentum

transfers. However, the highest energy of conventional x-rays is from Ag K_α and

is around 22 keV ($\approx$ 0.56 Å) which corresponds to Q_{max} around 20 Å^{-1}. This is
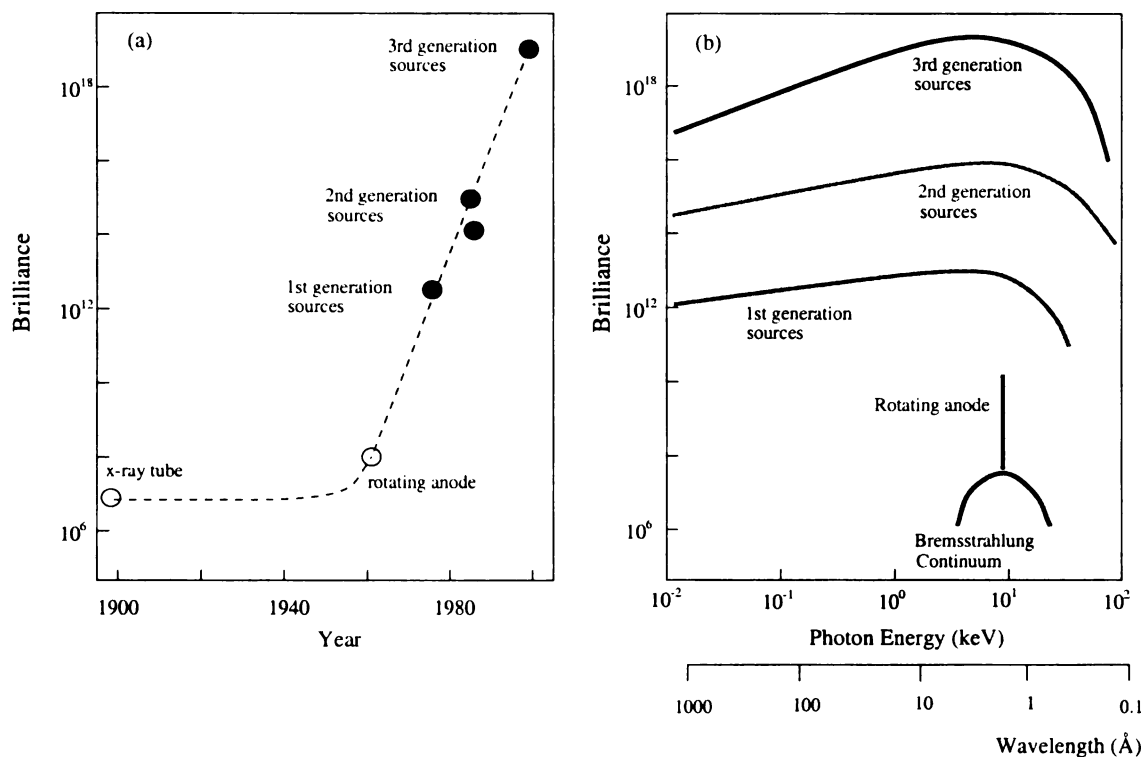
Figure 2.8: (a) Progress in the brilliance of the X-ray beams during 20th century [55], (b) Brilliance of the x-ray beams as a function of energy.

not enough to get high real-space resolution in the PDF method. These problems, atomic scattering factor and limited available radiation sources, were addressed using synchrotron radiation sources and in particular the advent of third generation synchrotron sources. Figure 2.8 (a) shows the progress in the brilliance (photons)of x-ray beams during the 20th century. In Figure 2.8 (b), the energy dependence of the brilliance (photons/sec/mm^2/mrad^2 in 0.1 % b.w.) of the x-ray is shown. With the advent of third generation synchrotron radiation, beams that are 10^{10} times more brilliant than conventional x-rays are available. In addition, the third generation synchrotron radiation covers most wavelengths, from infrared to hard x-rays, making it possible to collect data beyond $Q_{max}=40\text{Å}^{-1}$.
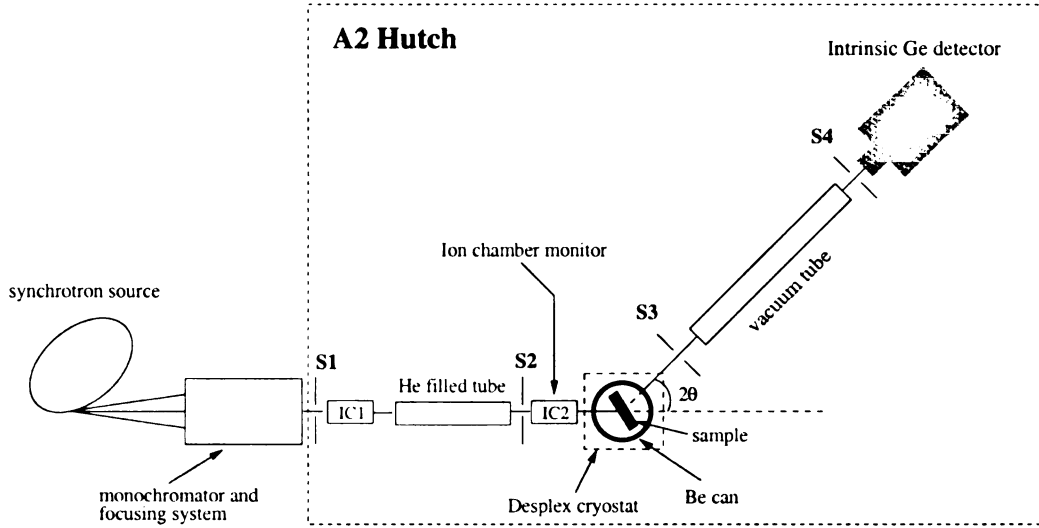
Figure 2.9: Illustration of the experimental set-up

2.3.2 Data Collection and Analysis Procedure

In this Section, we present brief description of the experimental set-up and data collection strategy. Figure 2.9 shows the experimental set-up at Cornell High Energy Synchrotron Source (CHESS). The intense white beam is generated using an insertion device (wiggler) at the A2 beamline. The white beam is dispersed using a Si(111) double-bounce monochromator. Unlike the conventional tube x-rays, in a synchrotron experiment the incident x-ray intensity is changing with time. Therefore it is important to monitor the incident x-ray intensity. This will be used to normalize for the incident intensity. Two Ion chamber (IC) monitors with flowing Ar gas were used. All measurements were carried out in flat plate symmetric transmission geometry. In order to minimize thermal atomic motion in the samples, and hence increase the sensitivity to static displacements of atoms, the samples were cooled down to 10 K using a closed cycle helium refrigerator mounted on the Huber 6 circle diffractormeter. The samples were uniform flat plates of loosely packed fine powder suspended between

thin foils of kapton tape. The sample thicknesses were adjusted to achieve sample absorption $\mu t \sim 1$ for the incident x-ray energy, where μ is the linear absorption coefficient of the sample and t is the sample thickness.

During the whole measurement, the maximum intensity was scaled so that the count rate across the whole detector energy range in the Ge detector did not exceed $\sim 2 \times 10^4 \ s^{-1}$. At these count-rates detector dead-time effects are significant but can be reliably corrected as we describe below. To reduce the random noise level below 1%, we repeated runs until the total *elastic scattering* counts become larger than 10,000 counts at each value of Q. Also, to obtain a better powder average the sample was rocked with an amplitude of $\pm 0.5°$ at each Q-position. The scattered x-rays were detected using an intrinsic Ge solid state detector. The signal from the Ge detector was processed in two ways. The signal was fed to a multi-channel analyzer (MCA) so that a complete energy spectrum was recorded at each data-point. The signals from the elastic and Compton scattered radiation could then be separated using software after the measurement. In parallel, the data were also fed through single-channel pulse-height analyzers (SCA) which were preset to collect the elastic scattering, Compton scattering, and a wider energy window to collect both the elastic and Compton signals.

For the SCAs, the proper energy channel setting for the elastic scattering is crucial. Any error in the channel setting could cause an unknown contamination by Compton scattering and make data corrections very difficult. There's no such problem in the MCA method since the entire energy spectrum of the scattered radiation is measured at each value of Q. In addition, Laaziri *et al.* [56] developed a fitting procedure for separating Compton from elastic scattering using an MCA spectrum for the whole Q-range. The main disadvantage of the MCA method is that it has a larger dead-
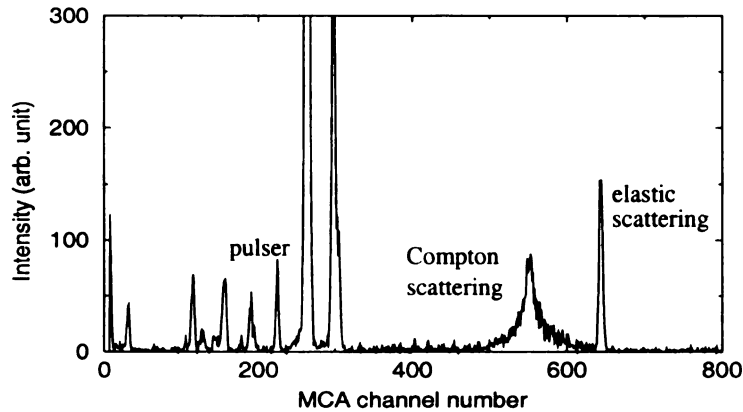
Figure 2.10: MCA spectrum of InAs at Q=45 Å^{-1}. Peaks in the spectrum from the elastic and Compton scattering are labelled, as is a peak from an electronic pulser used for dead-time correction. The other peaks in the spectrum come from various fluorescence and escape peaks.

time, although this can be reliably corrected as we show below. Figure 2.10 shows a representative MCA spectrum taken from the InAs sample at $Q = 45$ Å. It is clear that the Compton and elastic scattering are well resolved at this high momentum transfer. The elastically scattered signal, which contains the structural information, is obtained by integrating the area under the elastic scattering peak.

In a diffraction experiment, the measured x-ray diffraction data suffers from experimental effects like sample absorption, x-ray polarization and so on. Therefore we can express [34] the measured intensity in the following way:

$$I^{mea}(Q) = PA[N(I^{coh}_{eu} + I^{inc}_{eu} + I^{mul}_{eu})], \qquad (2.11)$$

where P is the polarization factor, A the absorption factor, N the normalization constant, and I^{coh}_{eu}, I^{inc}_{eu}, I^{mul}_{eu} are the coherent single scattering, incoherent (Compton), and multiple scattering intensities, respectively, per atom, in electron units. The total scattering structure function, $S(Q)$, is then defined as

$$S(Q) = [I^{coh}_{eu} - (\langle f^2 \rangle - \langle f \rangle^2)]/\langle f \rangle^2, \qquad (2.12)$$

30

where $\langle f \rangle = \langle f(Q) \rangle$ is the sample average atomic form factor and $\langle f^2 \rangle$ is the sample average of the square of the atomic form factor. Therefore, to obtain $S(Q)$ from the measured diffraction data, we have to apply corrections such as multiple scattering, polarization, absorption, Compton scattering and Laue diffuse corrections on the raw data [34, 38].

2.3.3 PDFgetX

As we discussed in Section 2.3.2, it is necessary to apply several steps of corrections to obtain the total scattering structure function, S(Q), from the raw powder diffraction pattern. In the high intensity high energy synchrotron x-ray experiments, it is important to correct for detector dead-time effect. In addition, proper corrections for the multiple scattering and Compton scattering are more important in high-Q region.

For the analysis of the high intensity high energy synchrotron x-ray powder diffraction data, we developed data analysis program, PDFgetX [57]. PDFgetX is written in Yorick language. This requires users to install Yorick, a freely available program [58]. PDFgetX applies corrections to "input" data in sequence. During the analysis, it displays all corrections to raw data and saves all parameters used in the analysis. This makes the analysis procedure easy to understand and allows reproducible results. The manual of PDFgetX is attached in Appendix A and the details about the data analysis procedure and corrections are given in Appendix A.4 and A.5 respectively. The program is available from the following website: http://www.pa.msu.edu/cmp/billinge-group/programs/PDFgetX.html.

Chapter 3

Correlated Thermal Motion in Semiconductor Compounds

3.1   Introduction

Atoms in crystals are coupled together by the interatomic forces. Therefore, a motion of one atom influences those of others. Figure 3.1 shows a schematic diagram of atomic motions in three different interatomic force systems. In a rigid-body system, the interatomic force is extremely strong and all atoms move in phase. In this case, we can expect peaks in the PDF to be delta-functions. In another extreme case such as the Einstein model every atom moves independently. This type of atomic motion results in broad PDF peaks whose widths are given by the root mean-square atomic displacement amplitude ($\sqrt{\langle u^2 \rangle}$). In real materials, the interatomic forces depend on the atom separation; it is strong for nearest neighbor interaction and decreases as the atom separation increases. In this case, near-neighbor atoms tend to move in-phase with each other and far-neighbors move independently. As a result, the near-neighbor PDF peaks are sharper than those of far-neighbor pairs. Therefore, from the PDF peak width as a function of atom separation, we can measure the degree of correlation in atomic motion. In addition, from the details of correlated atomic motion, we can obtain information about potential parameters.

Rigid-Body Motion

(a)

G(r)

r

Uncorrelated Atomic Motion

(b)

G(r)

r

Correlated Atomic Motion

(c)

α

G(r)

r
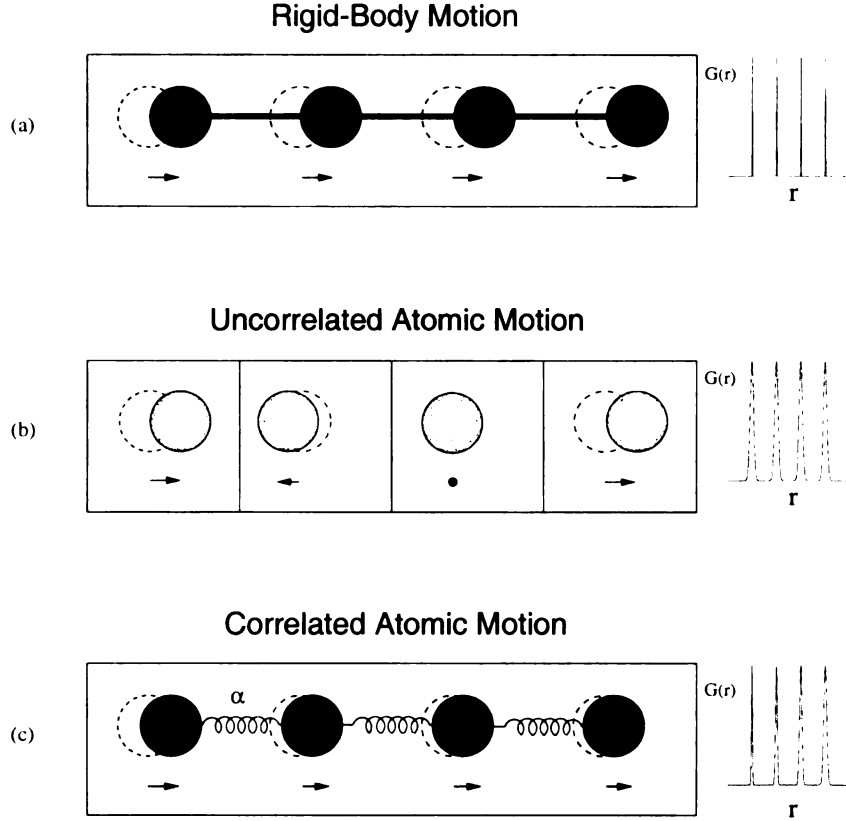
Figure 3.1: Schematic diagram showing an instantaneous snapshot of atomic positions in (a) rigid-body model (b) Einstein model (c) Debye model. In (a) and (b) all PDF peaks have the same width independent of atom separation. In (c) PDF peak width increases up to the root mean-square displacement as atom separation increases.

In a scattering experiment, the information about correlated atomic motion is contained in thermal diffuse scattering [32, 33]. Therefore the most detailed information can be obtained from phonon dispersion curves determined using inelastic neutron scattering. More recently very high energy resolution x-ray scattering has successfully been used to measure phonon dispersion curves [59, 60]. Another approach that yields this information with lower precision is the study of x-ray thermal diffuse scattering from single crystals without resolving energy [36, 61]. Other experimental techniques include Raman scattering or IR absorption which can only extract frequencies of zone center phonons but no information about phonon dispersion or

zone edge behavior [4]. The correlated motion of near neighbor atoms also can be measured in x-ray absorption fine structure (XAFS) experiments [62] which directly probe their relative motion. In these measurements, however, the information about the relative motion of far neighbor pairs is very limited and uncorrelated thermal parameters are not available.

We have taken the approach of extracting correlated thermal motion from powder diffraction data. This approach may not seem to be favorable since not only is energy information lost but also the diffuse scattering is isotropically averaged. Nevertheless, we show that this approach yields extensive information. It has the additional benefit that the experiments are straightforward and do not require single crystals. In the powder diffraction data, the Bragg peak intensity is attenuated as a function of scattering angle by the well-known Debye-Waller factor [36]. The 'remaining' intensity shows up as diffuse scattering. If the correlated motions are taken into account, the behavior of the intensities of the Bragg reflections is unchanged but as shown in Figure 3.2, so-called thermal diffuse scattering (TDS) appears centered at the Bragg peak positions. The TDS is exaggerated in this picture. By measuring the attenuation of Bragg-peak intensity it is possible to find the mean-square atomic displacement amplitude, $\langle u^2 \rangle$, which corresponds to the uncorrelated value of the thermal motion. However, in order to learn about the correlated motion of atoms, *all* diffraction data including TDS must be used [36, 63]. Although directional information is lost, it is still possible to extract significant information about the correlation of thermal motions even in systems with multiple atoms in the unit cell.

A representation of the powder diffraction data that emphasizes the correlated atomic motions is the atomic pair distribution function. The PDF peak width gives information about the correlation of the atomic motion since it is a measure of the
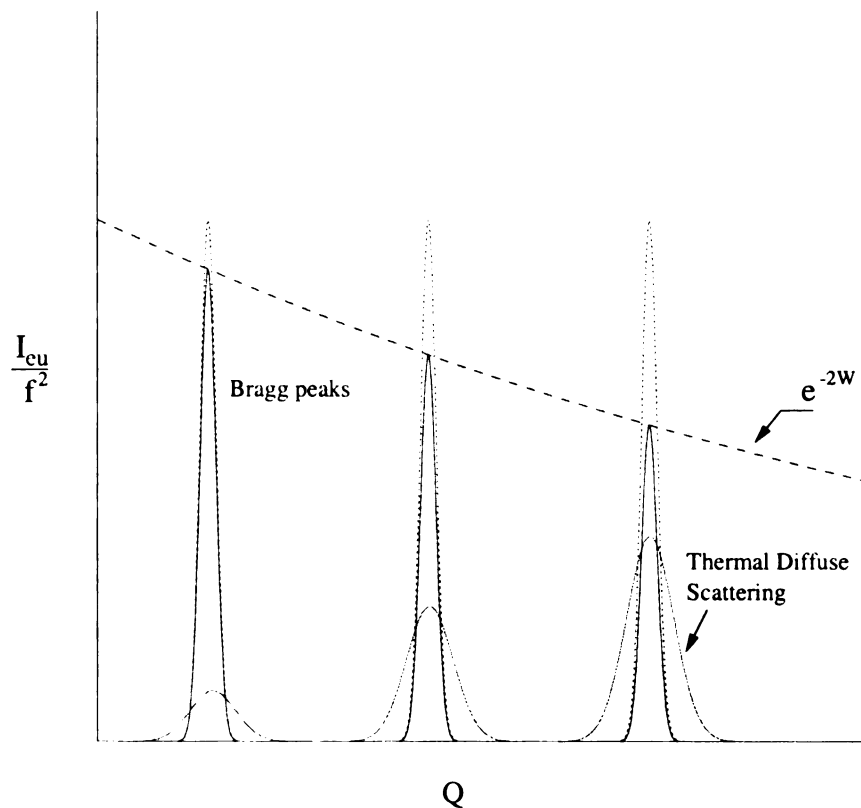
Figure 3.2: Thermal diffuse scattering. The TDS intensity is exaggerated in the picture. W is the Debye-Waller factor.

amplitude of relative motions of atom pairs. At low r_{ij} where r_{ij} is the separation distance of the pair of atoms, the PDF peaks are relatively sharpened because of the tendency for near-neighbor atoms to move in-phase with each other. This behavior was first analyzed by Kaplow in a series of papers [32, 33, 63] and interatomic potentials were determined directly from the PDF for a number of elemental metals. With the advent of modern synchrotron x-ray and neutron sources and high-speed computing, the reliability and utility of this technique has dramatically improved from these early investigations.

3.2 Mean-Square Relative Displacements in Crystals

The PDF peak shape can be approximated by a Gaussian function. The peak position measures atom pair distance and its width is determined by the standard deviation of atom distance from the average value. Therefore the peak width can be approximated by the mean-square relative displacement (MSRD) of atom pair [50], projected onto the vector joining the pair of atoms as is shown in Eq. 3.1

$$\sigma_{ij}^2 = \langle [(\mathbf{u_i} - \mathbf{u_j}) \cdot \hat{\mathbf{r}}_{\mathbf{ij}}]^2 \rangle, \tag{3.1}$$

where σ_{ij} is a peak width of atom pair i, j and $\mathbf{u_i}, \mathbf{u_j}$ are thermal displacements of atom i and j from their average positions. The vector $\hat{\mathbf{r}}_{\mathbf{ij}}$ is a unit vector parallel to the vector connecting atoms i, j, and the angular brackets indicate an ensemble average. This equation can be rearranged as

$$\sigma_{ij}^2 = \langle [\mathbf{u_i} \cdot \hat{\mathbf{r}}_{\mathbf{ij}}]^2 \rangle + \langle [\mathbf{u_j} \cdot \hat{\mathbf{r}}_{\mathbf{ij}}]^2 \rangle - 2 \langle (\mathbf{u_i} \cdot \hat{\mathbf{r}}_{\mathbf{ij}})(\mathbf{u_j} \cdot \hat{\mathbf{r}}_{\mathbf{ij}}) \rangle. \tag{3.2}$$

Equation 3.2 shows that the MSRD (σ_{ij}^2) is composed of the mean-square displacement (MSD) of each atom $\langle [\mathbf{u_i} \cdot \hat{\mathbf{r}}_{\mathbf{ij}}]^2 \rangle$, $\langle [\mathbf{u_j} \cdot \hat{\mathbf{r}}_{\mathbf{ij}}]^2 \rangle$ and the displacement correlation function (DCF), $\langle (\mathbf{u_i} \cdot \hat{\mathbf{r}}_{\mathbf{ij}})(\mathbf{u_j} \cdot \hat{\mathbf{r}}_{\mathbf{ij}}) \rangle$. For a monoatomic crystal, the MSRD can be represented as the following

$$\sigma_{ij}^2 = \frac{2\hbar}{NM} \sum_{k,s} \frac{1}{\omega_s(k)} (\hat{\mathbf{e}}_{\mathbf{k,s}} \cdot \hat{\mathbf{r}}_{\mathbf{ij}})^2 [n(\omega_s(k)) + 1/2][1 - \cos(\mathbf{k} \cdot \mathbf{r_{ij}})], \tag{3.3}$$

where $\omega_s(k)$ is a phonon frequency with wave vector k in branch s, $n(\omega_s(k))$ is the phonon occupation number, $\hat{\mathbf{e}}_{\mathbf{k,s}}$ is the polarization vector of the k, s phonon mode. N is the number of atoms and M is the mass of the atom. If we know the potential parameters for a system under study, we can obtain phonon frequency ($\omega_s(k)$) and polarization ($\hat{\mathbf{e}}_{\mathbf{k,s}}$) from the eigenvalues and eigenvectors of the dynamical matrix,
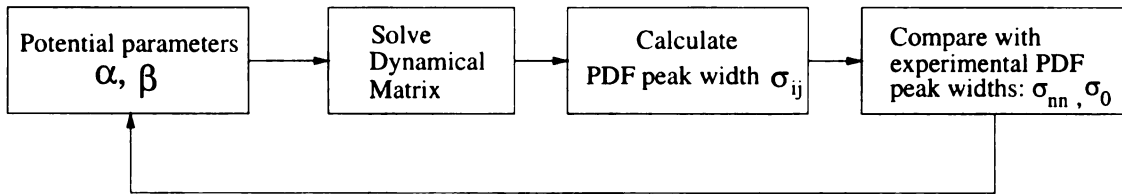
Figure 3.3: Schematic diagram of determining potential parameters using Kirkwood potential and experimental PDF peak widths in InAs compound.

respectively [50]. Then, using Eq. 3.3 we can calculate the MSRD for all atom pairs and by varying the potential parameters until the theoretical MSRD matches the experimental values, we can estimate the potential parameters. Figure 3.3 shows a schematic diagram of the procedure for determining the potential parameters using a Kirkwood potential in semiconductor compounds with bond stretching (α) and bond bending (β) force constants.

3.3   Experiments

All measurements were made using x-ray radiation, at the National Synchrotron Light Source (NSLS) and at Cornell High Energy Synchrotron Source (CHESS). Ni and InAs were measured at room temperature at X7A at NSLS using 30 KeV x-rays. GaAs was measured at the beam line A2 at CHESS using 60 KeV ($\lambda = 0.206$ Å) x-rays. The data were corrected for absorption, multiple scattering and polarization effects. Background and Compton scattering were removed and the data were normalized for flux and number of scatterer to obtain the total scattering structure function, S(Q), as is described in Section 2.3. The experimental PDF, $G(r)$, is obtained by taking the Fourier transform of the reduced structure function, $F(Q)$, according to Eq. 2.7.
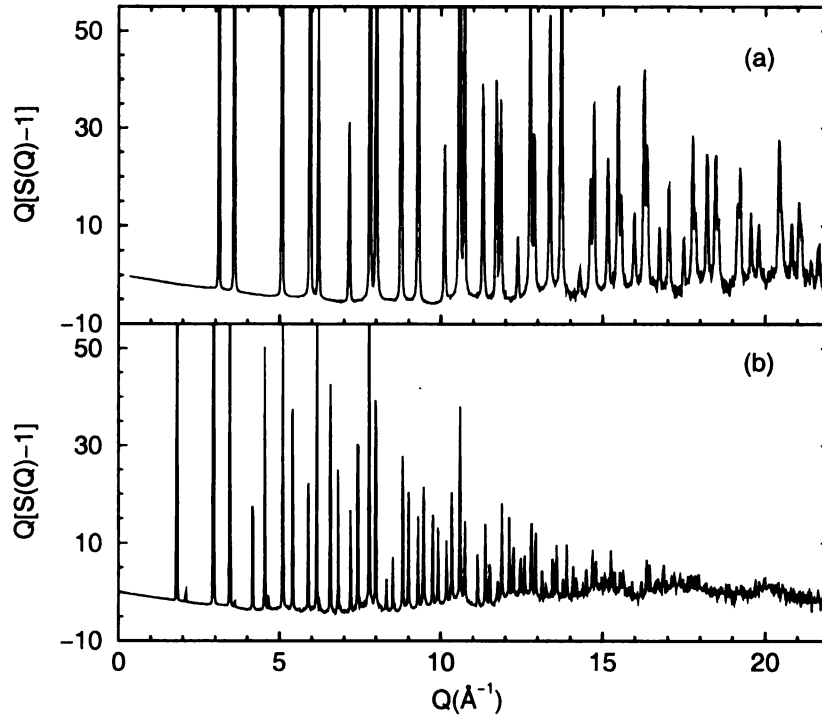
Figure 3.4: Reduced structure functions, F(Q) = Q[S(Q)-1] of (a) Ni, and (b) InAs measured at T=300 K.

3.4 Correlated Thermal Motion in Ni and InAs

In order to study how the atomic correlation depends on the interatomic force, we first studied correlated atomic motions in Ni and InAs which have very different types of bonding forces. In Ni, the bonding between atom is isotropic metallic bonding. On the contrary, InAs has covalent bonding which is very directional. Therefore, we expect these systems will serve as good examples for the study of the dependence of atomic correlations on the interatomic forces. Figure 3.4(a) and (b), shows the reduced structure function, F(Q) = Q[S(Q)-1], of the Ni and InAs data measured at T=300 K. The TDS is evident under the Bragg peaks in the high Q-region. The Q-range probed is limited by the x-ray energy and flux in these experiments at NSLS.

The corresponding PDFs are shown in Figure 3.5 as open circles.

3.4.1 Modeling and extraction of the PDF peak width

In principle one can imagine various ways to extract the widths of the individual peaks from the experimental PDF. However, the task is not as straightforward as it might seem. One of the problems is the contribution of termination ripples. These ripples appear in the PDF from the Fourier transform due to a finite data range. They are well understood [40], but may cause large errors in conventional fitting or integration procedures. Here we have used 'real-space' Rietveld program PDFFIT [64], which takes those experimental effects into account, to fit a model PDF, $G_m(r)$, to the observed PDF. The model PDF, $G_m(r)$, is defined as [5]

$$G_m(r) + 4\pi r \rho_0 = \frac{1}{r} \sum_i \sum_j \frac{f_i f_j}{\langle f \rangle^2} \delta(r - r_{ij}). \tag{3.4}$$

The sums are over all atoms within the sample. The number density of the sample is given by ρ_0. The value f_i is the atomic scattering factor of atom i evaluated at $Q = 0$, in other words the number of electrons Z for atom i. The sample average atomic scattering factor at $Q = 0$ is $\langle f \rangle$. Additionally, each atomic pair correlation, $\delta(r - r_{ij})$, is convoluted with a Gaussian to account for thermal motion. Finally, the Gaussian peaks are convoluted with a Sinc function to account for the experimental termination effect.

In order to see the correlation effect in the PDF, we first refined the InAs PDF with the assumption that all PDF peaks have the uncorrelated width (refinement A) given by the same as the root mean-square displacements of the atoms in the pair. The result is shown in Figure 3.6. It is immediately obvious that although the agreement at large values of r is good, the first peak of the model PDF, $G_m(r)$ is too broad compared to the experimental PDF. This directly shows the effect of correlated
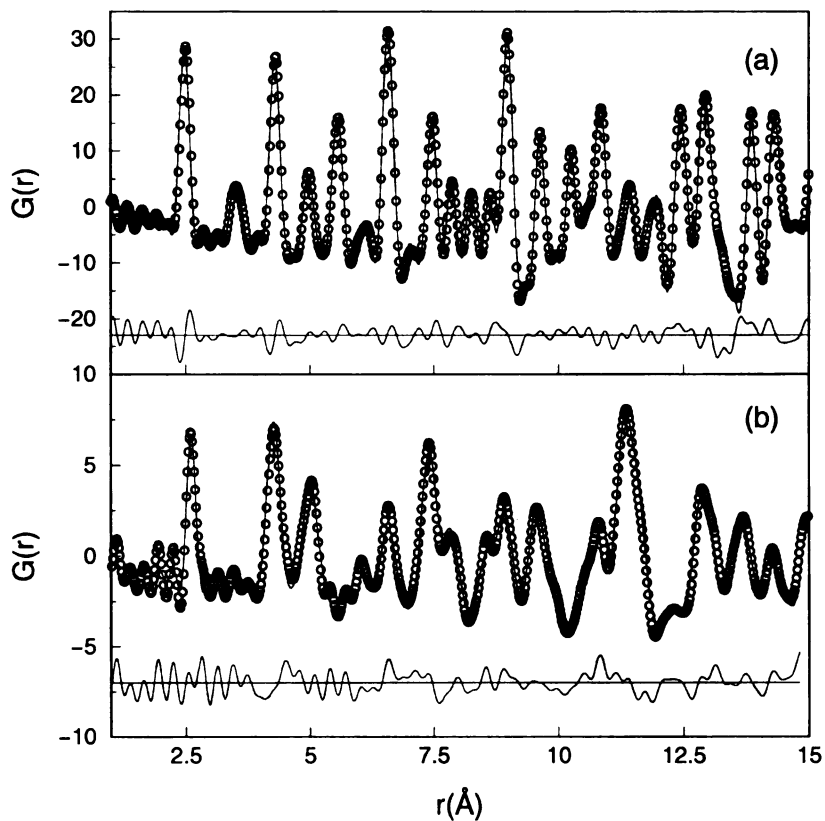
Figure 3.5: Experimental PDF (circles) and model PDF (solid line) of (a) Ni, and (b) InAs; correlation in thermal atomic motion is taken into account (refinement B). Difference curves are plotted below the data.

motion for the nearest neighbor due to the strong covalent bond between In and As. In refinement A, the sharpening of the PDF peaks at low values of r was not taken into account to illustrate this point. Thus, the calculated PDF we see in Figure 3.6 corresponds to the case of completely *uncorrelated* motion.

The effect of *correlated* atomic motion is taken into account empirically in our modeling by describing the r dependence of the PDF peak width, σ_c by the following equation,

$$\sigma_c = \sigma_0 - \frac{\delta}{r_{ij}^2}. \tag{3.5}$$
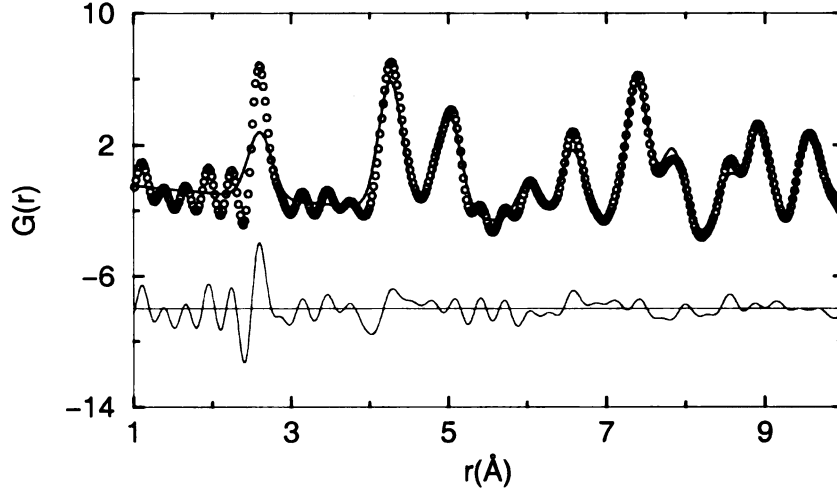
Figure 3.6: Experimental PDF (circles) and model PDF (solid line) of InAs; No correlation in thermal atomic motion is assumed (refinement A). All PDF peaks have the same width as given by the root mean-square displacement. Also shown is a difference curve between data and fit.

The parameter σ_0 corresponds to the uncorrelated thermal motion of atom pairs and is given by $\sigma_0^2 = \sigma_i^2 + \sigma_j^2$, where σ_i and σ_j are the amplitudes of uncorrelated thermal motion ($\sqrt{\langle u^2 \rangle}$) of atoms i and j and δ is an empirical parameter describing the sharpening of the PDF peaks. The parameters σ_0 and δ are refined in the modeling process. Figure 3.5 shows the refinement results including the correlated atomic motion (refinement B) for the Ni and InAs data. We observe a good agreement between experimental and calculated PDF over the complete r range.

To explicitly extract the peak width, $\sigma_c(r)$, as a function of r, we carried out the refinement in two steps. In the first step, all parameters are refined using the complete r range of the experimental PDF. In a second step multiple refinements were carried out, using only a small region in r around each PDF peak. In this step all parameters except lattice parameters and the thermal motion parameters were kept fixed. This approach allowed us to extract individual peak widths reliably.

41

3.4.2 Results

In order to describe the motional correlations more quantitatively, a correlation parameter ϕ can be defined using the following equation [62],

$$\sigma_c^2 = \sigma_i^2 + \sigma_j^2 - 2\sigma_i\sigma_j\phi. \tag{3.6}$$

It can be seen from Eq. 3.6 that $\phi = 0$ corresponds to completely uncorrelated motion. Positive values of ϕ describe a situation where the atoms move in phase, thus the resulting value of σ_c is smaller than for the uncorrelated case. Negative values of ϕ stand for neighboring atoms moving in opposite directions. Using Eq. 3.6 the correlation parameter ϕ can be calculated from the PDF results as

$$\phi = \frac{\sigma_0^2 - \sigma_c^2}{2\sigma_i\sigma_j}. \tag{3.7}$$

The peak widths and correlation parameters, ϕ, as a function of the separation distance r are shown in Figure 3.7 for the Ni and InAs crystals.

A. Ni

The r-dependence of the PDF peak width and the correlation ϕ for Ni is shown in Figure 3.7(a). Even in this close packed compound with isotropic metallic bonding we observe a weak correlation of the motion of neighboring atoms, e.g. the correlation parameter for the nearest neighbor is $\phi = 0.32$ corresponding to a value of $\sigma_c = 0.0823(2)$ Å. Fitting the expression given in Eq. 3.5 to the data points in Figure 3.7, we find the following values: $\sigma_0 = 0.10(3)$ Å and $\delta = 0.11(4)$ Å^3. Here the width of the PDF peak is only determined by thermal broadening and zero-point motion and no static disorder or strain is present in the crystal.

The value for the uncorrelated thermal motion of $\sigma_0 = 0.10(3)$ Å determined in this analysis can directly be compared to the theoretical value for nickel of $\sigma_{Ni} = 0.1045$ Å
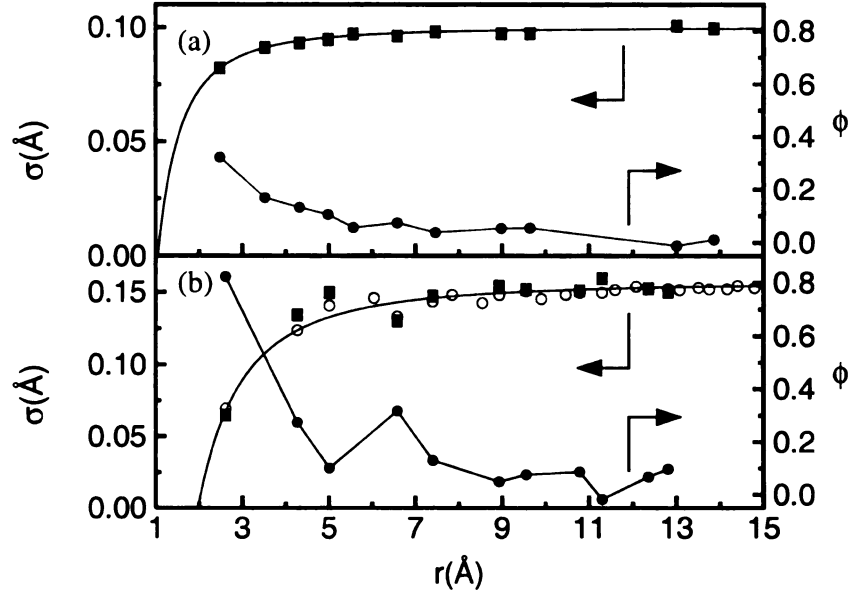
Figure 3.7: (a) Ni: PDF peak width σ_{ij} (closed square) and correlation parameter, ϕ (closed circle) as a function of r. The solid line marks the empirical relation in Eq. 3.5. (b) InAs: Open circles are theoretical values by Chung and Thorpe [50]. The other symbols are the same as in (a).

calculated from the Debye temperature of Ni [65]. The good agreement of the observed and theoretical value indicates that the PDF analysis allows one to extract thermal parameters on an absolute scale.

B. InAs

InAs crystallizes in the zincblende structure and shows strong covalent bonding. The r dependence of the PDF peak width and the correlation parameter ϕ are displayed in Figure 3.7(b). It should be noted that for some separation distances r only a theoretical value is present since no meaningful peak width could be extracted from the experimental PDF at those points due to PDF peak overlap and weakness of signal. The correlation parameter for the nearest neighbor (In-As) of $\phi = 0.82$ is much larger than in Ni reflecting the differences in the bonding of the nearest neighbors.
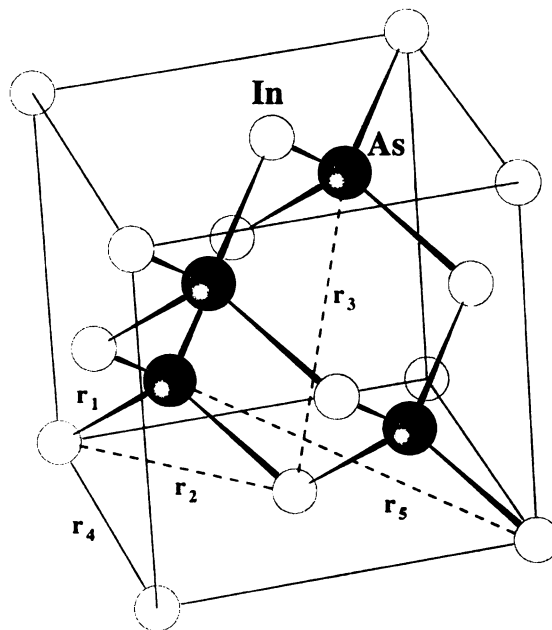
Figure 3.8: Schematic drawing of a unit cell of InAs. The marked distances, r_1 to r_5 are discussed in the text.

The corresponding value of σ_c is 0.064(2) Å. The resulting values from the empirical relation given in Eq. 3.5 are: $\sigma_0 = 0.160(7)$ Å and $\delta = 0.61(9)$ Å^3. The overall agreement between experiment and theory are good. In addition, the empirical Eq. 3.5 shows good agreement with experiment.

In contrast to the Ni results, we can observe a deviation from the empirical behavior given in Eq. 3.5 for low values of r_{ij}. These deviation appears in the theory (open circle) *and* are accurately determined in the measurement. They are not artifacts but have a real origin. An explanation of this behavior can be given as follows; First we assume all bonds to be rigid, thus the first neighboring atoms separated by $r_1 \approx 2.6$ Å would move completely in phase, i.e. $\sigma_c = 0$. This is obviously an approximation since we only observe $\sigma_c = 0.064(2)$ Å for the first neighbor. In our simple model all broadening of subsequent PDF peaks would be caused by bond bending. The

structure of InAs is illustrated in Figure 3.8. The first to fifth nearest neighbors are marked by r_1 to r_5, respectively. From Figure 3.7 we can see that the PDF peak width for neighbors separated by r_3 is larger whereas for r_5 the width is smaller than given by Eq. 3.5. To understand this behavior we need to consider the bond bending motion at the two intermediate atoms in both cases. Figure 3.9 shows the geometrical configuration of atoms involving r_3 and r_5 bonds. For atoms, i, j separated by r_3, both bending motions result in almost parallel displacements along the vector r_3 and involve *two* bending motions resulting in a weaker correlation or broader PDF peak. For neighbors separated by r_5, however, the bending motions lead to displacements roughly perpendicular to the vector r_5. In addition, the thermal motions of atom i, j involve bond stretching motion of l, k atoms which is very difficult. Due to this constraint, the combined motion can be considered as a *single* bond bending. Subsequently the correlation should be of the same magnitude as for neighbors separated by r_2 connected by just a single bond bending motion. This is in good agreement with the observed correlation parameters of 0.27 and 0.31 for neighbors separated by r_2 and r_5, respectively, but only 0.10 for neighbors separated by r_3. For large separation distances r_{ij}, the PDF peak width converges to its uncorrelated limit σ_0 and the correlation ϕ goes to zero.

Chung and Thorpe [50, 66] have calculated the r dependence of the PDF peak width theoretically using the Kirkwood model [67]. They adjusted the force constants of their model to match the PDF peak width of the first and last peak of the experimental data presented in this paper [66] and obtained the bond stretching ($\alpha = 80$ N/m) and bond bending ($\beta = 10.3$ N/m) force constants. These values show 10%~30% difference from the literature values [12] determined using the elastic constants, C_{11}, C_{12}, C_{14}. However, as we discussed in Section 1.2.5, the force constants determined from the elastic constants also contain errors around 10%~30%.
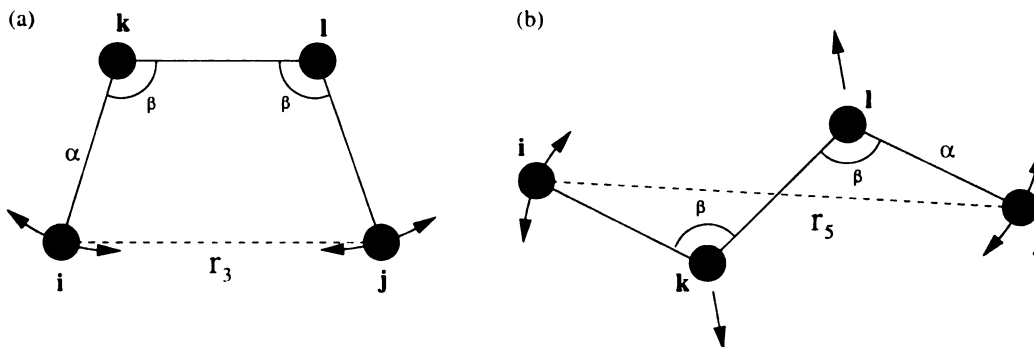
Figure 3.9: Geometrical configurations of atoms involving (a) r_3 bond and (b) r_5 bond.

Therefore it is not easy to estimate the accuracy of the force constants obtained from the PDF. In addition, we used only two data points, nearest and far-neighbor peak widths, to refine two force constants in our refinement. Therefore this could lead relatively large errors in the refined force constants. For current purpose, these force constants are reasonable. The theoretical PDF peak widths are shown as open circles in Figure 3.7(b). For more details about these calculations see references [50, 66]. The experimental and theoretical values show a good agreement. Even the deviations of the experimental data from the behavior described by Eq. 3.5 are reproduced by these theoretical calculations.

3.5 Correlated Thermal Motion: Debye approximation

We have discussed correlated atomic motion in InAs and showed that the MSRD obtained from lattice dynamical calculations using the Kirkwood potential are in good agreement with the experimental PDF peak widths. In the lattice dynamical calculations, however, the force constants must be known in advance. When the force constants are not available, the Debye approximation may be used to obtain the
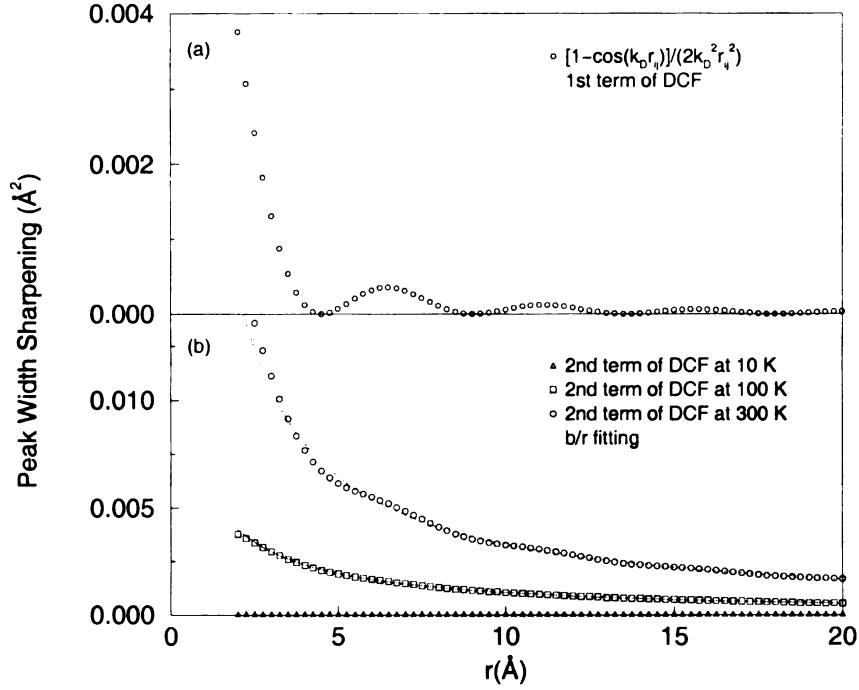
Figure 3.10: Peak width sharpening effects. (a) Open circle shows the 1st term of DCF of Eq. 3.10. (b) Symbols are the 2nd term of DCF of Eq. 3.10 at 10 K, 100 K, and 300 K. Dotted line is a fitting with b/r. b is a parameter.

PDF peak width changes as a function of atom distance. In Eq. 3.3, if we make no distinction between longitudinal and transverse phonons and take spherical averaging, then it will reduce to the following:

$$\sigma_{ij}^2 = \left\langle \frac{2\hbar}{M\omega} \left[n(\omega) + \frac{1}{2} \right] \left[1 - \cos(\mathbf{k} \cdot \mathbf{r_{ij}}) \right] \right\rangle, \tag{3.8}$$

where $\langle \cdots \rangle$ is the average over the $3N$ modes and N is the number of atoms. This result is a general expression for all materials and independent of the number of atoms per unit cell [68]. Using the Debye approximation, $\omega = ck$, Eq. 3.8 becomes

$$\sigma_{ij}^2 = \frac{2\hbar}{3NM} \int_0^{\omega_D} d\omega \, \frac{\rho(\omega)}{\omega} \left[n(\omega) + \frac{1}{2} \right] \left[1 - \frac{\sin(\omega r_{ij}/c)}{\omega r_{ij}/c} \right], \tag{3.9}$$

where $\rho(\omega) = 3N(3\omega^2/\omega_D^3)$ is the phonon density of states, c, the sound velocity and $\omega_D = ck_D$ is the Debye cut-off frequency. The Debye wave vector is given by

$k_D = (6\pi^2 N/V)^{1/3}$. Here N/V, the number density of a crystal. After integration over ω, we can rearrange Eq. 3.9 as the following:

$$\sigma_{ij}^2 = \frac{6\hbar}{Mk_Dc}\left[\frac{1}{4} + \left(\frac{T}{\Theta_D}\right)^2\Phi_1\right] - \frac{6\hbar}{M\omega_D}\left[\frac{1-\cos(k_D r_{ij})}{2(k_D r_{ij})^2}\right.$$
$$\left. + \left(\frac{T}{\Theta_D}\right)^2\int_0^{\Theta_D/T}\frac{\sin(k_D r_{ij}Tx/\Theta_D)/(k_D r_{ij}T/\Theta_D)}{e^x - 1}\,dx\right], \qquad (3.10)$$

where $\Phi_1 = \int_0^{\Theta_D/T} x(e^x - 1)^{-1}\,dx$, and x is a dimensionless variable and Θ_D is the Debye temperature. This result is known as the "Correlated Debye model" [69, 70]. In Eq. 3.10, the first term corresponds to the usual uncorrelated mean-square displacements (MSD) and the second term to the displacement correlation function (DCF). The MSD shows no r_{ij} dependence but the DCF depends explicitly on atom distance, r_{ij}. Figure 3.10 shows the r_{ij} dependence of the first and second terms of the DCF. The first term of the DCF decreases as $1/r_{ij}^2$ with a cosine modulation and the second term shows a $1/r_{ij}$ dependence. In addition, the second term of the DCF shows a strong temperature dependence. At low temperature, it is negligible compared to the first term of the DCF. However, as the temperature increases, the second term becomes dominant. This suggests that the MSRD shows a $1/r_{ij}^2$ dependence at low temperature and a $1/r_{ij}$ dependence at room temperature or higher. This r_{ij} dependence of the PDF peak width in Correlated Debye model is a little bit different from the empirical equation ($\sigma_c = \sigma_0 - \delta/r_{ij}^2$) that we used in Section 3.4. Actually our approximate expression should be okay:

$$\sigma_c^2 = \sigma_0^2 - 2\delta\sigma_0/r_{ij}^2 + \delta/r_{ij}^4$$
$$\sim \sigma_0^2 - 2\delta\sigma_0/r_{ij}^2$$
$$= \sigma_0^2 - \delta'/r_{ij}^2, \qquad (\sigma_0 \sim \delta \ll r_{ij}). \qquad (3.11)$$

What the Correlated Debye model shows is that for higher temperature (on a scale set by the θ_D) we might also need a $1/r_{ij}$ term. This shows that the empirical equation is
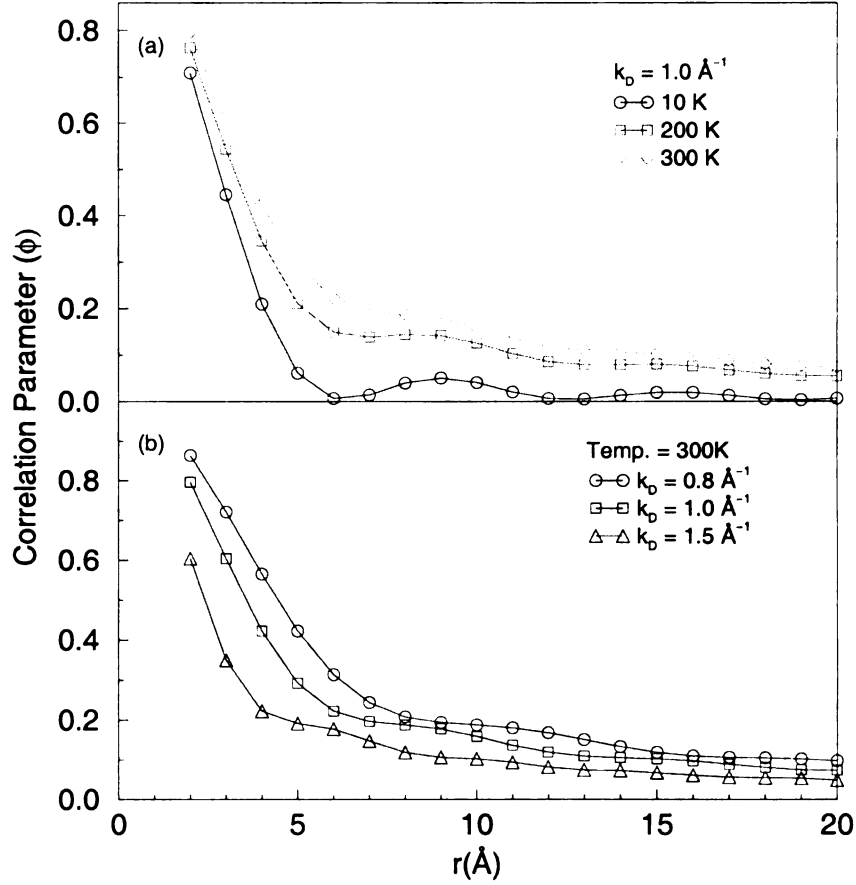
Figure 3.11: Correlation parameters calculated using the Eq 3.10. (a) Temperature and atom distance dependence of correlation parameter. Open circle (10 K), open square (200 K), and open diamond (300 K). Debye wavevector, $k_D = 1.0$ Å^{-1}, Debye temperature, $\theta_D = 400$ K. (b) Correlation parameter as a function of atom distance and Debye wavevector. Circle ($k_D = 0.8$ Å^{-1}), square ($k_D = 1.0$ Å^{-1}), and diamond ($k_D = 1.5$ Å^{-1}). Debye temperature, $\theta_D = 400$ K, temperature T = 300 K.

a good approximation in representing the r_{ij} dependence of PDF peak width although it appears it could be improved at higher temperatures by including a b/r_{ij} term.

The displacement correlation function also depends on the Debye wavevector, k_D. Figure 3.11(a) shows the correlation parameter as a function of atom distance and temperature. It shows that the correlation parameter increases as the temperature increases. This is due to the second term of DCF which increases as the temperature
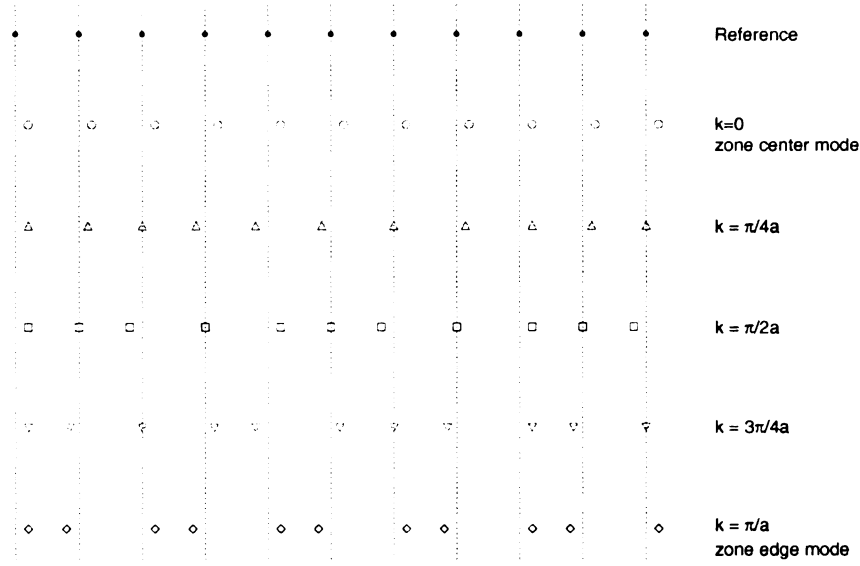
Figure 3.12: Schematic diagram of phonon modes for different values of wavevector.

increases thus results in higher correlation parameter. Figure 3.11(b) shows the k_D dependence of the correlation parameter. It clearly shows that for larger k_D, the correlation becomes smaller. Therefore, in general body-centered cubic (bcc) crystals have stronger atomic correlation than those of face-centered cubic (fcc) crystals [69] because the Debye wavevector is larger in the fcc crystals than in the bcc crystals. Considering phonon modes for different wavevectors may help to understand this result. Figure 3.12 shows a schematic diagram of longitudinal phonon modes for different wavevectors, k. For the zone center phonon mode, all atomic displacements are completely correlated. This mode doesn't contribute to the PDF peak width broadening. However, as the phonon wavevector increases, the relative displacement of neighboring atoms becomes less and less correlated and beyond $k = \pi/2a$ their motion becomes more and more anti-correlated until it is completely anti-correlated at the zone boundary. Thus with increasing Debye wavevector, the NN PDF peak gets broader.
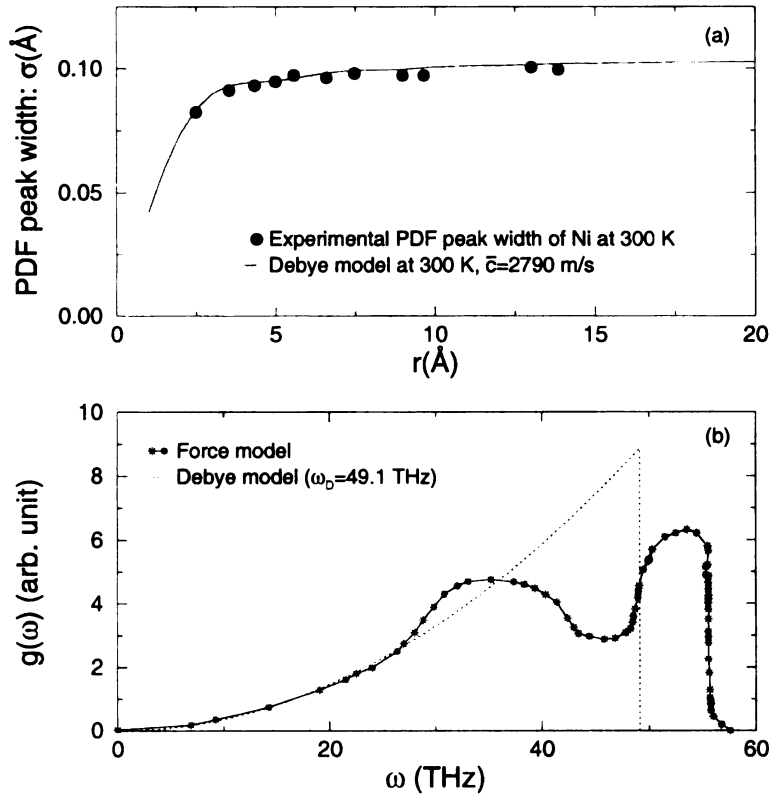
Figure 3.13: (a) Correlated Debye model calculation of Ni PDF peak width at 300 K. Circles are experimental PDF peak width and solid line is the calculation. (b) Solid line: schematic diagram of Ni phonon density of states calculated using force model [71]. Dotted line: Debye density of states with the same area as the force model calculation.

Finally, we compared experimental PDF peak widths with the σ_{ij} obtained from the Correlated Debye model. Figure 3.13(b) shows schematic diagram of Ni phonon density of states calculated using a force model [71] and corresponding Debye density of states. In this simple element, the Debye model reasonably approximate the 'real' density of states. Figure 3.13(a) shows comparison between experimental PDF peak widths and Correlated Debye model calculation at 300 K. In this calculation, Debye wavevector, k_D=1.757 Å^{-1} and sound velocity, $\bar{c}$=2790 m/s are used. With these values given by the atomic geometry and independent measurement, the Correlated

51
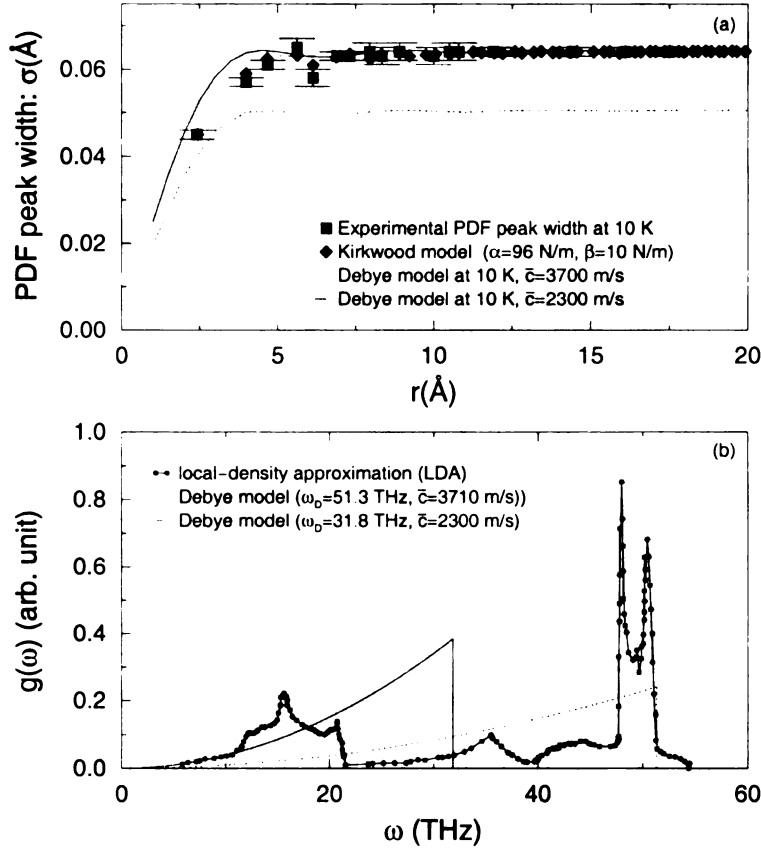
Figure 3.14: (a) PDF peak width of GaAs as a function of atom separation. Symbols: Experimental PDF peak width (closed square). PDF peak width, σ obtained from lattice dynamics calculation (closed diamond). Correlated Debye model peak width calculation using the average sound velocity, $\bar{c}$=3710 m/s (dotted line), and $\bar{c}$=2300 m/s (solid line). (b) Symbol is the GaAs phonon density of states calculated using local-density approximation [72] and solid (ω=31.8 THz) and dotted (ω=51.3 THz) lines are the corresponding Debye approximation with the same area as the LDA calculation.

Debye model shows very good agreement with the experiment without any adjustable parameters. We also compared the Correlated Debye model calculation of PDF peak width with the experimental peak widths and lattice dynamic calculation using the Kirkwood potential. Figure 3.14(a) shows the r_{ij} dependence of the PDF peak widths of GaAs at 10 K. In the Kirkwood model, the potential parameters are obtained using the procedure described in Section 3.2. In the Correlated Debye model, the Debye

wavevector, k_D=1.382 Å^{-1} is obtained from the atomic geometry and the sound velocities, c along the [100], [110], and [111] directions are calculated from the elastic constants. In Figure 3.14(a), the dashed line is obtained using the average sound velocity, $\bar{c}$=3710 m/s averaged over three different directions, [100], [110], and [111]. However, the far-neighbor peak widths calculated using this average sound velocity are off by a factor of 1.2 from the experimental PDF peak widths. This is due to the poor approximation of density of states by the Debye model as shown in Figure 3.14(b). In order to match the calculated far-neighbor peak widths to the experimental value, we used the sound velocity as a parameter. The solid line in Figure 3.14(a) is obtained using $\bar{c}$=2300 m/s. This result shows that with just one parameter, the Correlated Debye model is reasonable in predicting the experimental PDF peak widths even in more complex systems like GaAs. In addition, the comparison between the Correlated Debye model and the Kirkwood model calculation shows interesting result. The difference between these two model calculations are not significant. The general behavior of PDF peak width changes as a function of atom distance is given by the Correlated Debye model except *small* details in PDF peak width changes below $\sim$ 10 Å. This results suggest that in order to obtain reasonable interatomic potential parameters, accurate measurements of all the details of the PDF peak width changes are important.

Chapter 4

Local Structure of $In_xGa_{1-x}As$ Semiconductor Alloys

4.1 Introduction

The local structure of $In_xGa_{1-x}As$ was first studied by Mikkelson and Boyce using extended x-ray absorption fine structure (XAFS) [25]. In this experiment, Mikkelson and Boyce showed that the individual nearest neighbor (NN) Ga-As and In-As distances in the alloys are quite different from the concentration weighted average value of Ga-As and In-As distances but rather closer to the pure Ga-As and In-As distances. Further XAFS experiments showed that this is a quite general behavior for many zinc-blende type alloy systems [27, 28, 29]. Since then a number of theoretical and model studies have been carried out on the semiconductor alloys to understand how the alloys accommodate the local displacements [26, 73, 74, 75, 76, 77, 78, 79].

Until now, however, these models and theoretical predictions are tested mainly by the comparison with XAFS data. The XAFS results give information about the nearest neighbor and next nearest neighbor distances in the alloys but imprecise information about bond-length distributions and no information about higher-neighbor shells. This limited structural data makes it difficult to differentiate between competing models for the local structure. For example, even a simple radial force model [74]

54

rather accurately predicts the nearest neighbor distances of $In_xGa_{1-x}As$ alloys in the dilute limit. Therefore, one needs more complete structural information including nearest neighbor, far-neighbor distances, and bond length *distributions* to study the local structure of these alloys more accurately.

In Section 4.2, we present high real-space resolution PDFs of $In_xGa_{1-x}As$ alloys. In-As and Ga-As bond lengths and distributions are obtained from the $In_xGa_{1-x}As$ PDFs. In Section 4.3, we describe how the alloys accommodate the local distortion due to alloying using simple cluster model and more sophisticated Kirkwood potential based model. Finally, in Section 4.4, we describe correlated static displacements in $In_xGa_{1-x}As$ alloys.

4.2 High Real-Space Resolution PDF measurement of $In_xGa_{1-x}As$ Alloys

4.2.1 Sample preparation

The $In_xGa_{1-x}As$ alloy samples with compositions (x = 0, 0.17, 0.33, 0.5, 0.83, 1) were prepared by a melt and quench method. An appropriate fraction of InAs and GaAs crystals were powdered, mixed and sealed under vacuum in quartz ampoules. The samples were heated beyond the liquidus curve of the respective alloy [24, 80] to melt them and held in the molten state for 3 hours before quenching them in cold water. The alloys were powdered, resealed in vacuum, and annealed just below the solidus temperature for 72-96 hours to increase the homogeneity of the samples. After annealing, the sample was cooled down in the furnace by turning off the power. Depending on the cooling rate, the concentration fluctuation might lead to chemical clustering [81, 82, 83]. However, because of the slow cooling and the suppression of mesoscopic chemical concentration fluctuation in the $In_xGa_{1-x}As$ alloys [84] we

expect the clustering effects can be neglected in our experiment. The annealing cycle was repeated until the homogeneity of the samples, as tested by x-ray diffraction, was satisfactory. After finishing annealing, the sample was ground by hand and sieved using a 400-mesh sieve. From this, we expect that the particle size distribution is between a few μm to 38 μm and the particle size induced strain is negligible. X-ray diffraction patterns from all the samples showed single, sharp diffraction peaks at the positions expected for the nominal alloy similar to the results obtained by Mikkelson and Boyce [25].

4.2.2 PDFs of $In_xGa_{1-x}As$ alloys

Figure 4.1 shows the experimental reduced total scattering structure functions, $F(Q) = Q[S(Q) - 1]$, for the $In_xGa_{1-x}As$ alloys measured at 10 K. It is clear that the Bragg peaks are persistent up to $Q \sim 35$ Å^{-1} in the end-members, GaAs and InAs. This reflects both the long range order of the crystalline samples and the small amount of positional disorder (dynamic or static) on the atomic scale. In the alloy samples, however, the Bragg peaks disappear at much lower Q-values but still many sharp Bragg peaks are present in the mid-low Q region. Instead, oscillating diffuse scattering which contains local structural information is evident in high Q region. The observation of Bragg peaks reflects the presence of long-range crystalline order in these alloys. The fact that the Bragg peak intensity disappears at lower Q-values in the alloys than the end-members reflects that there is significant atomic scale disorder in the alloys as expected. The oscillating diffuse scattering in the high-Q region originates from the stiff nearest-neighbor In-As and Ga-As covalent bonds.

Figure 4.2 shows the corresponding reduced PDFs, $G(r)$, obtained using Eq. 2.7. In the alloys, it is clear that the first peak is split into a doublet corresponding to shorter Ga-As and longer In-As bonds [51]. The position in r of the left and
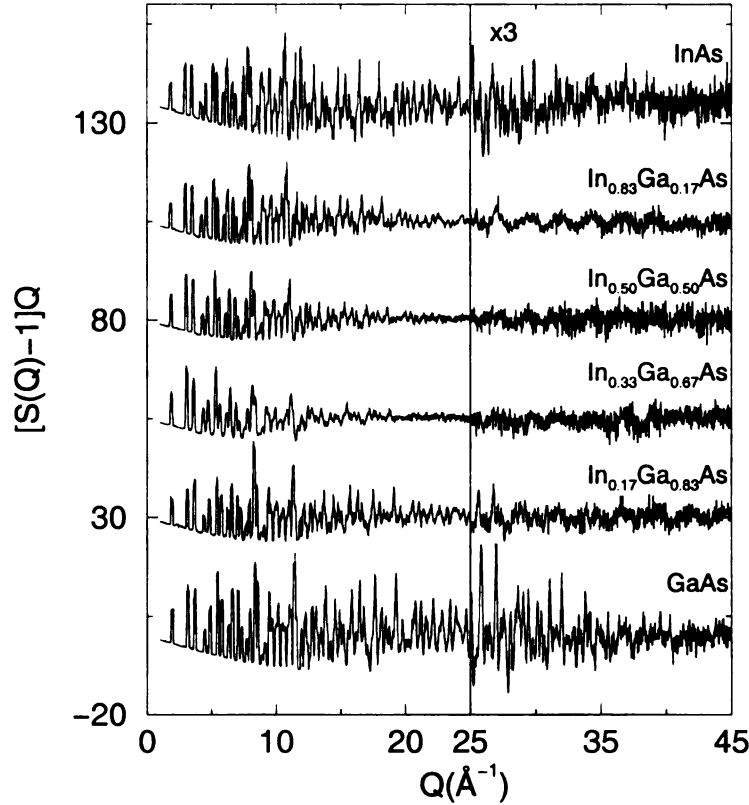
Figure 4.1: The reduced total scattering structure function $Q[S(Q)-1]$ of $In_xGa_{1-x}As$ alloys measured at 10K. The data-sets are offset for clarity. The high-Q region is shown on an expanded scale ($\times$ 3) to highlight the presence of diffuse scattering.

right peaks does not disperse significantly on traversing the alloy series. This shows that the local bond lengths stay close to their end-member values and do not follow Vegard's law, in agreement with the earlier XAFS [25] reports. However, already by 10 Å the structure is behaving much more like the average structure. For example, the doublet of PDF peaks around 11 Å in GaAs (Figure 4.2) remains a doublet (it doesn't become a quadruplet in the alloys) and disperses smoothly across the alloy series to its position at around 12 Å in the pure InAs. This shows that already by 10 Å the structure is exhibiting Vegard's law type behavior. It is also notable that for the nearest neighbor PDF peak, the peak widths are almost the same in both
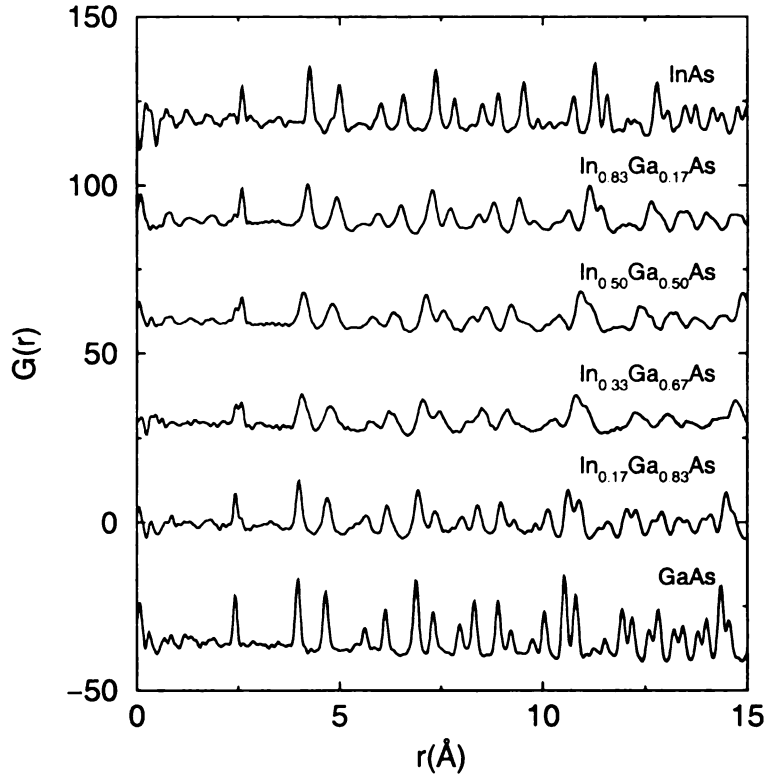
Figure 4.2: The reduced PDF, $G(r)$, of $In_xGa_{1-x}As$ alloys measured at 10 K. The data-sets are offset for clarity.

alloys and end-members but for the higher neighbors, the peaks are much broader in the alloys than in the end-members.

4.2.3 Bond length & bond length distributions in $In_xGa_{1-x}As$ alloys

We determined the bond lengths of Ga-As and In-As in the alloys from the first peak of $In_xGa_{1-x}As$ PDFs. Figure 4.3(a) shows the nearest neighbor PDf peaks of $In_xGa_{1-x}As$ alloys and Figure 4.3(b) shows the evolution of the bond length across the alloy series. Also shown is the room temperature XAFS data obtained by Mikkelson and Boyce [25]. We can notice that the individual Ga-As and In-As bond
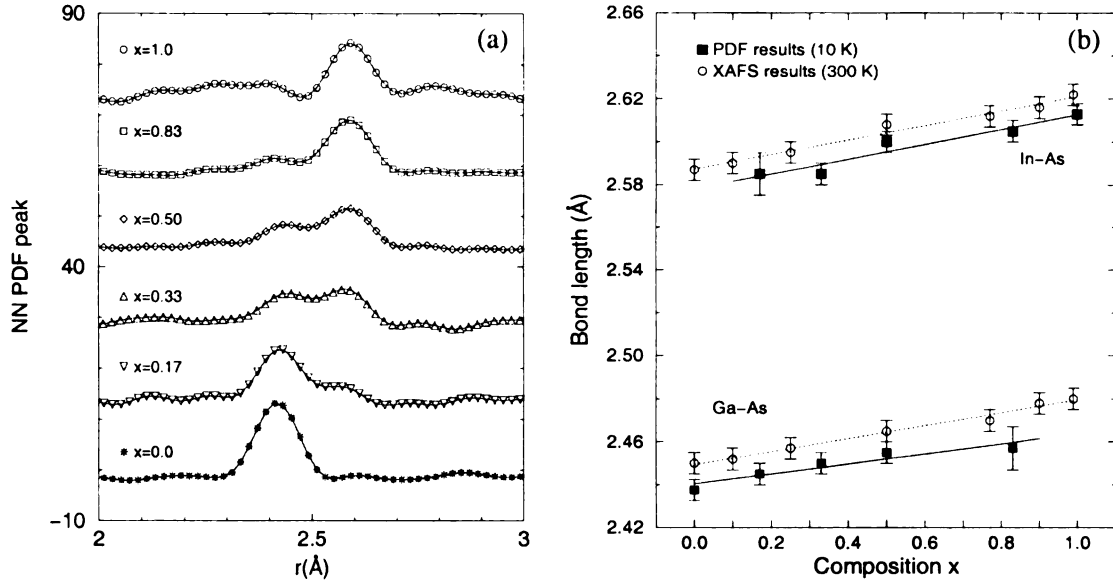
Figure 4.3: (a) NN PDF peaks in $In_xGa_{1-x}As$ alloys. (b) Solid symbols: Composition dependence of Ga-As and In-As bond lengths in $In_xGa_{1-x}As$ alloys obtained from PDF measured at 10 K. Open symbols: room-temperature XAFS results from Ref. [25].

lengths in the alloys are much closer to those of the end-member than the composition weighted average values. In addition, it shows quite good agreement with the XAFS results except a constant shift in bond lengths to smaller values by about 0.012 Å in the PDF-based results. This is presumably due to the difference in the measuring temperature; the PDF data are measured at 10 K whereas the XAFS data were collected at room temperature.

In $A_xB_{1-x}C$ type zinc-blende semiconductor alloys, the angle between A-C and B-C atom bonds is not orthogonal. Therefore, a displacement of the tetrahedron-centered C atom leads to a bond length change of all the nearest neighbor atoms. We obtained the bond length *distribution* from the PDF peak width. In the alloys, the PDF peak width (Δ) has both static and thermal contribution and can be modeled

in the following way [35];

$$\Delta^2 = \sigma_T^2 + \sigma_D^2, \tag{4.1}$$

where, σ_T and σ_D are peak broadening due to thermal and static disorder, respectively. The thermal contribution to the PDF peak width, σ_T, can be determined from the peak widths of the end-members in which no static disorder exists. In the alloys, we assume that σ_T is given by the linear interpolation of the two end-member values. Then, we can separate thermal and static contribution. Figure 4.4 shows the composition dependence of the nearest neighbor (NN) and far-neighbor PDF peak width. We can see that, for the NN peak, the additional broadening to PDF due to alloying is very small. It's less than 15% of the thermal broadening. This makes the accurate measurements of static bond length distribution very difficult even with our high real-space resolution PDF. The difference between Ga-As and In-As peak widths is less than 2.8% which is within the uncertainty of our measurements. However, the general trend shows that the Ga-As bond has a larger width than In-As bond. For a fully relaxed zinc-blende alloy structure, the bond length distributions for A-C and B-C bonds can be modeled as a single peak [76, 85]. In addition, the composition dependence of the static bond length distribution, σ_D can be modeled that

$$\sigma_D^2 = 4\Gamma_0^2 x(1-x). \tag{4.2}$$

Schabel *et al.* [76] calculated Γ_0^2 using the Keating potential model and obtained 0.000448 Å^2 and 0.000629 Å^2 for In-As and Ga-As bonds, respectively. In Figure 4.4(b) ($\triangle$-$\triangle$) and ($\triangledown$-$\triangledown$) show the In-As and Ga-As static peak width calculated with the Γ_0^2 given above. This shows reasonable agreement with the experimental static peak width. For far-neighbor PDF peaks, it is shown that the static contribution is up to five times larger than the thermal contribution. In addition, As-As pair peak width is almost three times larger than that of (In, Ga)-(In, Ga) pair. From
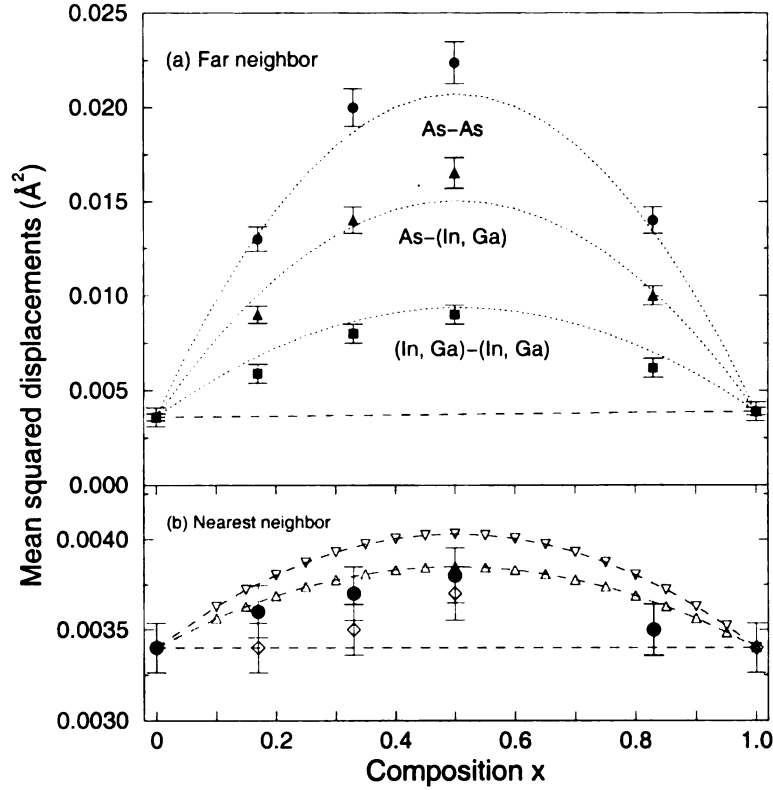
Figure 4.4: Square of the PDF peak widths for far-neighbors (a) and nearest neighbor (b) vs alloy composition, x. In (b), ● and ◇ represent the experimental Ga-As and In-As peak widths, respectively. The ($\triangle$-$\triangle$) and ($\triangledown$-$\triangledown$) are theoretical calculations for In-As and Ga-As bonds [76]. In (a), the straight dashed line is the thermal contribution to PDF peak width. The parabolic dotted curves are the calculations using the Kirkwood model. Note that for far-neighbor, the static contribution to the peak width is almost five times larger than that of the nearest neighbor [41].

this result, we can expect that the local distortion on the As sublattice is greater than the (In, Ga) sublattice distortion. This is understandable considering that (In, Ga) atoms always have four As neighbors, whereas As atoms have five different local environments.
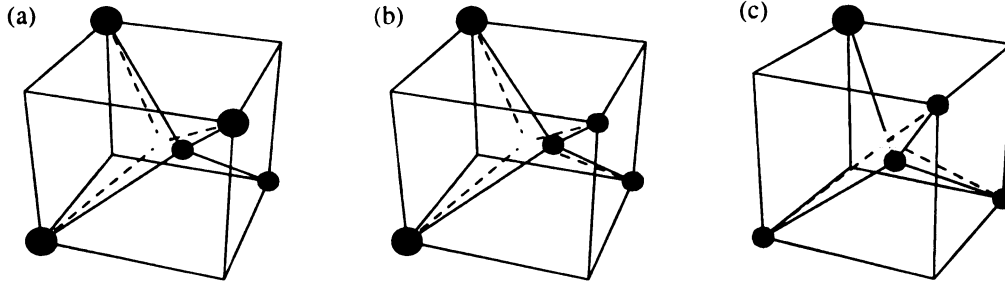
Figure 4.5: Schematic diagram of As displacements in cluster (a) type II, (b) type III, and (c) type IV. Cluster types are discussed in the text. At the corner, a large dark circle and small grey circle show In and Ga atom positions respectively. At the center, the grey and dark circles correspond to the As atom position before and after displacement.

4.3 Modeling the local structure of $In_xGa_{1-x}As$ semi-conductor alloys

4.3.1 Tetrahedral Cluster Model

The structural disorder in the $A_xB_{1-x}C$ type tetrahedral alloys can be intuitively visualized by considering simple tetrahedral clusters centered about C sites (the un-alloyed site). In the random alloy this site can have five distinct environments (4 A-neighbors (type-I), 3 A- and 1 B-neighbors (II), 2 A- and 2 B-neighbors (III), 1 A and 3 B-neighbors (IV) or 4 B neighbors (V)). We assume that the mixed site (A,B) atoms stay on their ideal crystallographic positions. By considering each cluster type in turn we can predict the qualitative nature of the atomic displacements present in the alloy. Let the A atoms be larger than the B atoms. In clusters of type I and V the C atom will not be displaced away from the center of the tetrahedron. As is shown in Figure 4.5, in type II clusters the C atom will displace away from the center directly towards the B atom. This is a displacement in a $\langle 111 \rangle$ crystallographic direction. In type III clusters it will displace in a direction between the two B atoms along a $\langle 100 \rangle$

62

crystallographic direction. Finally, in type IV clusters it will again be a $\langle 111 \rangle$ type displacement but this time in a direction directly away from the neighboring A atom. A simple model of the alloy can then be built up just by determining how many of each type of cluster are present and applying some simplifying approximations with regard to the size of the tetrahedron. In the random alloys, the probability of a mixed sublattice having an A atom is x and a B atom is $(1-x)$. Therefore, the probability of finding type I cluster is x^4; type II, $4x^3(1-x)$; type III, $6x^2(1-x)^2$; type IV, $4x(1-x)^3$ and type V, $(1-x)^4$.

Such a cluster model was used to make quantitative comparisons with the nearest neighbor bond distances observed in XAFS measurements [25] over the whole alloy series [27]. In this model, it is assumed that no static disorder exists on the mixed (In,Ga) sublattice. All cluster types have the same lattice parameter that is given by Vegard's law [86] for each concentration, x. Thus, the (In,Ga) sublattice form a virtual crystal and all the structural relaxation and atomic displacements are accommodated by displacing the As atoms from the centers of the tetrahedra in the manner described above. Each cluster is independently relaxed according to the prescription of Balzarotti et al. [27] to get the bond-lengths within each cluster type. In determining the magnitudes of the displacements, it is important to neglect both bond-bending and relaxation of atoms on mixed sites due to cancellation of errors. It causes large errors in the average bond length if only one of them is included [27]. Assuming a random alloy the number of each type of cluster that is present can be estimated using a binomial distribution. This gives the static distribution of bond lengths predicted by the model. These are then convoluted with the broadening expected due to thermal motion. This was determined by measuring the width of the nearest neighbor peaks in the end-member compounds, InAs and GaAs.

Starting from this simple cluster model, we studied how the local structure affects the NN peak shape and far neighbor peak widths in the PDF. The nearest neighbor PDF peak can be calculated from a linear combination of the different clusters present. This is shown in Figure 4.8(a). In order to calculate far neighbor peaks in the PDF a larger model must be constructed. A simple approach is to extend the clusters using periodic boundary conditions and take a linear combination of these ordered cluster models. However, this introduces atom-pair correlations which are not there in the real alloy [87]. In order to avoid this problem, we create a random alloy structure using program DISCUS [88]. First a $20 \times 20 \times 20$ cubic cell of InAs is generated. Then, the In atoms were randomly replaced by Ga atoms according to the concentration, x. The average lattice parameter of the model was determined using Vegard's law for the value of x under study. Each resulting cluster was then identified by type and the As atom was displaced in the appropriate direction by the amount obtained from calculation carried on the isolated cluster of that size. Now we have static local displacements in the model structure. However, in order to calculate a model PDF, we need to take into account one more factor, i.e. thermal atomic motion. As was discussed in Chapter 3, thermal atomic motion in crystals is correlated [31, 50], e.g. near-neighbor atoms tend to move in-phase with each other but far-neighbor atoms move independently. Due to this correlated atomic motion, near-neighbor peaks are sharper than the far-neighbor peaks in the PDF. The effect of correlated motion is taken into account in our calculation by describing the r dependence of the PDF peak width by $\sigma_0 = \sigma_c - \delta/r^2$ (Eq. 3.5). The uncorrelated thermal factors and sharpening parameter are refined using the program PDFFIT [64] in the pure end-members. To take into account the thermal broadening in the alloy, the thermal factors of In and Ga found in the pure end-members were used. For the As atoms, however, the average of two values found in the pure end-member was used [89]. The thermal factors used
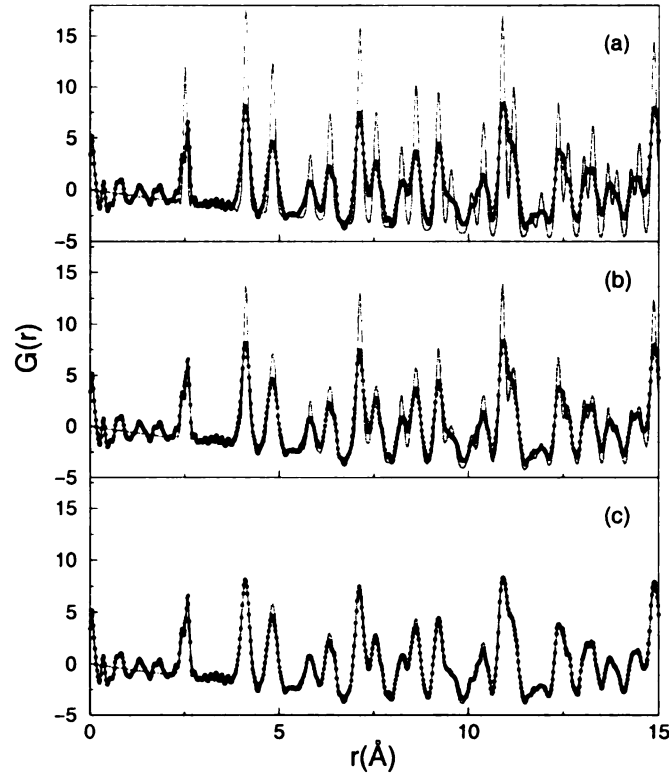
Figure 4.6: Experimental PDF (●—●) and cluster model PDF (–) of $In_{0.5}Ga_{0.5}As$. (a) Cluster model PDF is calculated using model structure which has chemical disorder (random distribution of In/Ga atoms) but no static disorder on both mixed (In,Ga) and As sublattices. (b) Static disorder on the As site is created using cluster models (see text) but no disorder on the (In,Ga) sublattice. (c) Disorder on the (In,Ga) sublattice is simulated by randomly displacing (In,Ga) atoms from their ideal sublattice (see text).

in this model are $U_{In} = 0.0445$ Å, $U_{Ga} = 0.0417$ Å, and $U_{As} = 0.0558$ Å, respectively. For the r-dependent sharpening of the PDF peaks, the parameter $\delta = 0.17$ Å^3 is used. With these information from end-members, the PDFs of the alloys can be calculated using the cluster model described above with no adjustable parameters.

In order to understand the contribution of the local distortion to the PDF peak widths, we first compared experimental PDFs with model PDFs calculated using the average structure (no static distortions on either sub-lattice) of the $In_{0.5}Ga_{0.5}As$ al-
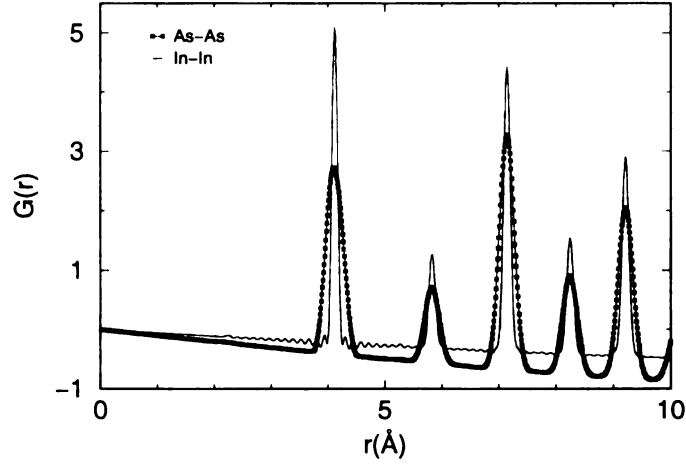
Figure 4.7: Partial PDF of In and As calculated using the Cluster model.

loy. The comparison is shown in Figure 4.6(a). We notice that *all peaks* in the model PDF are too sharp compared with the experimental PDF. Now we added the static disorder on arsenic sublattice using the method described in the cluster model. Figure 4.6(b) shows the comparison between the cluster model PDF which has static distortion on the As sublattice and the experimental PDF. We can see that the nearest neighbor doublet agrees reasonably well with the experiment. However, still *some peaks* in the model-PDF at higher-r are much sharper than those of the experimental PDF. In order to understand the origin of this difference, we calculated the As and In partial PDFs from the model. Figure 4.7 shows partial PDFs [90] of As and In in which only As-As and In-In pairs are shown. In this Figure, it is clear that the (As-As) correlations are much broader than those of (In-In) correlations. This suggests that the sharp peaks in the model PDF evident in Figure 4.6(b) are coming mostly from (In,Ga)-(In,Ga) correlations. The mismatch between the model and the experimental PDFs mainly comes from neglecting mixed (In,Ga) sublattice disorder in this model. To test this hypothesis we mimic the neglected static disorder on the mixed (In,Ga) sublattice. All In and Ga atoms in the mixed sublattice have four As

nearest neighbors. Since the (In,Ga) sublattice distortion is caused mainly by the second-neighbor distribution, we expect for the random alloys the second-neighbor distribution of (In,Ga) atoms is also random. From this, we assume that the static displacements of (In,Ga) atoms can be approximated as an isotropic distribution. Based on these arguments, we mimic the static disorder on the mixed (In,Ga) sublattice by randomly displacing (In,Ga) atoms from their ideal sublattice so that the overall static deviations have a Gaussian distribution. Figure 4.6(c) shows the comparison between the model PDF which has both As and (In,Ga) site disorder and the experimental PDF. Now the higher-r peaks in the model PDF become much broader and match the experimental PDF better.

We now focus on modeling the first peak of PDF. First of all, as we noted in the previous section, the additional peak broadening due to the bond length distribution is very small in the NN peaks. This result suggests that the peaks from different cluster types should line up with small dispersion. This is illustrated in Figure 4.8(b) which shows the NN PDF-peak for the $x = 0.5$ data-set. The solid line is calculated in the Pauling limit [23] where all nearest-neighbor bond-lengths are preserved at their values in the pure end-members. The broadening comes purely from thermal motion, again taken from the end-members. Clearly this reproduces the data quite well, though there is a small strain evident in the bonds decreasing the separation of the peaks in the doublet. The dashed line in this figure shows the peak profile that we obtain if we make the assumption that the nearest neighbor bond length changes in the alloy as seen in the "Z-plot" [25, 41], but there is no increase in the bond length distribution. Again, this gives rather good agreement emphasizing the fact that there is little additional peak broadening due to the alloying [41]. However, this effect is clearly exaggerated in the cluster model (Figure 4.8(a)). In the cluster model, bond-lengths vary significantly depending on the cluster type. These are
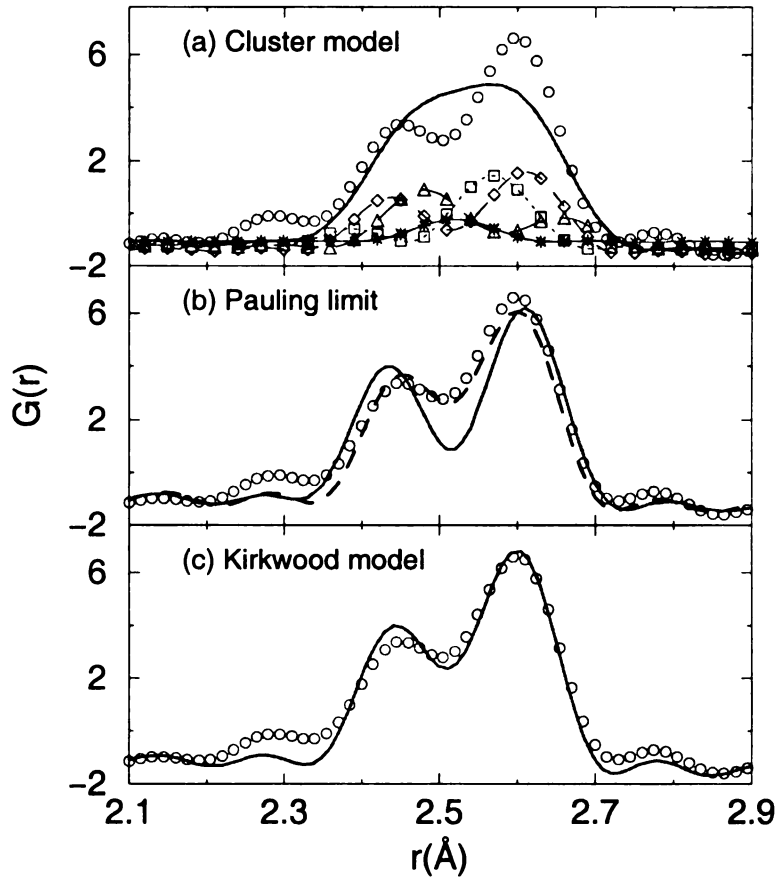
Figure 4.8: Comparison of the first peak in the experimental PDF (open circles) and model PDF (solid line) of $In_{0.5}Ga_{0.5}As$. (a) Tetrahedral cluster model with no disorder present on (In,Ga) sublattice. The sub-peaks represent the contributions from each type of cluster. Type I ($\times$), type II ($\square$), type III ($\diamond$), type IV ($\triangle$), and type V($*$). (b) The model PDF is calculated in the Pauling limit. The peak positions were obtained from the InAs and GaAs bond lengths in the end-members (solid line) and the InAs and GaAs bond lengths in the $In_{0.5}Ga_{0.5}As$ PDF (dashed line). See the text for details. (c) Kirkwood supercell model.

shown under the peak with their respective weights for the $x = 0.5$ sample. The symbol represents each type of cluster, type I($\times$), type II($\square$), type III($\diamond$), type IV($\triangle$), and type V($*$) respectively. The total model PDF is not resolved although it has a trace of double peaks. The cluster model successfully explains the sloping lines of the nearest neighbor bonds in the Z-plot [27], as exemplified by the agreement it gets with
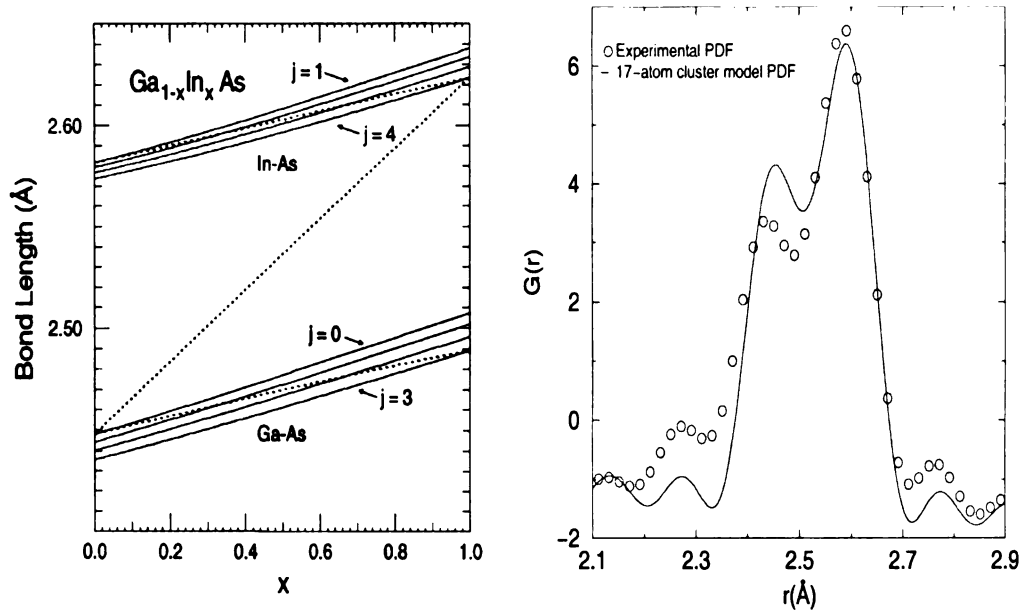
Figure 4.9: Left panel: Z-plot obtained using 17-atom cluster model [91]. Right panel: Comparison between experimental PDF and 17-atom cluster model PDF for $In_{0.5}Ga_{0.5}As$.

XAFS, but clearly does a poor job at explaining the nearest neighbor bond length distribution measured in the PDF. The major discrepancy is that too much intensity resides at, or close to, the undisplaced position leading to an unresolved broad first PDF peak in sharp contrast to the measurement. The disagreement is mainly due to the limited size of the clusters and is somewhat expected. The cluster models using larger clusters (17 atoms) improve the agreement with the experimental bond length distribution [78, 91] as is shown in Figure 4.9.
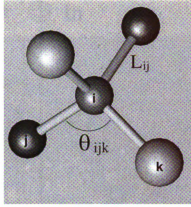
Figure 4.10: A sketch of the tetrahedron surrounding an impurity atom in the zinc-blende structure.

4.3.2 Supercell model based on the Kirkwood potential

A. Kirkwood model

A more realistic model for the structure of these alloys [41, 92] is obtained from a supercell relaxed using a Kirkwood potential given in Eq. 1.1 [67],

$$V = \sum_{<ij>} \frac{\alpha_{ij}}{2} (L_{ij} - L_{ij}^o)^2 + L_e^2 \sum_{<ij,ik>} \frac{\beta_{ijk}}{8} (cos\theta_{ijk} + \frac{1}{3})^2.$$

The potential contains nearest neighbor bond stretching (α_{ij}) and bond bending (β_{ijk}) force constants. In the relaxed supercell model, the force constants were adjusted to fit the PDFs of the end-members [26] with $\alpha_{Ga-As} = 96$ N/m, $\alpha_{In-As} = 97$ N/m, $\beta_{Ga-As-Ga} = \beta_{As-Ga-As} = 10$ N/m and $\beta_{In-As-In} = \beta_{As-In-As} = 6$ N/m. The additional angular force constants required in the alloy are taken to be the geometrical mean, so that $\beta_{Ga-As-In} = \sqrt{(\beta_{Ga-As-Ga} \cdot \beta_{In-As-In})}$. The PDFs for the alloys could then be calculated in a self-consistent way for all the alloys with no adjustable parameters [92]. Figure 4.11 shows the relaxed alloy structure for the $In_{0.5}Ga_{0.5}As$ alloy. The deviations of As atoms from their average positions are evident. In this model, the lattice dynamics are also included. Starting with the force constants and the
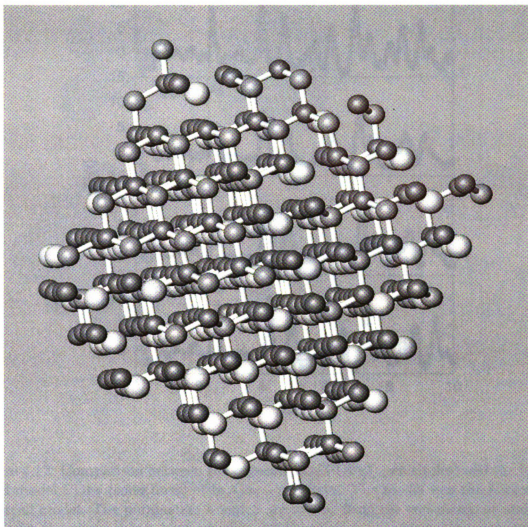
Figure 4.11: Relaxed structure of $In_{0.5}Ga_{0.5}As$ alloy. The deviation of As atoms from their average positions are evident [50]

Kirkwood potential, the thermal broadening of the PDF peaks at any temperature can be determined directly from the dynamical matrix [41, 92]. The model-PDF is plotted with the data in Figure 4.12. The excellent agreement with the data over the entire alloy range suggests that the Kirkwood potential provides an adequate starting point for calculating distorted alloy structures in these III-V alloys. Note that in comparison with experiment, the theoretical PDF has been convoluted with a Sinc
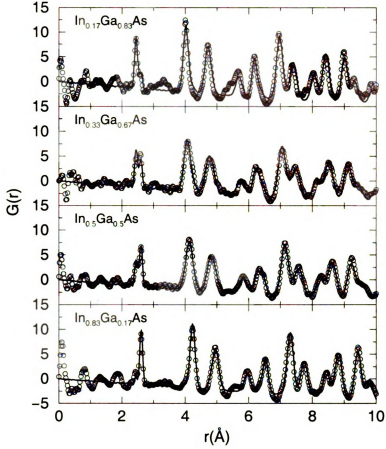
Figure 4.12: Comparison between the experimental PDFs (open circles) and the Kirkwood model PDFs (solid lines) of $In_xGa_{1-x}As$ alloys. The model was the Kirkwood supercell model. The parameters α and β are refined from the end-members and the PDFs for the alloys shown here are then calculated with no adjustable parameters.

function to incorporate the truncation of the experimental data at $Q_{max} = 45$ Å.

B. 3-dimensional atomic probability distribution

Now, we analyze the relaxed alloy structures obtained using a Kirkwood potential to get the average three dimensional atomic probability distribution of As and (In,Ga) atoms. Figure 4.13 shows iso-probability surfaces for the As site in the $In_xGa_{1-x}As$ alloy. The probability distributions were created by translating atomic positions of the displaced arsenic atoms in the supercell ($20 \times 20 \times 20$ cubic cell) shown in Figure 4.11
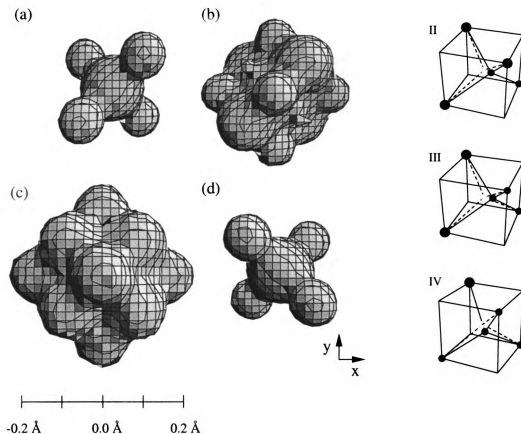
Figure 4.13: Iso-probability surface of the ensemble averaged As atom distribution. The surfaces plotted all enclose the volume where As atoms will be found with 68 % probability. (a) $In_{0.17}Ga_{0.83}As$ (b) $In_{0.33}Ga_{0.67}As$ (c) $In_{0.50}Ga_{0.50}As$ (d) $In_{0.83}Ga_{0.17}As$. In each case, the probability distribution is viewed down the [001] axis. Also shown is the cluster types II, III, and IV.

into a single unit cell. To improve statistics, this was done 70 times. The surfaces shown enclose a volume where the As atom will be found with 68 % probability. The probability distribution is viewed down the [001] axis. It is clear that the As atom displacements, though highly symmetric, are far from being isotropic. The same procedure has been carried out to elucidate the atomic probability distribution on the (In,Ga) sublattice. The results are shown in Figure 4.14, plotted on the same scale as in Figure 4.13. In contrast to the As atom static distribution, the (In,Ga)

(a) (b)

(c) (d)

-0.2 Å   0.0   0.2 Å

y, x
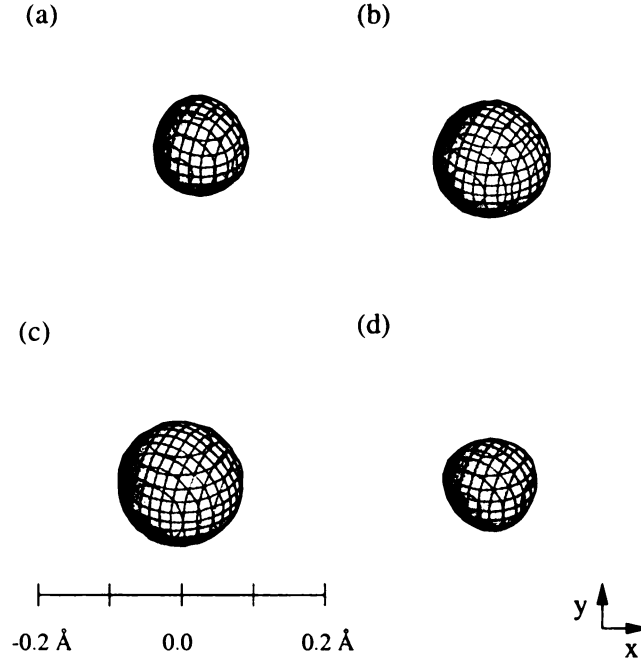
Figure 4.14: Iso-probability surface of the ensemble averaged (In,Ga) atom distribution. The surfaces plotted all enclose the volume where As atoms will be found with 68 % probability. (a) $In_{0.17}Ga_{0.83}As$ (b) $In_{0.33}Ga_{0.67}As$ (c) $In_{0.50}Ga_{0.50}As$ (d) $In_{0.83}Ga_{0.17}As$. In each case, the probability distribution is viewed down the [001] axis. These surfaces are plotted on the same scale as those in Figure 4.13.

probability distribution is much more isotropic and sharply peaked in space around the virtual crystal lattice site.

In all compositions, the As atom distribution is highly anisotropic as evident in Figure 4.13 with large displacements along $\langle 100 \rangle$ and $\langle 111 \rangle$ directions. This can be understood easily within cluster model as we discussed in Section 4.3.1. The $\langle 100 \rangle$ displacements occur in type III clusters and the $\langle 111 \rangle$ displacements occur in type II and IV clusters. This also explains why, in the gallium rich alloy in which the three and four Ga cluster is dominant, the major As atom displacements are along $[111]$, $[1\bar{1}\bar{1}]$, $[\bar{1}1\bar{1}]$, and $[\bar{1}\bar{1}1]$ as we observed in Figure 4.13(a). On the contrary, in the indium rich alloy, the major displacements are along $[\bar{1}\bar{1}\bar{1}]$, $[\bar{1}11]$, $[1\bar{1}1]$, and $[11\bar{1}]$, as

Table 4.1: Standard deviation of the As and (In,Ga) atom distributions in $In_xGa_{1-x}As$ alloys obtained from the Kirkwood model. The numbers in parentheses are the estimated error on the last digit. For both As, and (In,Ga) atoms, $\sigma = \sigma_x = \sigma_y = \sigma_z$. See text for details.

	x=0.17	x=0.33	x=0.50	x=0.83
$\sigma(As)$ (Å)	0.072(1)	0.092(1)	0.097(1)	0.074(1)
$\sigma(In,Ga)$ (Å)	0.044(1)	0.058(1)	0.060(1)	0.048(1)
$\frac{\sigma(In,Ga)}{\sigma(As)}$	0.61	0.63	0.62	0.61

can be clearly seen in Figure 4.13(d).

The atomic probability distribution obtained from the Kirkwood model for the (In,Ga) sublattice is shown in Figure 4.14. As we discussed, this is much more isotropic (though not perfectly so), and more sharply peaked than the As atom distribution. However, contrary to earlier predictions, [27] and borne out quantitatively by the supercell modeling, *there is significant static disorder associated with the (In,Ga) sublattice.* In order to compare the magnitude of the static distortion of the (In,Ga) sublattice with that of the As sublattice, we calculated the standard deviation, σ, of the As and (In,Ga) atomic probability distributions. This was calculated using $\sigma_i = \sqrt{\frac{1}{N-1}\sum_{k=1}^{N}(d_i(k))^2}$, $(i = x, y, z)$, where d_i refers to the displacement from the undistorted sublattice of atoms in the model supercell in x, y, and z directions, and N is the total number of atoms in the supercell. Table 4.1 summarizes the values of σ for the As and (In,Ga) atomic probability distributions in the alloys. It shows that for all compositions the static disorder on the (In,Ga) sublattice is around 60% of the disorder on the As sublattice. These static distortions give rise to a broadening of PDF peaks as is evident in Figure 4.2. To evaluate the static contribution to the PDF peak broadening, σ_D, from the $\sigma's$ reported in Table 4.1 we used the following

expression:

$$\sigma_D^2 = \sigma_a^2 + \sigma_b^2, \tag{4.3}$$

where a, b can be As, or (In,Ga). For example, for $x = 0.5$ alloy, we get $\sigma_D^2 = 0.0188(4)$ Å^2 for As-As peaks in the PDF, $0.0130(4)$ Å^2 for As-(In,Ga) peaks and $0.0072(3)$ Å^2 for (In,Ga)-(In,Ga) peaks. These values are in good agreement with the mean square static PDF peak broadening of As-As, As-(In,Ga) and (In,Ga)-(In,Ga) peaks, shown in Figure 4.4 of $0.0187(1)$ Å^2, $0.0128(1)$ Å^2, and $0.0053(1)$ Å^2 respectively.

4.4   Correlated atomic displacements in In$_x$Ga$_{1-x}$As alloys

We have shown that on the average, atomic displacements of As atoms in In$_x$Ga$_{1-x}$As alloy are highly directional. In this section, we would like to address the question whether these atomic displacements are correlated from site to site. To investigate this we have calculated theoretically the diffuse scattering intensity which would be obtained from the relaxed Kirkwood supercell model and compare it with the known experimental diffuse scattering. The Figure 4.15 shows diffuse scattering of In$_{0.5}$Ga$_{0.5}$As alloy calculated using the DISCUS program [88]. In this calculation the Bragg-peak intensities have been removed. Strong diffuse scattering is evident at the Bragg points in the characteristic butterfly shape pointing towards the origin of reciprocal space. This is the Huang scattering which is peaked close to Bragg-peak positions and has already been worked out in detail [93]. In addition to this, clear streaks are apparent running perpendicular to the [110] direction. The diffuse scattering calculations on (hkl) planes where $l \neq 0,$ integer (Figure 4.16), show that these diffuse streaks are extended along the $[hhl]$ direction consisting of sheets of diffuse scattering per-
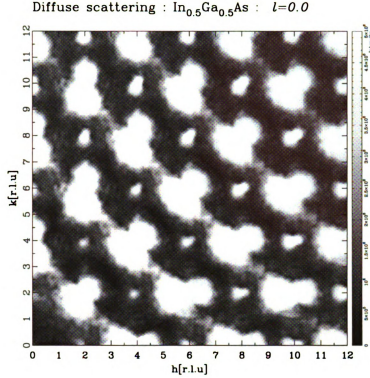
Figure 4.15: Single crystal diffuse scattering intensity obtained from the relaxed super-cell model for the $In_{0.5}Ga_{0.5}As$ alloy. The cut shown is the diffuse intensity expected in the $(hk0)$ plane of reciprocal space. Bragg peaks have been removed for clarity. See text for details.

pendicular to the [110] direction of reciprocal space. Diffuse scattering with exactly this (110) symmetry was observed in the TEM study of $In_{0.53}Ga_{0.47}As$ [94]. Careful observation of our calculated diffuse scattering indicates that the diffuse scattering has a maximum on the low-Q side of the $(hh0)$ planes passing through the Bragg points, with an intensity minimum on the high-Q side of these planes. This is charac-teristic size-effect scattering obtained from correlated atomic displacements due to a mismatch between chemically distinct species as recently observed in a single-crystal diffuse scattering study on $Si_{1-x}Ge_x$ [95], for example. This asymmetric scattering was clearly observed in the earlier diffuse scattering study on $In_{0.53}Ga_{0.47}As$ [94].

The single-crystal diffuse scattering intensity which is piled up far from the Bragg-
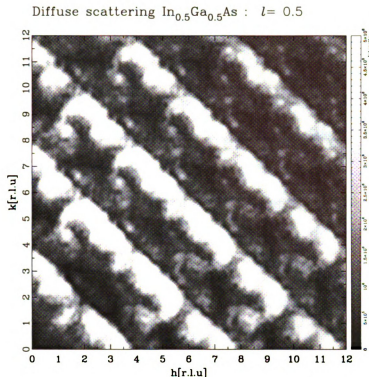
Figure 4.16: Single crystal diffuse scattering intensity obtained from the relaxed supercell model of the $In_{0.5}Ga_{0.5}As$ alloy. The cut shown is the diffuse intensity expected in the $(hk0.5)$ plane of reciprocal space. Bragg peaks have been removed for clarity. See text for details.

points is giving information about intermediate range ordering of the atomic displacements. It is interesting that it is piled up in planes perpendicular to [110] whereas the local atomic displacements are predominantly along $\langle 100 \rangle$ and $\langle 111 \rangle$ directions. This observation underscores the complementarity of single-crystal diffuse scattering and real-space measurements such as the PDF. The real-space measurements are mostly sensitive to the *direction and magnitude of local atomic displacements* and less sensitive to how the displacements are correlated over longer-range (though this information is in the data). On the other hand, the single crystal diffuse scattering immediately yields the intermediate range correlations of the displacements but one has to work harder to extract information about the size and nature of the local

atomic displacements. Used together these two approaches, together with XAFS, can reveal a great deal of complementary information about the local structure of disordered materials.

The single crystal diffuse scattering suggests that atomic displacements are most strongly correlated (i.e., correlated over the longest range) along [110] directions although the displacements themselves occur along $\langle 100 \rangle$ and $\langle 111 \rangle$ directions. The reason may be that the zinc-blende crystal is stiffest along [110] directions because of the elastic anisotropy in the cubic crystal. This was shown for the case of InAs and was used to explain why the 5th peak in the PDF (coming from In-As next neighbor correlations along [110] direction) was anomalously sharp in both experiments and calculations [31]. If the material is stiffer in this direction, one would expect that strain fields from displacements will propagate further in these directions than other directions in the crystal correlating the displacements over longer range. These are consistent with the displacement pair correlation function calculation by Glas [96] which shows that the correlation along $\langle 110 \rangle$ directions is larger than correlations along $\langle 100 \rangle$ and $\langle 111 \rangle$ and extends further.

Chapter 5

Discussion and Conclusions

The high real-space resolution PDF measurements of $In_xGa_{1-x}As$ alloys provide more complete structural information such as bond length, bond length distributions, and far-neighbor distances and distributions. The bond lengths from the PDF showed good agreement with those of the XAFS measurements. The high real-space resolution PDF measurement made possible the separation of thermal and static bond length distributions in the alloys. The static bond length distributions in the alloys are less than 15 % of thermal broadening at 10 K. This result shows that the accurate measurements of static distribution becomes more difficult at higher temperatures. In addition, the composition dependence of NN PDF peak width shows that the In-As bond has a larger distribution than the Ga-As bond. The Keating [76] and Kirkwood model [30] also show two different bond length distributions for In-As and Ga-As bonds in the alloys. Similar results were obtained in $In_xGa_{1-x}P$ alloys using Keating model that Ga-P bond length distributions are larger than those of In-P [89]. In addition to the NN information, the PDF gives far-neighbor pair distributions which help to understand a global picture of semiconductor alloys. The far-neighbor distributions show that static distribution becomes dominant in peak width broadening although it is less than 15% of thermal broadening for NN.

The model structure of III-V $In_xGa_{1-x}As$ alloys was obtained from a supercell relaxed using the Kirkwood potential. The resultant Kirkwood model PDFs show good agreement with experimental PDFs in predicting the bond length, bond length distribution, and far-neighbor pair distributions without adjustable parameters. Recently, it is also shown that the Kirkwood model is successful for more polar II-VI $ZnSe_{1-x}Te_x$ alloys [97]. The 3-dimensional As atom iso-probability surface obtained from the relaxed supercell shows that the As atom displacements are very directional and symmetric. On the contrary, the (In,Ga) atom displacements are more or less isotropic. The directional properties of As atom displacements are well understood with the help of a simple cluster model. The cluster model intuitively explains the As atom displacements for various nearest neighbor configurations.

In the Kirkwood model, we assumed that (In,Ga) atom distributions are random according to the concentration, x. However, in reality the concentration fluctuation leads to the cluster formation [81]. The Monte-Carlo simulation based on the Keating potential shows a tendency (7~10 %) of repulsion between first NN Indium pairs and attraction between second NN pairs [83] in the bulk $In_xGa_{1-x}As$ alloys (x=0.05, 0.2). Recent simulations on Cu_3Au show that the PDF can differentiate differences in the occupational disorder (clustering) in the same sample at different temperatures [98]. In real experiments, it will be more demanding to detect any difference coming from the clustering effect due to the noises and error in the data. However, these results open a possibility of using the PDF analysis to extract chemical short range order information in crystalline materials.

In addition to the atomic displacements and distributions in the alloys, the single crystal diffuse scattering calculation of the relaxed supercell reveals a correlation in static displacements of atoms. The diffuse scattering shows that the atomic dis-

placements are *correlated* over longer range along [110] directions although the displacements of As atoms are along ⟨100⟩ and ⟨111⟩ directions. This result shows the complementarity of single crystal diffuse scattering and real-space measurements such as the PDF; the real-space measurements are mostly sensitive to the direction and magnitude of local atomic displacements but the single crystal diffuse scattering yields the intermediate range correlations of the displacements. This suggests that if used together these two approaches can reveal a great deal of complementary information about the local structure of disordered materials.

Besides local static distortions, the PDF measurements can probe the relative thermal motions of atoms in semiconductor compounds. In the PDF the near-neighbor peaks are sharper than those of far-neighbor pairs due to the correlation in near-neighbor thermal motions. The comparison of correlated atomic motion in Ni and InAs shows that the details of the correlation in atomic motion depends on the strength of interatomic interaction and configuration of atom pair. The correlated thermal motions in simple materials are well explained using the Correlated Debye model without any adjustable parameters. The Correlated Debye model is simple but picks up most features of the r_{ij} dependence of the PDF peak width.

The relative motions of nearest neighbor pair atoms are mainly determined by the bond stretching force constant of a material. Therefore from the NN PDF peak width, it is possible to estimate the bond stretching force constant. The temperature dependence of NN peak width, σ_{NN}, can be parameterized [99, 100] by the Einstein frequency, ω_E as $\sigma_{NN}^2(T) = \frac{\hbar}{2\mu\omega_E} \coth(\hbar\omega_E/2kT)$, where μ is a reduced mass and ω_E is the Einstein frequency. The Einstein frequencies and corresponding force constants of several As-crystalline and glass compounds determined from the temperature of NN peak width are in reasonable agreement with the bond stretching force constants

measured from Raman and infrared spectra of same materials [101]. This result shows the possibility of measuring force constants from PDF the peak width.

We determined bond stretching and bond bending force constants of semiconductor compounds by fitting the nearest neighbor and far-neighbor peak widths to the lattice dynamic calculations using the Kirkwood model. The refined bond stretching and bond bending force constants show 10%~30% difference from the literature values [12]. However, since the literature values also containes errors around 10%~30% [26], it is not easy to estimate the accuracy of force constants refined using the PDF. In addition, we used only two data points, nearest and far-neighbor peak widths, to refine two force constants in our refinement. Therefore this could lead relatively large errors in the refined force constants. Especially, bond bending force constant which is mainly determined by the far-neighbor peak width show relatively large variation. Recently, force constants in Ni and CaF_2 were determined from the PDFs of these materials [102]. In this method, one-phonon diffuse scattering is calculated by varying the force constant until the resultant PDF best matches the experimental PDF for the whole r-range. The phonon dispersion curves calculated using these refined force constants show good agreement with the phonon dispersion curves measured by the inelastic neutron scattering. However, in this study only the one-phonon contribution to the PDF peak width sharpening is counted. As Thorpe et $al.$ [103] pointed out, however, the one-phonon contribution recovers only around 90% of the peak sharpening effect and at least two-phonon contributions should be included to recover 95% of the peak sharpening of the NN PDF peak. In addition, the accurate correction for the effects of an instrument resolution function to the PDF peak width broadening [102, 103] should be applied. More fundamentally, in the PDF the diffuse scattering which contains information about interatomic force constants are averaged over all directions. This raises questions about how accurately the force

83

constants can be determined using the PDF method. We expect that more systematic studies should be conducted both theoretically and experimentally to understand the limitations and potentials of PDF method in determining the interatomic force constants.

Finally, we like to mention that most high real-space resolution PDF measurements [41, 97] of semiconductor alloys are carried out for bulk materials. However, many semiconductor alloys used in real applications are in the form of thin film. In addition, a recent XAFS experiment [91] on strained $In_xGa_{1-x}As$ thin-alloy film grown on GaAs(001) shows very interesting results. The individual Ga-As and In-As bond lengths in the thin-alloy film are contracted from their bulk-alloy values due to the strain imposed on the layer by the substrate. As in the bulk material, however, XAFS gives only nearest neighbor information about the thin-alloy film. This limits our understanding of the external strain effects on the overall alloy structure. An important future development would be the ability to study the high real-space resolution PDFs of the thin film.

APPENDIX

User's Manual

PDFgetX

Version 1.1

Ilkyoung Jeong

Jeroen Thompson

Thomas Proffen

Simon Billinge

Department for Physics and Astronomy
Michigan State University
East Lansing, MI, 48824-1116, USA

Contact: *billinge@pa.msu.edu*

Preface

Disclaimer

By downloading the program PDFgetX, you agree to the terms and conditions concerning its use specified in the license agreement that is provided as part of the distribution. End users wishing to make commercial use of the software must contact Libraries, Computing & Technology, Michigan State University, East Lansing, MI 48824; (517)353-0722 prior to any commercial distribution to discuss terms. The Software is provided to End User by MSU on an as is basis. No user support is provided or implied.

MSU makes no warranty, express or implied to end user or to any other person or entity. Specifically, MSU makes no warranty of merchantability or fitness for a particular purpose of the software. MSU will not be liable for special, incidental, consequential, indirect or other similar damages, even if MSU or its employees have been advised of the possibility of such damages, regardless of the form of the claim.

Using PDFgetX

Publications of results totally or partially obtained using the program **PDFgetX** should state that **PDFgetX** was used and contain the following reference:

> JEONG, I.-K., THOMPSON, J.,PROFFEN, TH., PEREZ, A. AND BILLINGE, S. J. L. "PDFgetX, a program for obtaining the atomic Pair Distribution Function from X-ray powder diffraction data" *J. Appl. Cryst.* (2001), submitted.

Acknowledgments

A.1 Introduction

A.1.1 What is PDFgetX

PDFgetX is a program to be used to obtain the atomic Pair Distribution Function (PDF) from a measured X-ray powder diffraction data. PDFgetX is written using the Yorick, an interpreted language. This will require users to obtain the Yorick distribution and install it yourself. See Chapter A.2 for help in installation.

PDF is the instantaneous atomic number density-density correlation function which describes the atomic arrangement in materials. A useful characteristic of PDF method is that it gives both *local* and *average* structure information because both Bragg peaks and diffuse scattering are used in the analysis. And from the PDF peak width, it's possible to obtain the information about bond-length distribution (static, thermal) [41] and correlated atomic thermal motion [31]. By contrast, an analysis of the Bragg scattered intensities alone, by a Rietveld type analysis for instance, yields the *average* crystal structure only and the extended x-ray absorption fine structure(EXAFS) gives nearest-neighbor and next nearest-neighbor distance information. PDF analysis method has long been used to characterize glasses, liquids and amorphous materials. Recently, however, it has found more application in the study of local structural disorder in crystalline materials, where some deviation from the *average* structure is expected to take place.

Obtaining total scattering structure function (and PDF) from raw diffraction data requires many corrections for experimental effects such as absorption, polarization corrections and removing of Compton and multiple scattering contribution to the elastic scattering. Also it needs proper error propagation to be used in modeling of PDF using either PDFFIT (real-space Rietveld) [64] or a Reverse Monte Carlo approach [105] using e.g. DISCUS [88] to yield structural parameters. PDFgetX allows users to do all these data corrections and error propagation in convenient ways. During the refinement, PDFgetX displays each correction effect to the raw data and saves all the parameters used for refinement. This makes the refinement processes easy to understand and allows reproducible results. PDFgetX supports the following data formats: multi-column ascii file, SPEC and multi-channel analyzer(MCA) files.

To find out about recent updates of PDFgetX or to get further information visit the PDFgetX homepage at the following site:

http://www.pa.msu.edu/cmp/billinge-group/programs/PDFgetX

A.2 Installation

A.2.1 System Requirements

PDFgetX should run on any UNIX/Linux platform supported by Yorick. This includes PC/Unix and SGI. It also run on Windows NT and 95. For a list of systems on which PDFgetX is known to work, see Table A.1. If you successfully install PDFgetX on a system not included in this list, please contact us and let us know. If you cannot install PDFgetX on a system, and have studied the documentation thoroughly, please contact us and ask for help. Without access to a similarly configured system, we may not be able to help you with the installation, but see Section A.2.2.4 for instructions on how to report your trouble.

Table A.1: Known Platforms Supporting PDFgetX

Hardware	Operating System
Intel 486	RedHat Linux 6.0
	Windows 95/NT
DEC-ALPHA	Digital Unix
SGI	Irix

A.2.2 What You Need

A.2.2.1 Yorick

Before you can run PDFgetX, you will need to install Yorick. PDFgetX is written in the Yorick language, which is an interpreted C-like language (and it's free). The distribution of PDFgetX contains only the source code files for PDFgetX; it does *not* come with Yorick. The latest version of Yorick can be downloaded from the official site:

ftp://wuarchive.wustl.edu/languages/yorick/yorick-ad.html

This document provides no information about installing Yorick; see the Yorick readme files for help with the installation and checking that the installation was successful. Before installing PDFgetX, be sure that your installation of Yorick works.

A.2.2.2 PDFgetX

You may obtain the latest version of PDFgetX from the PDFgetX website:

http://www.pa.msu.edu/cmp/billinge-group/programs/PDFgetX

PDFgetX is provided as a compressed file. Use the command

```
tar -xzvf pdfgetx1.1.tar.gz
```

which will extract the files into a new directory called "PDFgetX/". And you can find the following program files under the directory PDFgetX/.

```
        pdfgetx.i, pdfgetxdistribution.i, pdfgetx_custom.i
ASF.DAT, PERIODIC_TABLE.DAT, MASS_ABS_COEFF.DAT, LICENSE.TXT
```

If the -z flag does not work on your system, then use the commands

```
gzip -d pdfgetx1.1.tar.gz, tar -xvf pdfgetx1.1.tar
```

to extract the files.

A.2.2.3 Installing and Configuring PDFgetX

To customize the PDFgetX installation, you need to modify two files, "custom.i" and "pdfgetxdistribution.i". If you are new user of "Yorick", you can simply rename "pdfgetx_custom.i" (included in compressed file) to "custom.i" and give the proper path for the "Actual_PATH" in the following two lines in "pdfgetx_custom.i" file.

```
#include "Actual_PATH/pdfgetx.i"
#include "Actual_PATH/pdfgetxdistribution.i"
```

And then create a directory "/Yorick" under your home directory and place your own version of "custom.i" there. If you already have your own version of "custom.i", simply add the above two lines in the "custom.i" file.

For Windows OS, you need to beware of a few things. First, the path should look like the following: "/c/pdfgetx/..". Second, in windows OS, users can set the size of font and graphic window in "custom.i" file. Therefore it is better to copy the "custom.i" file coming with the Yorick Window version and add the above two lines there than just rename "pdfgetx_custom.i" to "custom.i". Finally, remember that if the directory name has a space (" ") as in "My Directory", the Yorick couldn't find the directory.

After configuring the "pdfgetx_custom.i" file, if you open the file "pdfgetxdistribution.i" using a text editor, you will find the following code:

```
asf_file="Actual_PATH/ASF.DAT"
periodic_table="Actual_PATH/PERIODIC_TABLE.DAT"
mabscoeff_file ="Actual_PATH/MASS_ABS_COEFF.DAT"
```

again, give the proper path for the "Actual PATH". These code set paths for three important data files: Atomic scattering factor, Periodic table, and Mass absorption coefficient. Also, the variable name, e.g. asf_file, should not be changed, otherwise PDFgetX couldn't find these data files.

If you want to print graphs directly from PDFgetX, you need to edit the file "pdfgetxdistribution.i" and change the following line:

$$printer\_string = "lpr -h -Prm31 \_\_temp.ps".$$

Modify the printer string to reflect your system. When printing, PDFgetX creates a temporary postscript file called "_temp.ps" and makes a system call to print the file. Do not change the name of the file in the printer string or printing will not work. For windows OS, "lpr" command doesn't work, instead use "print" command. This is a DOS command and it seems it sends the graph to a printer connected via "LPT1" port. If this setting is not working, we would recommend windows OS users to use another method to print graphs. First, save the graph as a postscript (PS) file or window meta file (WMF) using [S] option in the main menu, and open it using ghostview (PS file) or using MS word (WMF file). Then print the graph using print command in the program.

A.2.2.4 Report problems and suggestions

If you have any problems in installing & running PDFgetX and have any suggestions about the PDFgetX, please send email to the following address:

billinge@pa.msu.edu
http://www.pa.msu.edu/cmp/billinge-group/programs/PDFgetX.html

A.3 Tutorial: $In_{0.33}Ga_{0.67}As$ Semi-conductor Alloy

Now you might have installed PDFgetX and can start it simply by typing **pdfgetx** at Yorick prompt. In this tutorial, you'll get a chance to analyze $In_{0.33}Ga_{0.67}As$ semi-conductor alloy data collected at Cornell High Energy Synchrotron source (CHESS) using intense x-rays of 60 KeV ($\lambda = 0.206$ Å). The tutorial files can be downloaded from the PDFgetX homepage. In this experiment, the incident x-ray energy was selected using a Si(111) double-bounce monochromator. The data were collected at 10 K to minimize thermal atomic motion in the sample, and hence increase the sensitivity to static displacement of atoms due to alloying using a closed cycle helium refrigerator mounted on the Huber 6 circle diffractormeter. All the signal measured was saved to a file using the system controlling software, SPEC.

The signal measured using the intrinsic Ge solid state detector was processed in two ways. Using single-channel pulse-height analyzer (SCA), the elastic scattering, Compton scattering, and elastic + Compton scattering were collected separately. In the measurements using SCA, the proper energy window setting for the elastic scattering is very important because any error in the window setting could cause an unknown contamination to the elastic scattering thus make data corrections very difficult. At the same time, the signal was fed to multi-channel analyzer (MCA) to record the complete energy spectrum of each value of Q. The elastic and Compton scattered radiation could then be separated using software after measurement. Collecting data using MCA has advantages and disadvantages. In the MCA method, since the entire energy spectrum of the scattered radiation is measured at each value of Q, the error caused by the mis-set of energy window is negligible. The main disadvantage of the MCA method is that it has a larger dead-time, although this can be reliably corrected [106].

This tutorial is composed of two subsections, "Preliminary Data Analysis" and "Refine structure function". The "Preliminary Data Analysis" section is mainly concentrated on how to reduce SPEC and MCA file to build PDFgetX *input file* for structure refinement. In "Refine structure function" section, the step by step procedure of structure function refinement is presented. Users can build the *input file* using tutorial SPEC file in "Preliminary Data Analysis" section or use a tutorial *input file* coming with the program. In this manual, *SPEC file* refers to the data collected using SCA and *MCA file* for the data collected using MCA.

A.3.1 Preliminary Data Analysis

A.3.1.1 Reduction of SPEC file

The raw data from x-ray powder diffraction measurements using either a sealed x-ray tube or synchrotron source could have many different file formats and could contain multiple scans that ought to be averaged together. Therefore it is very difficult to use the raw data directly in the structure function refinement. With these things in mind, we limited the "Preliminary Data Analysis" to support only the SPEC file format and N-column ascii file format. For details about SPEC file format, please refer to Appendix App.a This section will show you how to reduce the raw SPEC data into the *input file* from which to start analysis. This process includes extracting scans from SPEC file, comparison of different scans, applying dead-time correction and combining different scans.

In general, one SPEC file contains many scans. The following shows a scan header of SPEC file collected at CHESS.

#L pmQ ereal elive Epoch Seconds IC1 IC3 I_CESR PULSER TOTAL COMPTON IC2 ELASTIC

During the SPEC file reduction process, we will use *column number* to refer to a specific variable such as *ELASTIC, IC2, PULSER, etc* , so you need to remember which column corresponds to which variable. Follow along with this example terminal output. It will guide users to learn about how the "Reduction of SPEC file" works. The comments in /* ... */ mark are added just for explanation purpose and will not be shown in the real analysis.

```
current directory> yorick

 Copyright (c) 1996.  The Regents of the University of California.
 All rights reserved.  Yorick 1.4 ready.  For help type 'help'

> pdfgetx
```

   Pair Distribution Function from the X-ray powder diffraction (PDFgetX 1.1)

```
    0) Preliminary data reduction
    1) Build a setup file
    2) Background Substraction
    3) Reduction of Structure Function: S(Q)
        Input file format: (Q, I, dQ, dI)
    4) PDF calculation: G(r)
        Input file format: (Q, S(Q), dQ, dS)
    P) Print, S) Save, U) Unzoom, L) Limits windows
    Q) Quit

    [0-4 qsulp] 0 /* Enter to the Preliminary data reduction level */

    1) Extract Scan(s) from SPEC file
    2) Compare N-column(N>=2) ascii files
```

93

```
3) Combine N-column(N>=2) ascii files
4) Build PDFgetX input format: (Q, I, dQ, dI)
5) Convert MCA file to N-column ascii file
Q) Return to Main


[1-5Q] 1


The Input should be SPEC file format : Continue (y/n)? y


ENTER SPEC FILE NAME TO READ: in33_tutorial.spec
  - The following shows scan information in in33_tutorial.spec


  #S  1  601  pts -->  ascan  pmQ 1 13    600 1
  #S  2  601  pts -->  ascan  pmQ 1 13    600 1
  #S  3 1401  pts -->  ascan  pmQ 12 40  1400 1
  #S  4 1401  pts -->  ascan  pmQ 12 40  1400 1
  #S  5 1401  pts -->  ascan  pmQ 12 40  1400 1
  -------------------------------------------------


EXTRACT SCANS FROM SPEC FILE:
  - Each scan will be saved as an ascii file
  - Enter all scans to be read: [Ex: 2 4 5] 1 2 3 4 5
    /* Extract good scans by entering the scan number */


SAVE SCANS TO ASCII FILE:
  - Output file name will be 'samplename_scannumber.asc'
  - Enter your 'samplename' [Ex. InAs] : in33


Return to Preliminary data reduction
-----------------------------------------------------------------
```

Now each scan is saved as ascii file. As it is mentioned during extracting process, the file name will be "in33_1.asc", "in33_2.asc", and so on. Now we can compare these different scans.

```
[1-5Q] 2 /* Compare N-column (N>=2) ascii files */

 The Input should be N-column ascii file format :
 Plot y(=data/norm) vs. x(=q). Continue (y/n)? y


ENTER FILE NAMES TO COMPARE, TO QUIT READING, ENTER 'Q':
  - File name to compare : in33_1.asc


    #L pmQ ereal elive Epoch Seconds IC1 IC3 I_CESR PULSER TOTAL COMPTON IC2 ELASTIC


    ASSIGN COLUMN NUMBER TO VARIABLES:

      - Column # corresponding to X-axis : 1
      - Column # corresponding to DATA   : 13

      - Normalization of data :
          for constant normalization, enter '0'
```

```
                - Column # corresponding to NORM.   : 12



ENTER FILE NAMES TO COMPARE, TO QUIT READING, ENTER 'Q':
   - File name to compare : in33_2.asc


   .

   .


ENTER FILE NAMES TO COMPARE, TO QUIT READING, ENTER 'Q':
   - File name to compare : in33_5.asc

ENTER FILE NAMES TO COMPARE, TO QUIT READING, ENTER 'Q':
   - File name to compare : q
-------------------------------------------------------
/* Dead-time correction setting */

READ FILE : in33_1.asc

   APPLY DEAD-TIME CORRECTION FOR DATA (y/n)? y

      1) Dead-time correction using detector dead-time
      2) Dead-time correction using pulser measurement
      Q) Exit Dead-time correction

      [1-2Q] 2

      Enter column # containing pulser : 9

   APPLY DEAD-TIME CORRECTION FOR MONITOR (y/n)? n
   /* For details, refer to CH. 4 Using PDFgetX */

   CHECK VARIABLE AND ASSIGNED COLUMN #

      - X-axis                        : 1
      - DATA                          : 13
      - Normalization                 : 12

      Detector dead-time Correction using pulser
         - Pulser column              : 9

      No Monitor dead-time Correction

   CHANNEL SETTINGS ARE CORRECT (y/n)? y

READ file: in33_2.asc


   .

   .


READ file: in33_5.asc

Colors in order of reading: magenta, cyan, blue, green, red, and blacks
```

Comparison of scans after dead-time correction
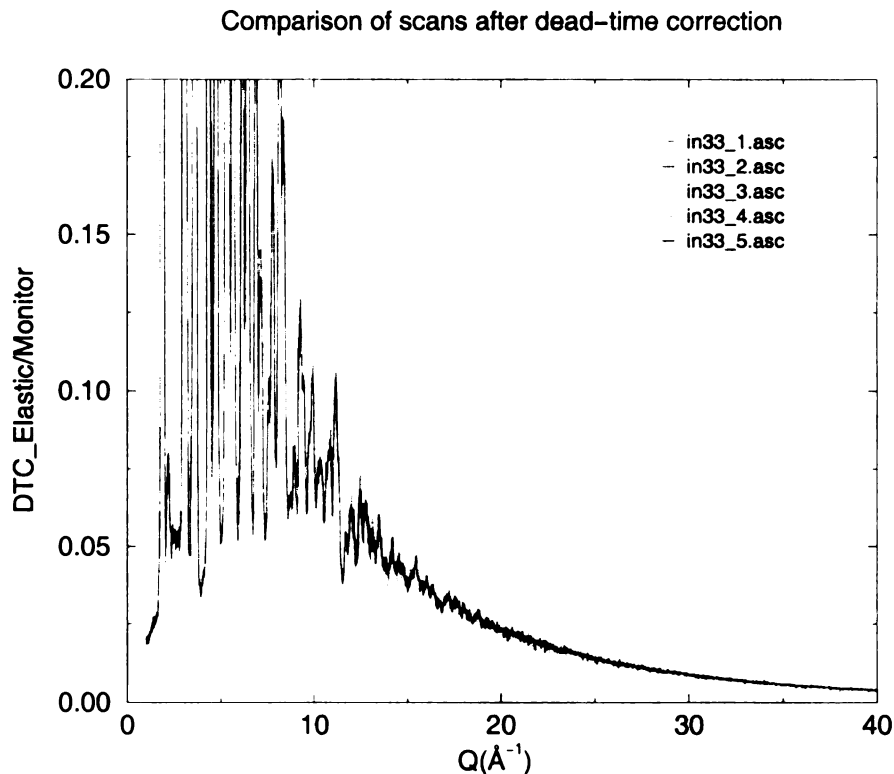
Figure A.1: Comparison of normalized elastic scattering in five scans after dead-time correction. It shows that the elastic scattering in each scan overlap with each other quite nicely.

```
COMPARE OTHER VARIABLE (y/n)? n

EXIT COMPARING FILES:

Return to Preliminary data reduction
-------------------------------------------------------------------------
```

Figure A.1 shows dead-time corrected elastic scattering after normalization by monitor. It shows that these scans overlap with each other quite nicely. Maybe it's good to check how the comparison looks like if the dead-time correction is not applied. Since the normalized elastic scattering from different scans overlap with each other, we can combine all of them.

```
[1-5Q] 3 /* Combine N-column (N>2=2) ascii file */

The Input should have N-column ascii file format !
The X-axis column should have constant step(dX)  !
Combine upto five variables: X-axis(Q, Two-theta)!
DATA, NORM, and Aux1, Aux2 (auxiliary variables) !
Continue (y/n)? y
```

ENTER FILE NAMES TO COMBINE, TO QUIT READING, ENTER 'Q':
  - File name to combine : in33_1.asc

   #L pmQ ereal elive Epoch Seconds IC1 IC3 LCESR PULSER TOTAL COMPTON IC2 ELASTIC

   ASSIGN COLUMN NUMBER TO VARIABLES:

     - If the column # is set to '0', the corresponding variable
     - will not be propagated !!

     - Column # corresponding to X-axis : 1
     - Column # corresponding to DATA   : 13
     - Column # corresponding to NORM. : 12
     - Column # corresponding to Aux1   : 0
     - Column # corresponding to Aux2   : 0

ENTER FILE NAMES TO COMBINE, TO QUIT READING, ENTER 'Q':
  - File name to combine : in33_2.asc
  .
  .

ENTER FILE NAMES TO COMBINE, TO QUIT READING, ENTER 'Q':
  - File name to combine : in33_5.asc

ENTER FILE NAMES TO COMBINE, TO QUIT READING, ENTER 'Q':
  - File name to combine : q

READ file : in33_1.asc

  Apply DEAD-TIME CORRECTION FOR DATA (y/n)? y

     1) Dead-time correction using detector dead-time
     2) Dead-time correction using pulser measurement
     Q) Exit Dead-time correction

     [1-2Q] 2

     Enter column # containing pulser : 9

  APPLY DEAD-TIME CORRECTION FOR MONITOR (y/n)? n

  CHECK VARIABLE AND ASSIGNED COLUMN #

     - X-axis   : 1
     - DATA   : 13
     - Normalization   : 12
     - AUX1   : 0
     - AUX2   : 0

97

```
        Detector dead-time Correction using pulser :

            - Pulser column                    : 9

        No Monitor dead-time Correction

      CHANNEL SETTINGS ARE CORRECT (y/n)? y


    READ file : in33_2.asc
        .

        .


    READ file : in33_5.asc

    Enter variable name corresponding to X-axis: Q
    Enter variable name corresponding to DATA  : Elastic
    Enter variable name corresponding to NORM. : Monitor

    SAVE COMBINED DATA:
        - Enter file name for combined data: in33_tutorial.comb

    Make sure the X-column and combined variables have a correct value !

    Return to Preliminary data reduction
    ----------------------------------------------------------------
```

We just obtained combined N-column ascii file. The next step is to convert it to the PDFgetX input format: (Q, I, dQ, dI). Here Q is the magnitude of scattering vector and defined as $Q = 4\pi \sin(\theta)/\lambda$. I is the intensity of elastic scattering normalized by the monitor, dQ and dI are errors in Q and I. In this tutorial we'll not preprocess the background data. It'll be given as 4-column (Q, I, dQ, dI) format.

```
    [1-5Q] 4 /* Build PDFgetX input file */

    The Input should be N-column(N>=2) ascii file
    All columns should have same number of lines
    Blanks and commas in columns are not permitted
    Continue (y/n)? y

    ENTER FILE NAME TO READ: in33_tutorial.comb
        - Enter number of comment(and blank) lines in the data header : 2

    CHECK FILE FORMAT:

        1) Column contains Q/Two-theta?      : 1
            - Data in Q or Two-theta value?   : Q
        2) Column contains Intensity?        : 2
        3) Column contains Monitor/Time?     : 0
            - Normalization by Monitor or Time?: No Normalization
        x) Exit.

    [1-3X] 3
```

```
      Column contains Monitor/Time? : 3
        - Normalization by Monitor or Time(M/T)? m

      1) Column contains Q/Two-theta?       : 1
         - Data in Q or Two-theta value?    : Q
      2) Column contains Intensity?         : 2
      3) Column contains Monitor/Time?      : 3
         - Normalization by Monitor or Time?: Monitor

      x) Exit.

      [1-3X] x

    SAVE PDFgetX INPUT FILE (Q, I, dQ, dI):
      - Enter file name to for input file: in33_tutorial.input

    Return to Preliminary data reduction
    ------------------------------------------------------------------
```

Now, you obtained the *input file* for the structure function refinement. If the X-column is 2θ, then the program converts it to Q.

A.3.1.2 Reduction of Multi-Channel Analyzer (MCA) data

The MCA file format could be different depending on the instruments. Therefore here we assume an MCA file format which we used in the data reduction process. The MCA file format we used is attached in Appendix A.c. In this file, the scattered intensity at every Q point is distributed to the whole MCA channels. So each block which is separated by blank corresponds to each Q point. In order to convert this file to the normal N-column ascii file, we need to know the following information: Minimum Q or two-theta, number of data points, Q/two-theta step (this should be constant), total channel number of MCA. Many of these information can be obtained using "scan_summary" function which is a part of PDFgetX. We will not provide whole MCA file to do the analysis but just one MCA file to show you how it works. However we can tell that the structure function obtained using SPEC and MCA data are basically same.

```
    [1-5Q] 5 /* Convert MCA file to N-column ascii file */

    File should have MCA file format: Continue (y/n)? y

    ENTER MCA FILE NAME TO READ: in33_tutorial.mca
      - Build an X-axis column of corresponding MCA data
      - The X-axis should be either 'Q' or 'Two-theta'
      - The X-axis should have constant step (dX)

      - Enter variable name corresponding to X-axis, [Q/TT] : q

      - Enter minimum Q value             : 36
      - Enter number of data points       : 251
      - Enter Q step                      : 0.02
```

```
      - Total channel number of MCA          : 1024

READING MCA DATA, BE PATIENT!!

SET UP THE INTEGRAING REGIONS OF MCA SPECTRUM:
   - Propagate upto four variables:
       Elastic, Elastic+Compton, Aux1 and Aux2
   - If the starting and ending channel number of a variable
   - is same, the corresponding variable will not be propagated

   - Start of elastic channel            : 639
   - Stop of elastic channel             : 657
   - Start of elastic_compton channel    : 470
   - Stop of elastic_compton channel     : 657
   - Start of MCA auxiliary channel 1    : 0
   - Stop  of MCA auxiliary channel 1    : 0
   - Start of MCA auxiliary channel 2    : 0
   - Stop  of MCA auxiliary channel 2    : 0

read-write binary stream: _mcachannel
  In directory: /home/jeong/analysis/gainas/data/in50/mcafile/
  /* Open a binary file to save MCA channel setting */

CHECK SETTING OF MCA CHANNEL

   1) Start of elastic channel           : 639
      Stop of elastic channel            : 657
   2) Start of elastic_compton channel   : 470
      Stop of elastic_compton channel    : 657
   3) Start of MCA auxiliary channel 1   : 0
      Stop  of MCA auxiliary channel 1   : 0
   4) Start of MCA auxiliary channel 2   : 0
      Stop  of MCA auxiliary channel 2   : 0
   Q) Exit MCA channel setting

   Enter to reset channel setting [1-4Q] : q

INTEGRATE REGIONS OF INTEREST!!

SAVE MCA DATA TO ASCII FILE:
   - Enter file name for MCA-derived data: in33_mca.dat

READ ANOTHER MCA FILE(y/n)?  n

EXIT MCA FILE READING:

Return to Preliminary data reduction
-------------------------------------------------------------------
```

Figure A.2 shows MCA spectrum of $In_{0.33}Ga_{0.67}As$ at $Q=40\text{Å}^{-1}$. The elastic and Compton scattering are well separated at this value of Q. It also shows some fluorescence peaks in low channel number side. If you check the output file, you'll find that it contains Q, MCA_Elastic, MCA_ElaCompt, and MCA_Det_Tot. When the

MCA Spectrum of : $In_{0.33}Ga_{0.67}As$
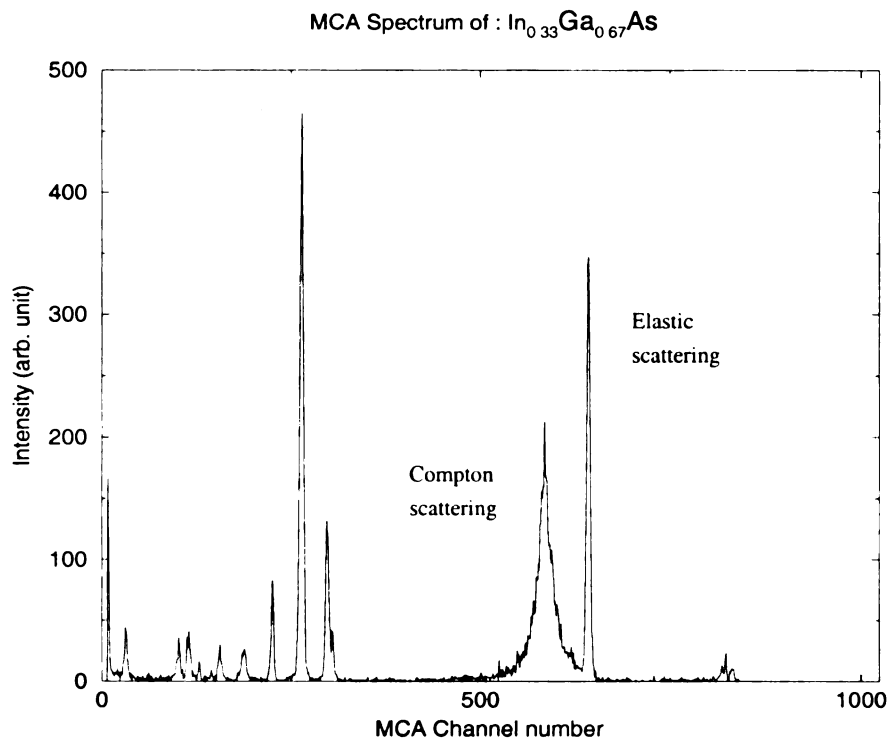
Figure A.2: MCA spectrum of $In_{0.33}Ga_{0.67}As$ at $Q=40\text{Å}^{-1}$. It shows that the very sharp elastic scattering around channel number 640 is well separated from the broad Compton scattering. The fluorescence of the alloy are shown below channel number 300.

program generates X-column, it assumes constant X-step. The whole MCA files can be converted to N-column ascii files in this way and then as we did in "Reduction of SPEC file" these files can be compared and combined. Also it's possible to apply dead-time correction for MCA file.

A.3.2 Refine structure function of $In_{0.33}Ga_{0.67}As$

Now we are almost ready to refine structure function of $In_{0.33}Ga_{0.67}As$ semiconductor alloy except two more things; building setup file and background subtraction.

```
[0-4 qsulp] 1 /* Enter to Build a setup file in Main */

BUILD SETUP FILE:
----------------------------------------------------------------
Note that the setup file is a text file written
using Yorick syntax, and may be modified in emacs without going
through this whole procedure of building a new one.

If PDFgetX crashes, check the (text) input file very closely!
```

```
------------------------------------------------------------------

ENTER THE TYPE OF INCIDENT X-RAY RADIATION:
  - [S]ilver, [M]olybdenum, [C]opper or enter [E]nergy [smce]? e
  - Enter Energy of incident X-ray (KeV) : 59.67

SAMPLE INFORMATION:
  - Number of elements in the sample[Ex. InGaAs => 3]? 3

  - Element #: 1
  - Enter the element (ions not yet supported) : in
  - Enter fractional composition: 0.33

  - Element #: 2
  - Enter the element (ions not yet supported) : ga
  - Enter fractional composition: 0.67

  - Element #: 3
  - Enter the element (ions not yet supported) : as
  - Enter fractional composition: 1

  - Enter absorption coefficient*thickness of sample, mu*t: 1.11

MONOCHROMATOR INFO.:

  1) d-spacing of monochromator: 3.135
  2) Position of monochromator : incident_beam
  3) Type of monochromator     : perfect_cryst
  Q) Exit

  [123Q] Q

SAVE SETUP FILE AS: in33_tutorial.setup
------------------------------------------------------------------
```

You've finished creating a setup file which contains information about the sample composition and experimental setup. You may take a look at the setup file using a text editor and check what you have there. Also you can add some more comment using Yorick syntax if you want. The final step before starting refinement is to subtract background. Because the sample itself affects magnitude of background, sometimes instrument background (background measured without sample) over estimate the real background. So in background correction, the program allows users can change the magnitude of background by multiplying correction constant in order to make it match data more nicely in low Q.

```
[0-4 qsulp] 2 /* Enter to Background substraction in Main */

The Input should be 4-column ascii file(Q, I, dQ, dI)
Continue (y/n)? y

ENTER DATA FILE NAME TO READ        : in33_tutorial.input

ENTER BACKGROUND FILE NAME TO READ : in33_bkg.input
```

```
BACKGROUND SUBTRACTION:
  - Multiply correction constant to background to make
  - it match data more nicely in low Q (y/n)? n
  - 30 negative intensities set to 0.000208106.
  /* negative value are set to minimum intensity */

ENTER FILE NAME FOR BACKGROUND CORRECTED DATA: in33_cfbg.input
------------------------------------------------------------------

[0-4 qsulp] 3  /* start structure function refinement */

ENTER SETUP FILE NAME: in33_tutorial.setup

READ INPUT FILE: It should be 4-column ascii file(Q, I, dQ, dI)
  - Enter data file name to read:  in33_cfbg.input

DATA REDUCTION :

read-write binary stream: _history.pdb
  In directory: /u24/jeong/PDFgetX/manual/
  /* Open binary file to save refinement history. Refer to the Appendix A.b */


SMOOTH DATA USING SAVITZKY & GOLAY METHOD (y/n)? n

Flat Symmetric [R]eflection or [T]ransmission geometry (r/t)? t
/* Choose either symmetric flat reflection or transmission geometry  */

------------------------------------------------------------
Flat Plate Symmetric Transmission Geometry Data Correction
------------------------------------------------------------

WINDOW 0: CORRECTION EFFETS ON RAW DATA !

APPLY MULTIPLE SCATTERING CORRECTION (y/n)? y
  - Does the data contain Compton scattering in high Q (y/n)? n
  - Multiple scattering calculation in transmission geometry

WINDOW 3: MULTIPLE SCATTERING RATIO!

APPLY POLARIZATION CORRECTION (y/n)? n
  => Polarization correction NOT applied!

APPLY ABSORPTION CORRECTION (y/n)? y

NORMALIZATION USING MID-HIGH Q PART OF DATA
  - Enter a mid-range Q value (roughly 26.4): 25
  - 751 points are used for normalization
  - Approximate normalization constant: 1904.38

WINDOW 1: CORRECTED DATA vs. TIS!
```
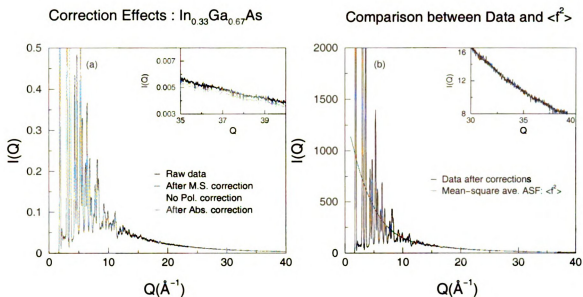
Figure A.3: (a) Corrections on raw data of $In_{0.33}Ga_{0.67}As$ semiconductor alloy. In high Q region, after each correction, the change of slope is noticeable. (b) Comparison between normalized data after corrections and mean-square average atomic scattering factor, $\langle f^2 \rangle$. In high Q, those two line up quite nicely.

```
ENTER NORMALIZATION CONSTANT: 1920

APPLY COMPTON SCATTERING CORRECTION
  - Apply Compton correction in MID-LOW Q region using 'Ruland' method.
  - Enter integral width 'b' (try 0.008): 0.003
  - For details, please refer to the MANUAL !!

WINDOW 4: <f^2>, Compton, and Modified Compton by the Ruland function

WINDOW 2: REDUCED STRUCTURE FUNCTION, Q*(S(Q)-1)!

CHECK IF F(Q) = (S(Q)-1)*Q IS APPROXIMATELY 0 AT HIGH Q
  - Is F(Q) approximately 0 at high Q (y/n)? y

SAVE STRUCTURE FUNCTION, S(Q), TO ASCII FILE:
  - Enter file name to save data: in33_tutorial.soq
-------------------------------------------------------------------
```

Now you've obtained structure function. Before we move on, let's examine the corrections applied during data reduction. First, Figure A.3(a) shows corrections on the raw data. Each correction effect is not significant, however, the changes of slope is noticeable in high Q region. Figure A.3(b) shows comparison between normalized data after all correction and total independent scattering(TIS). We can see that TIS lines up with data in high Q region nicely. Figure A.4 shows absorption factor, double scattering, Compton scattering and modified Compton scattering by the Ruland
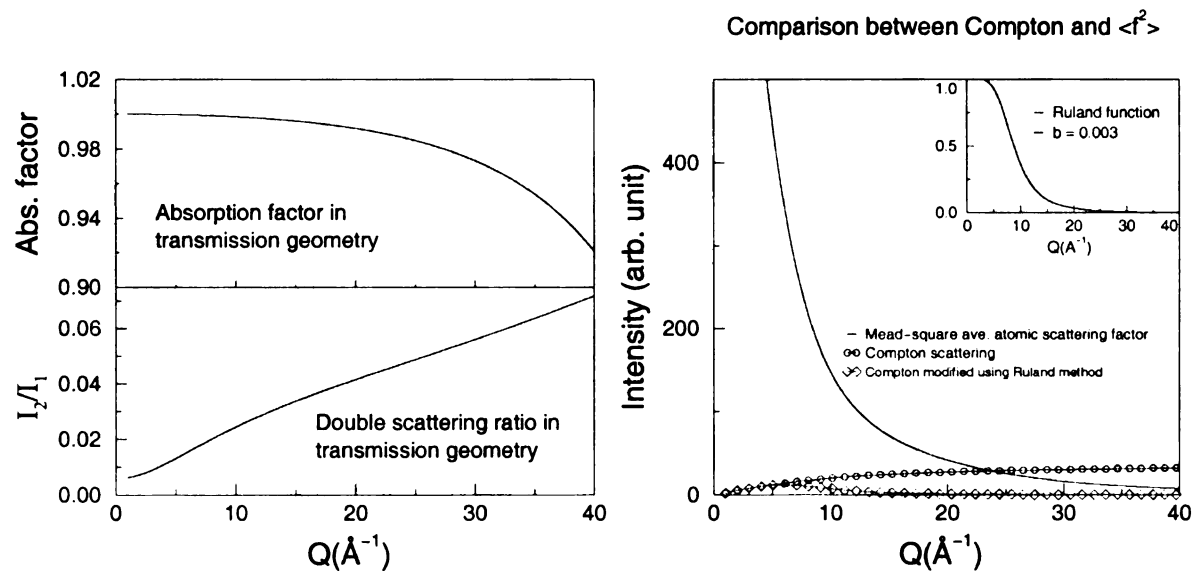
Figure A.4: Data corrections in $In_{0.33}Ga_{0.67}As$ semiconductor alloy: (a) Absorption factor ($\mu t = 1.11$). Absorption effect becomes larger as Q increases. (b) Double scattering ratio. (c) Comparison between mean-square average atomic scattering factor, $\langle f^2 \rangle$, Compton (o), and modified Compton (◇) using the Ruland function. Inset shows the Ruland function for the integral width, b=0.003.

function. Finally Figure A.5(a) shows reduced structure function of $In_{0.33}Ga_{0.67}As$ semiconductor. The oscillating diffuse scattering is clear in high Q region. Table A.2 shows all the inputs used in the refinement. Now let's calculate Pair Distribution Function(PDF) using the structure function just we obtained.

```
[0-4 qsulp] 4 /* PDF calculation: G(r) */
```

Table A.2: Summary of structure function refinement

Input file	in33_tutorial.input
Background file	in33_bkg.input
Setup file	in33_tutorial.setup
Smoothing	No
Geometry	Tramsmission
Multiple Scattering Correction	Yes Compton in high Q region is discriminated
Polarization Correction	No
Absorption Correction	Yes
Normalization Constant	1920
Compton Correction	Remove mid-low Q Compton intensity using Ruland method. Integral width, b = 0.003
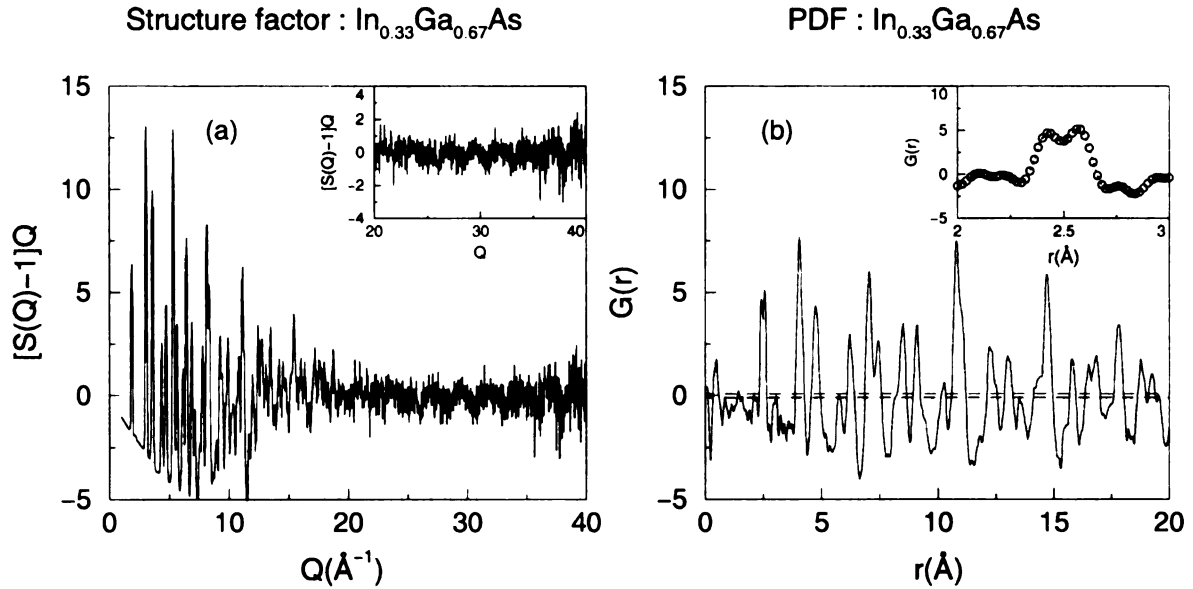
Figure A.5: (a) Reduced Structure Function of $In_{0.33}Ga_{0.67}As$ semiconductor. The high Q data shows oscillating diffuse scattering. (b) Pair Distribution Function of $In_{0.33}Ga_{0.67}As$ semiconductor. The nearest-neighbor peak is split into a doublet corresponding to shorter Ga-As and longer In-As bonds

```
CALCULATE PAIR DISTRIBUTION FUNCTION(PDF): G(r)
  - Read structure function: (Q, S(Q), dQ, dS)

ENTER FILE NAME: in33_tutorial.soq
  - Enter Qmax at which to cut the data: 40
  - Read structure function from Q = 1 to Q = 40
  - Enter maxmimum range, r(Angstrom) for PDF calculation: 20
  - Enter PDF step size(dr): 0.02

Calculating PDF up to rmax=20 with dr=0.02.

  - SAVE PDF: (r, G(r), dr, dG) (y/n)? y
  - Enter file name to save data: in33_tutorial.pdf

  - Recalculate PDF (y/n)? n
-----------------------------------------------------------------
```

Congratulations! You've made a PDF. Figure A.5(b) shows pair distribution function of $In_{0.33}Ga_{0.67}As$ semiconductor alloy. The nearest-neighbor(NN) peak shows well resolved doublet which corresponds to shorter Ga-As and longer In-As bonds. This clearly shows the power of high real-space resolution PDF method to study the local structure of the alloy. It could be instructive to obtain the PDF using different Q_{max} to see how it affects the shape of NN peak. The dotted line shows ± one standard deviation(σ) of PDF; the error propagated to PDF from the raw data. The ripples

around sharp peaks are known as the termination ripple. It is caused by the limited Q value in Sine Fourier transform. And the noise peaks near to $r=0$ are caused by noises in the data.

A.4 Using PDFgetX

This chapter will teach you how to **use** PDFgetX. For this purpose, first we'll give you overview of PDFgetX. And then explain how the program works; we will explain the structure function refinement process.

A.4.1 Overview of PDFgetX

Before learning the specific commands and procedures to control PDFgetX, it is best to understand how PDFgetX works in a very general way. This section documents the "broad overview" of PDFgetX while the following sections discuss the specifics at length.

The function of PDFgetX is to produce PDFs from x-ray powder diffraction data, whether from an sealed tube x-ray source or from a synchrotron source. Obviously, to begin the analysis one requires the *raw data*. The raw data, however, is in general too "raw" for analytical processing; not only does every facility has a different data file format, but the data file could contain multiple scans that ought to be averaged together. PDFgetX can help reduce the raw data into a more convenient format from which to start the analysis, but ultimately the responsibility for doing so will lie with the end user.

The *input file* from which PDFgetX can start the analysis contains the averaged intensities. Please be aware of the possible name confusion that can occur: the *raw data file* refers to the file that is directly output from the computer (like SPEC file) whereas the *input file* refers to a input data which will be used for the calculation of structure function, S(Q). Some information regarding the experiment (such as the wavelength used) and some information regarding the specimen characteristics (such as the stoichiometry) are required in order to apply proper correction. The experiment and specimen information are contained in a *setup file* that is required at every step of the analysis.

With the *setup file* and the *input file*, the analysis can begin. The first stage of the analysis is to produce $S(Q)$ which is saved as the *S(Q) file*. However, only the S(Q) file is used in the second stage of the analysis to produce the PDF. Note that each stage of the analysis is independent of the others, so long as the necessary input files are present. That is, to recalculate the PDF of a specimen, you do not have to

start the analysis from input file; instead, you can specify the correct S(Q) file and the analysis will immediately create the PDF.

A.4.1.1 Launching PDFgetX

You can start Yorick from any directory by typing **yorick** at the prompt. At the Yorick prompt, type **pdfgetx** and Yorick should begin executing PDFgetX.

```
current directory: > yorick
 Copyright (c) 1996.  The Regents of the University of California.
 All rights reserved.  Yorick 1.4 ready.  For help type 'help'

> pdfgetx
```

Then, this is what you should see:

```
Pair Distribution Function from the X-ray powder diffraction (PDFgetX 1.1)

0) Preliminary data reduction
1) Build a setup file
2) Background Substraction
3) Reduction of Structure Function: S(Q)
     Input file format : (Q, I, dQ, dI)
4) PDF calculation :
     Input file format : (Q, S(Q), dQ, dS)
P) Print, S) Save, U) Unzoom, L) Limits windows
Q) Quit

[0-4 hlqpu]
```

This is the main menu, and Section 5 will explain the menu in detail.

A.4.1.2 Exiting PDFgetX

To quit PDFgetX, type "q" at the main menu prompt. This will exit PDFgetX but leave you still in Yorick. Type "quit" to exit Yorick.

```
[0-4 hlqpu] q

Exiting (PDFgetX 1.1):
> quit

current directory: >
```

A.4.1.3. The Main Menu

```
Pair Distribution Function from the X-ray powder diffraction (PDFgetX 1.1)

0) Preliminary data reduction
1) Build a setup file
2) Background Substraction
3) Reduction of Structure Function: S(Q)
     Input file format : (Q, I, dQ, dI)
4) PDF calculation :
     Input file format : (Q, S(Q), dQ, dS)
P) Print, S) Save, U) Unzoom, L) Limits windows
Q) Quit

[0-4 hlqpu]
```

The main menu provides you with several options. Simply type the number or letter of the option you want and hit "Enter".

Option 0: This will access an interactive routine that can extract scan(s) from raw SPEC data and MCA data acquired from x-ray powder diffraction experiments. Correction for detector and monitor dead-time correction can be applied. You can also compare variables(e.g. elastic) in each scan and combine scans to get average value.

Option 1: This will access an interactive routine used to create a setup file describing the conditions of your experiment. The setup file is needed at several stages in the analysis; PDFgetX will prompt for the name of the setup file at the appropriate points.

Option 2: This will access an interactive routine that can subtract a background from a PDFgetX input file.

Option 3: This will access an interactive routine that applies most of the corrections to the data and produces $S(Q)$. Those corrections requiring feedback from the user will prompt for the necessary information.

Option 4: This will access an interactive routine that calculates the PDF from $S(Q)$.

Option P: When there is a Yorick window present on your screen, you may select this option to print the contents of the window. When prompted, specify the number of the window (this number should be visible in the title bar of the window. "Yorick 3" would indicate a window number of 3.). This option is only available from

the main menu, which means that printing is not possible while doing the analysis.

Option S: This option save the specified window as postscript (PS) file or windows meta file (WMF) in your directory instead of sending figure to printer.

Option U: This UN-zooms a window. Yorick permits zooming on a data window (left-button zooms, right-button UN-zooms, and middle-button drags. You may also click on one axis only to zoom or unzoom that axis.) but sometimes it is difficult to make the window look the way it did before the zooming. In that case, select this option and, when prompted, specify the window number to unzoom the window. Unzooming only returns the window to the state it was in before the mouse-based zooms; manually-specified axis limits (option L) supersede the effects of this option.

Option L: This allows you to manually specify the axis limits for a given window. Enter the window number when prompted.

A.4.2 Data Analysis Procedure in PDFgetX

The Figure A.6 shows schematic diagram of data analysis procedure in PDFgetX. The procedure is composed of four main blocks, "Preliminary Data Reduction", "Build PDFgetX input file", "Refine Structure Function", and "PDF Calculation". Since most processes in the main blocks are already explained in the tutorial chapter, we will not repeat the explanation for the whole process. Instead, we'll give explanation for the refinement process in detail.

In order to obtain the structure function, we need to apply five major corrections; dead-time, multiple scattering, polarization, absorption, and Compton scattering corrections. In these corrections, dead-time correction will be applied in the preliminary data reduction. All other corrections will be applied during structure function analysis. The Figure A.7 shows flow chart of structure function analysis process. During the analysis process, the program asks input if it is necessary so please beware of the messages on the screen.

A.4.3 History File

During data reduction, PDFgetX records all the experimental information, parameters used for corrections, intermediate correction results to a binary file. The default file name is "_history.pdb". You can look at the content of this file using Yorick command.

```
> o = openb("_history.pdb")
> show, o
```

PDFgetX Data Analysis Procedure
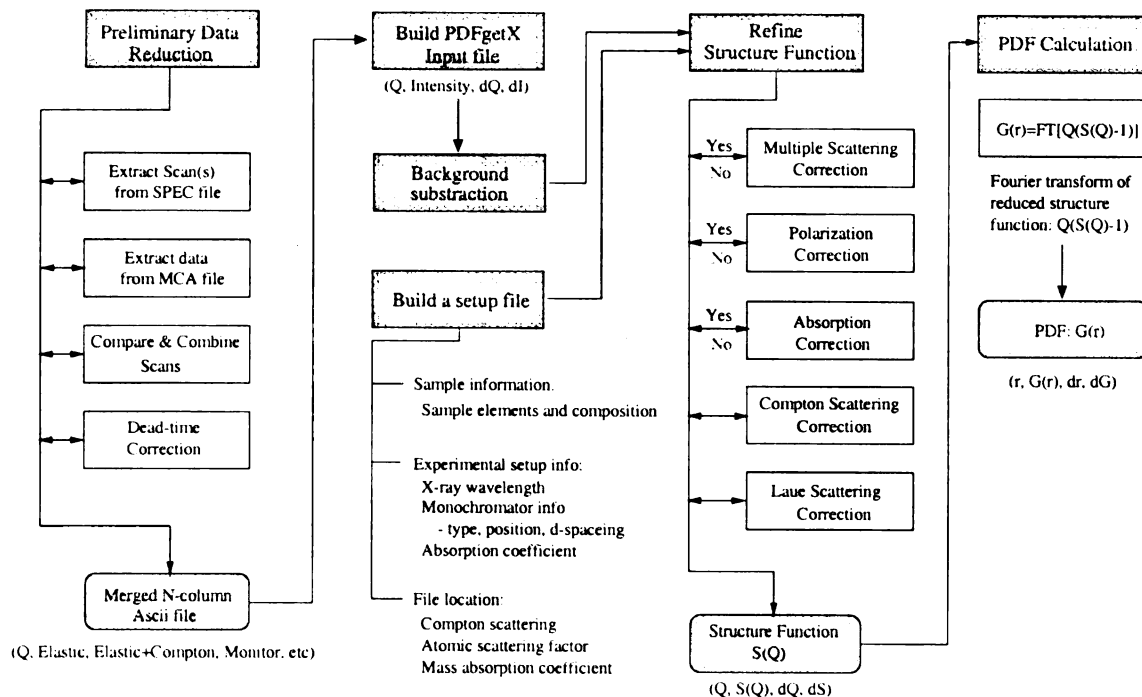
Figure A.6: Data analysis procedure in PDFgetX

```
37 non-record variables:
                   R              date                  nc
                   Z           deg_pol                  pf
             absflag          dis_mono             polflag
                 aft            dstran            pos_mono
                  aw       elementsname                   q
            coh_data             f2ave         soq_process
               compo             fave2             rn_data
             compton             fpara      rn_data_cfcompt
         compton_hiq          geometry              smflag
            data_cfbg            lambda                 soq
          data_cfbgms          mabscoeff            typ_mono
         data_cfbgmspf          mscflag
       data_cfbgmspfabs            mut
>
```

For example, you can simply check your experimental geometry by typing

```
> o.geometry
"r" /* "r" means reflection geometry */
```

For a complete description of history file see Appendix App.b.

A.4.4 Some Yorick Information

This section describes some miscellaneous information regarding the operation of Yorick, within the context of PDFgetX.

At any time, you may stop the execution of PDFgetX by entering control-C. You may restart PDFgetX at any time. If PDFgetX, for some reason, crashes, you can simply restart PDFgetX from within Yorick. It will not usually be necessary to exit Yorick before restarting PDFgetX. You may zoom any Yorick window using a mouse. The left mouse button zooms in, the right mouse button zooms out, and the middle button can be used to drag (if you have a two-button mouse, use both the right and left buttons at the same time). Click on an individual axis to affect only that axis.

Analysis of Structure Function
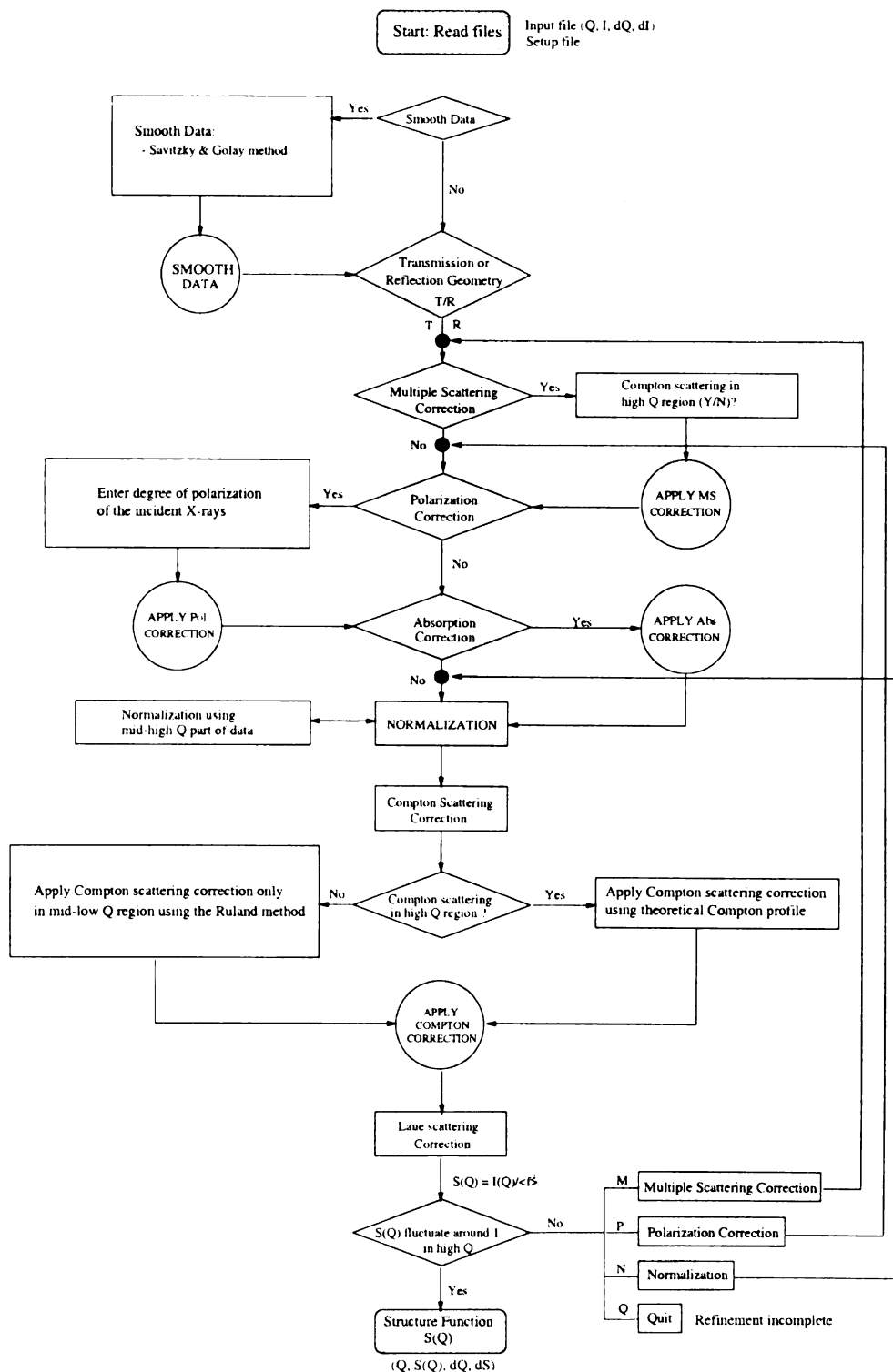
Figure A.7: Structure function analysis procedure in PDFgetX

114

A.5 Data Corrections

The measured X-ray diffraction intensity may be expressed [34] by

$$I^{mea}(Q) = PA[N(I_{eu}^{coh} + I_{eu}^{inc} + I_{eu}^{mul})], \qquad (A.1)$$

where P is the polarization factor, A the absorption factor, N normalization constant, and $I_{eu}^{coh}, I_{eu}^{inc}, I_{eu}^{mul}$ are the coherent, incoherent(Compton), and multiple scattering intensities, respectively, in electron units. We can define the structure function($S(Q)$) in the following form.

$$S(Q) = [I_{eu}^{coh} - (\langle f^2 \rangle - \langle f \rangle^2)]/\langle f \rangle^2 \qquad (A.2)$$

where $\langle f \rangle$ is the sample average scattering factor. Therefore to get a structure function, we have to do the following corrections [38] step by step on raw data.

```
0) Dead-time correction

1) Multiple scattering correction

2) Polarization correction

3) Absorption correction

4) Normalization

5) Compton scattering correction

6) Laue diffuse correction
```

A.5.1 Dead-Time Correction

In high-energy, high-intensity synchrotron x-ray diffraction experiments, the detector and monitor dead-time effect on the measured experimental data is rather lager. Therefore in these experiments, proper dead-time correction should be applied before applying standard corrections.

In the PDFgetX, the dead-time effect can be corrected by measuring detector dead-time and using the following Eq. A.3.

$$N_{dtc} = \frac{N_m}{\left(1 - \frac{\tau * N_{tot}}{t_o}\right)}$$ (A.3)

where τ is dead-time of detector or monitor, N_{dtc} the dead time corrected counts, N_m the measured counts, N_{tot} the total counts of detector or monitor and t_o the measuring time for each data point. Or dead-time effect can be corrected using the pulser method [106]. A pulser-train from an electronic pulser of known frequency can be fed into the detector preamp. The measured counts in the pulser signal in an SCA window set on the pulser signal is then recorded for each data point. The data dead-time correction is then obtained by scaling the raw data by the ratio of the known pulser frequency and the measured pulser counts. The Figure A.8 shows a comparison of dead-time correction using these two methods.

A.5.2 Multiple Scattering Correction

We'll consider here only the double scattering process since it represents the major part of the multiple scattering. To calculate double scattering ratio, we followed the method suggested by Warren and Mozzi [36]. According to Warren and Mozzi, the double scattering ratio is given by Eq. A.4

$$\frac{I(2)}{I(1)} = \frac{B^2 Q_M(2\theta, a, b, \mu t)}{J(2\theta) \sum_{i=1} A_i \mu_i(m)}$$ (A.4)

where, $B = \sum_i Z_i^2$ and A_i, $\mu_i(m)$ are the atomic weights and mass absorption coefficients of the atoms. And $J(2\theta)$ is an approximate representation for independent scattering, $\sum_i f_i^2$ or $\sum_i [f^2 + i(M)]_i$ depending on whether the measurements include only the coherent scattering or both the coherent and incoherent scattering and given in Eq. A.5.

$$J(2\theta) = B(a + \frac{1-a}{1 + b \sin^2 \theta})$$ (A.5)

where, a, b are parameters and can be obtained by fitting $J(2\theta)$ to either $\sum_i f_i^2$ or $\sum_i [f^2 + i(M)]_i$. Q_M is a complicated function depending on Q, μt, fitting parameters a and b and geometry. For details, refer to the papers by Dwiggins Jr. [107, 108]. As you can see in Figure A.9, the multiple scattering depends on absorption coefficient and geometry. In transmission geometry it becomes larger as Q increases. In reflection geometry, however, it increases up to maximum point and decrease a little bit after that. We can see that smaller the absorption coefficient, smaller double scattering ratio, in both cases [109].
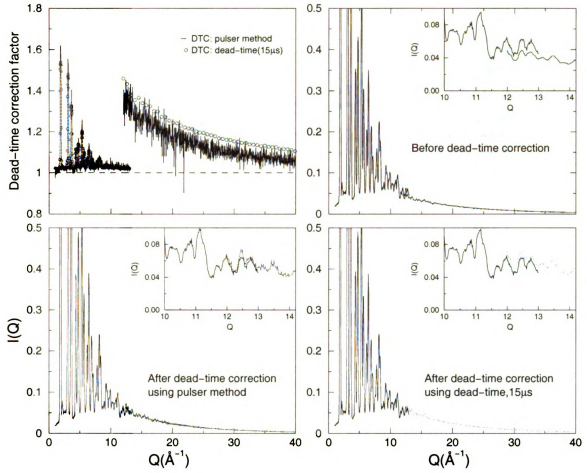
Figure A.8: Dead-time correction in $In_{0.33}Ga_{0.67}As$ semiconductor alloy: (a) Comparison between the dead-time correction using the pulser method and dead-time (15 μs) measurement. Comparison between low Q and high Q elastic scattering: (b) before dead-time correction. Low Q data don't overlap with the high Q data at Q=12-13 Å^{-1}, (c) after dead-time correction using the pulser method, (d) after dead-time correction using the dead-time measurement. After dead-time correction in both cases, the low Q and high Q data overlaps with each other quite well.

A.5.3 Polarization Correction

Polarization factor P is given by the following Eqs. [34]:

(a) Using a filter

$$P = (1 + \cos^2 2\theta)/2 \qquad (A.6)$$

(b) Using a crystal monochromator

$$P = (1 + x \cos^2 2\theta)/(1 + y) \qquad (A.7)$$
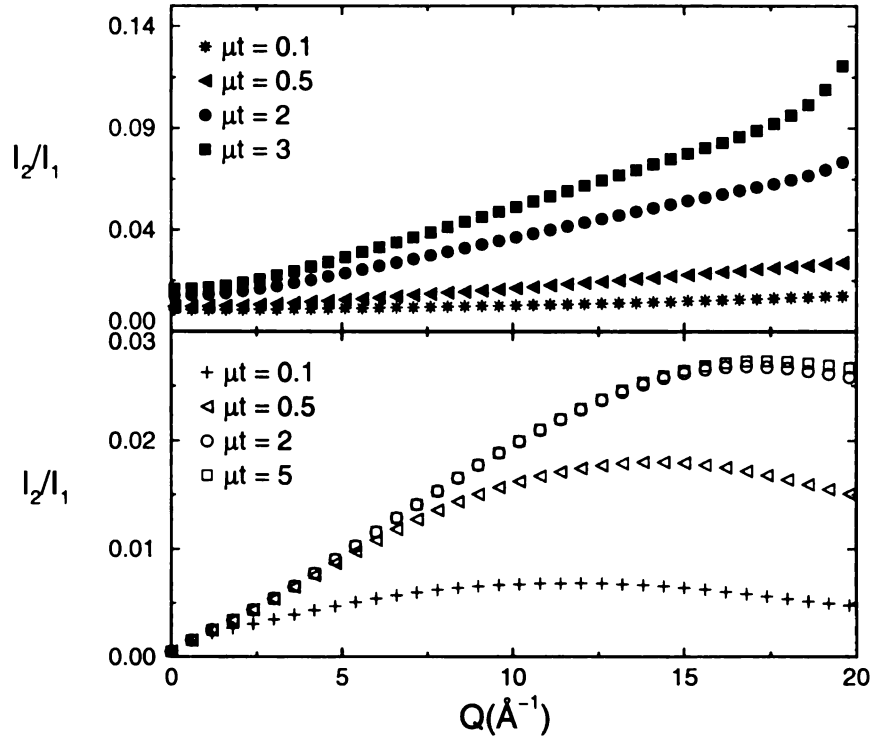
Figure A.9: Double Scattering Ratio in Ni, upper panel: transmission geometry, lower panel: reflection geometry, experimental data includes Compton scattering, wavelength of x-ray: 0.7107Å

where 2θ is the scattering angle, $x = \cos^2 2\alpha_c$ for a mosaic monochromator crystal or $x = \cos 2\alpha_c$ for a perfect monochromator crystal where $2\alpha_c$ is twice the Bragg angle of the monochromatic crystal. In Eq. A.7 $x = y$ when the monochromator is located in the incident beam, and $y = 1$ when the monochromator is set in the diffracted beam.

In the case of the sealed tube X-ray diffractometer, incident beam is unpolarized, so the full polarization correction should be applied. However, the Synchrotron X-ray radiation (e.g. CHESS) is almost perpendicularly polarized to the detector plane therefore only partial polarization correction is necessary, usually less than 5%.

A.5.4 Absorption Correction

Absorption factor A is given by the following Eqs. :

(a) Flat plate reflection geometry

$$A_{refl} = [1 - \exp(-2\,\mu\,t/\sin\theta]/2\,\mu \qquad (A.8)$$

118
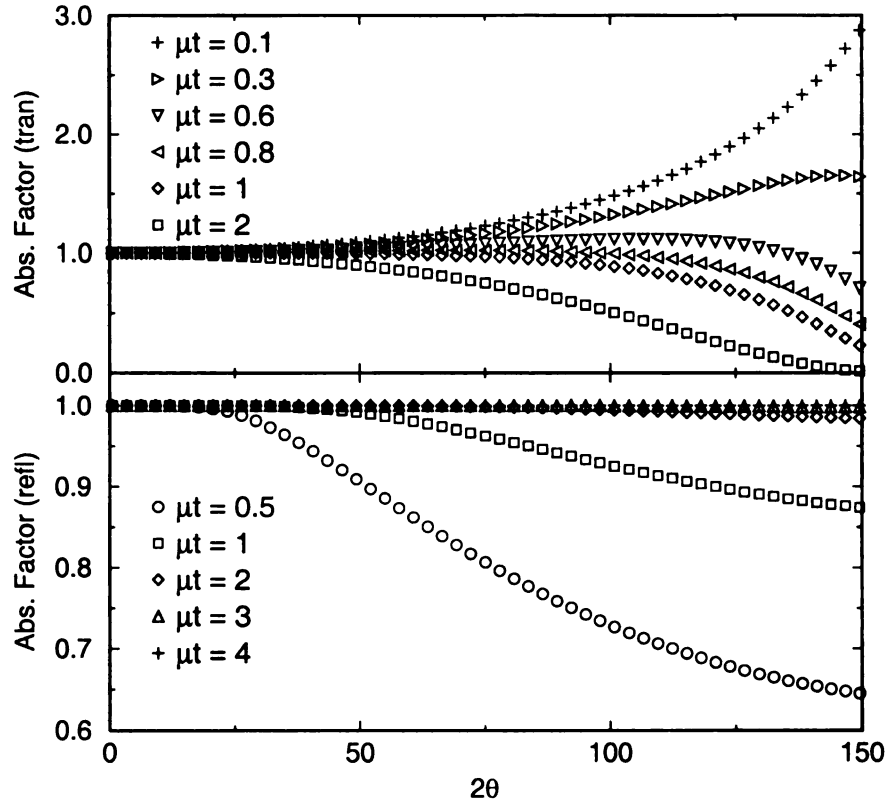
Figure A.10: Absorption Factor in transmission geometry (upper panel) and in reflection geometry (lower panel)

(b) Flat plate transmission geometry

$$A_{tran} = t \, \exp(-\mu \, t/\cos\theta)/\cos\theta \qquad (A.9)$$

Figure A.10 shows the absorption factor as function of angle and absorption coefficient. In reflection geometry, if the absorption coefficient is large enough ($\mu t \geq 4$), there's almost no angle dependence of absorption factor. In transmission geometry, however, when absorption coefficient is around '1', the angle dependence is minimal.

A.5.5 Compton Scattering Correction

Compton scattering correction is very important and difficult in X-ray diffraction data analysis. Figure A.11 shows elastic and Compton scattering. We can see that Compton scattering becomes much larger than coherent scattering in high Q. So even the small error in Compton correction causes big error in determining coherent scattering. Therefore it's better to discriminate Compton scattering from elastic

119
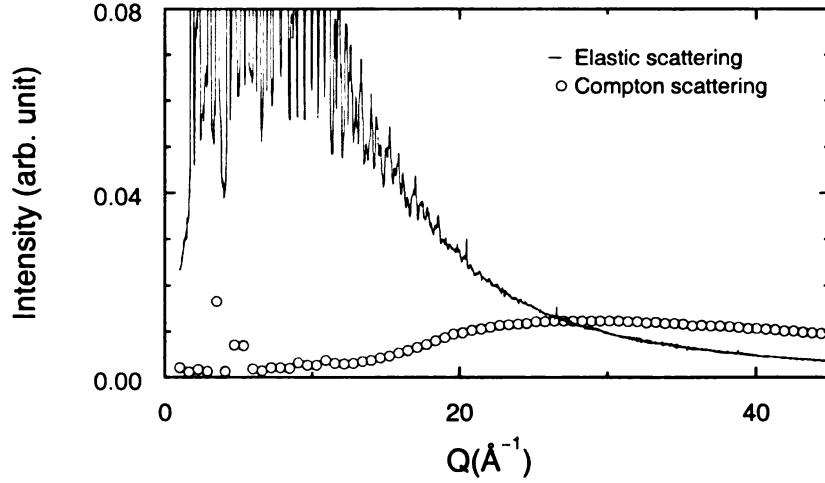
Figure A.11: Comparison between Compton and elastic scattering intensities measured in $In_{0.33}Ga_{0.67}As$. Above $Q=30\text{Å}^{-1}$, the Compton becomes larger than the elastic scattering.

scattering than to correct it theoretically. Compton scattering can be removed experimentally, particularly at large scattering angles, using an analyzer crystal in the diffracted beam, or using a solid state detector with a very narrow energy widow setup. When the Compton scattering is not discriminated, we have to use theoretical Compton profiles to apply correction. In this case we have to take into account the 'Breit-Dirac' recoil factor, R [110]. Formerly, R was usually set equal to unity, which is still an acceptable approximation for elements of high atomic number. For light elements and for present-day high-precision diffractometric measurement, however, it is essential that R be numerically evaluated if the maximum amount of information inherent in the experimental data is to be extracted. According to Ergun [110], the following Eq. A.10 should be applied when the *number of photons per unit area per unit time* is measured, as with counters.

$$R = (\frac{\lambda}{\lambda'})^2 = \frac{1}{(1 + \frac{2h}{mc}\frac{sin^2\theta}{\lambda})^2} \tag{A.10}$$

where λ and λ' are the wavelength of incident and Compton scattered beam. In this program, we use analytical Compton scattering formula [111] to calculate Compton profile. One can compare this results with theoretical Compton scattering data from the 'International tables for crystallography C' [112] and find the difference between these two are very small. Even when the Compton scattering in high Q is discriminated, the data still contains Compton in mid-low Q region. In order to remove the Compton in mid-low Q region, we use the method suggested by Ruland [113]. In this method, the Compton intensity in the data is smoothly attenuated with increasing Q as is shown in Figure A.4(c).

A.5.6 Normalization

The measured x-ray intensity is arbitrary value. The intensity should be normalized properly to get physical meaning. To determine normalization constant, N, we use high Q part of data. In this method, the normalization constant, N is defined in the following way.

$$N = \frac{\int_{Q_{mid}}^{Q_{max}} [\langle f^2 \rangle + I_{eu}^{inc}(Q)] \, dQ}{\int_{Q_{mid}}^{Q_{max}} [I^{cor}(Q)] \, dQ} \tag{A.11}$$

In Eq. A.11, I^{cor} corresponds to the data after corrections for background, multiple scattering, polarization, and absorption. The theoretical atomic scattering factor is calculated using the analytical formula suggested by D. Waasmaier & A. Kirfel [54].

A.5.7 Laue Scattering Correction

Laue term is defined as $\langle f^2 \rangle - \langle f \rangle^2$. The Laue scattering occurs when there is no short-range order and the atoms are distributed randomly and it decreases monotonically with increasing scattering angle [36].

A.5.8 Pair Distribution Function

The atomic Pair Distribution Function(PDF), $G(r)$, can be obtained from powder diffraction data through a sine Fourier transform:

$$G(r) = 4 \pi r \left[\rho(r) - \rho_o \right] = \frac{2}{\pi} \int_0^\infty Q \left[S(Q) - 1 \right] \sin (Qr) \, dQ \tag{A.12}$$

where $\rho(r)$ is the microscopic pair density, ρ_o is the average number density, and Q is the magnitude of the scattering vector. The PDF is a measure of the probability of finding an atom at a distance r from another atom and gives information about both average and the local structure of materials. For more about PDF analysis method, look up the papers by Egami, Toby and Billinge [40, 48, 114].

A.5.9 Error Propagation

In most diffraction experiments, the measured diffraction intensities are subject to statistical fluctuations. It is known that the detection process is well represented by the Poisson distribution. According to Poisson distribution, the standard deviation of statistical fluctuations is given by $\sqrt{N}$ for the measured N counts. This error in measured intensities will be propagated to the error in a function(e.g. PDF)

determined from these measured intensities. The estimated error in PDF will be used to test the quality of modeling. In general, an error in function $f(x_1, \ldots, x_n)$ can be calculated by the following Eq.

$$\delta f = \sqrt{\left(\frac{\partial f}{\partial x_1} \delta x_1\right)^2 + \cdots + \left(\frac{\partial f}{\partial x_n} \delta x_n\right)^2} \qquad (A.13)$$

The error in the Structure function, S(Q), is estimated by propagating error in the measured intensities through each correction step. For the calculation of error in G(r), the following Eq. is used [114].

$$\sigma_{G(r)} = \frac{2}{\pi} \sum_k \sigma_{S(Q_k)} Q_k \, \Delta Q_k \, \sin Q_k r \qquad (A.14)$$

App.a SPEC file format

In this appendix, the SPEC file format used in the data analysis is presented. The following shows sample SPEC file.

```
#F in33_tutorial.spec
#S 1   ascan   pmQ 1 13   600 1
#D Fri Sep 18 16:13:55 1998
#T 1   (Seconds)
#L pmQ ereal elive Epoch Seconds IC1 IC3 I_CESR PULSER TOTAL COMPTON IC2 ELASTIC
1   2.07 1.967 75931 2.11758 556914 396634 394.395 416 2866 233 31718 606
1.02   2.07 1.968 75934 2.11849 558523 396548 394.159 432 3000 217 31791 610
1.04   2.06 1.962 75936 2.10892 555188 394768 392.324 414 3030 253 31569 591
1.06   2.07 1.969 75939 2.11886 558933 396616 394.023 417 3138 240 31776 647
1.08   2.07 1.977 75942 2.1189 559126 396636 393.919 419 2923 246 31839 639

#S 2   ascan   pmQ 1 13   600 1
#D Fri Sep 18 16:40:55 1998
#L pmQ ereal elive Epoch Seconds IC1 IC3 I_CESR PULSER TOTAL COMPTON IC2 ELASTIC
1   2.07 1.999 77606 2.11876 490517 396566 353.616 418 2397 186 27129 533
1.02   2.069 1.997 77609 2.11807 490872 396438 353.319 415 2486 194 27167 558
1.04   2.07 1.989 77612 2.11884 489377 396583 353.419 416 2672 177 27045 536
1.06   2.07 1.996 77614 2.11884 492200 396585 353.414 428 2551 195 27218 551
1.08   2.06 1.989 77617 2.10866 488500 394682 351.707 419 2458 199 26993 550

#S 3   ascan   pmQ 12 40   1400 1
#L pmQ ereal elive Epoch Seconds IC1 IC3 I_CESR PULSER TOTAL COMPTON IC2 ELASTIC
12   2.07 1.115 88417 2.11861 633382 399154 451.721 317 44519 7243 634757 29557
12.02   2.06 1.137 88419 2.1088 628412 397322 449.505 313 43218 7290 630504 28163
12.04   2.07 1.166 88422 2.11877 625842 399215 451.612 327 42631 7336 630216 27395
12.06   2.07 1.185 88425 2.11884 624286 399227 451.478 299 41732 7166 629057 26469
```

As shown in the sample SPEC file, all the comments and characters start with # mark. To specify scan number #S is used and for the scan header, #L and so on. To separate scans blank line is used. Except these things the SPEC file is the same as the multi-column ascii file.

App.b Description of the history file

In this appendix, the content of the history file ("_history.pdb") is described. The history file contains all the experimental information, parameters used for corrections, intermediate correction results.

Parameter	Description
elementsname	Name of sample elements ; Ex. ["In", "Ga", "As"]
Z	Atomic number of sample elements ; Ex. [49,31,33]
compo	Composition of sample ; Ex. [0.33,0.67,1]
aw	Atomic weight of sample elements ; Ex. [114.82, 69.72, 74.92]
mabscoeff	Mass absorption coefficient of sample elements at wavelength λ Ex. [6.36, 1.88, 2.23] for λ=0.2078 Å
lambda	Wavelength of incident X-ray Ex. [0.2078] for E = 60 KeV X-ray radiation
mut(μt)	Absorption coefficient*sample thickness ;
geometry	Configuration of diffractometer r=Reflection geometry t=Transmission geometry
mscflag	0=No multiple scattering correction 1=Multiple scattering correction
mscParam	mscflag = 1: fpara, dsrefl, dstran fpara=parameters used to approximate scattering in function J (Warren & Mozzi, 1996) dsrefl=double scattering ratio, I2/I1 in reflection geometry dstran=double scattering ratio, I2/I1 in transmission geometry
polflag	0=No polarization correction 1=Polarization correction
polParam	polflag = 1: pos_mono, typ_mono, dis_mono, deg_pol, pf pos_mon : Position of Monochromator inc=Primary beam Monochromator ref=Diffracted beam Monochromator typ_mono : Type of Monochromator pc=Perfect crystal monochromator mc=Perfect crystal monochromator dis_mono : Distance between crystal plane Ex. Graphite(002), d = 3.3570 Å, Si(111), d = 3.135 Å deg_pol : Degree of polarization of incident X-ray beam Synchrotron source $\Rightarrow$ 1, X-ray tube $\Rightarrow$ 0 pf = polarization factor

124

absflag	0=No absorption correction
	1=Absorption correction
absParam	absflag = 1: afr, aft, mut(μt)
	aft=absorption factor in transmission geometry
	afr=absorption factor in reflection geometry
smflag	0=No smoothing of data
	1=Smoothing using the Savitzky-Golay filter
smoothParam	smflag = 1: q_s, num_ps
	q_s = starting point of smoothing
	num_ps = number of point used in Savitzky-Golay filter
compton_hiq	Y= contain Compton scattering in high Q region of data
	N= Compton in high Q is discriminated; no Compton in high Q
comptonParam	compton_hiq = N : integral_width, wf
	integral_width = control parameter for a width of window function
	wf = Ruland window function
nc	normalization constant
R	Breit-Dirac Recoil Factor
soq_process	0=S(Q) reduction process incomplete, no S(Q) obtained
	1=S(Q) reduction process completed, S(Q) obtained
date	Date of refinement
f2ave	$\langle f^2 \rangle$, sample average of square of scattering factor
fave2	$\langle f \rangle^2$, square of sample average of scattering factor
compton	Theoretical Compton scattering
q	Q (=4π sin(θ)/λ) array
data_cfbg	Data after background correction
data_cfbgms	Data after multiple scattering correction
data_cfbgmspf	Data after multiple scattering & polarization correction
data_cfbgmspfabs	Data after multiple scattering, polarization & absorption correction
rn_data	Normalized data after all necessary corrections
rn_data_cfcompt	Data corrected for Compton scattering after normalization
coh_data	Coherent scattering data
soq	Structure function

App.c MCA file format

In this appendix, the MCA file format used in the data analysis is presented. The MCA file format used in this manual is two column ascii file as shown in the following Figure A.12. The correspond MCA spectrum is shown in Figure A.2. The first column corresponds to the MCA channel number which starts from 0 to 1023 in this case (so total MCA channel $\#$ = 1024). And the second column is the intensity detected at each channel. Each 1024 lines corresponds to one Q value and separated by the blank line. Therefore to convert MCA file to N-column ascii file, the following information is needed; total MCA channel number and the corresponding "Q" column. You can get the "Q" column from the corresponding scan (saved in SPEC file) or you can generate "Q" column if it has constant step. In this case you need Q_{min} of your scan, total number of points in your scan, and Q step.

MCA channel	Intensity	
0	0	
1	0	
2	0	
.	.	
.	.	
.	.	
600	23	
601	34	
602	15	
603	65	Q(i)
604	34	
605	22	
.	.	
.	.	
.	.	
1020	0	
1021	0	
1023	0	

blank line

0	0	
1	0	
2	0	
.	.	
.	.	
600	23	
601	34	
602	15	
603	65	Q(i+1)
604	34	
605	22	
.	.	
.	.	
.	.	
1020	0	
1021	0	
1023	0	

blank line

0	0	
1	0	
2	0	
.	.	
.	.	
600	23	
601	34	
602	15	
603	65	Q(i+2)
604	34	
605	22	
.	.	
.	.	
.	.	
1020	0	
1021	0	
1023	0	

Figure A.12: MCA file format

Bibliography

[1] A. M. Glass, **Optical Materials**, Science **235**, 1003 (1985).

[2] W. Potzel, M. Steiner, H. Karzel, W. Schiessl, M. Köfferlein, and G. M. Kalvius, **Electronically Driven Soft Modes in Zinc Metal**, Phys. Rev. Lett. **74**, 1139 (1995).

[3] K. Einarsodotter, B. Sadigh, G. Grimvall, and V. Ozolinš, **Phonon Instabilities in fcc and bcc Tungsten**, Phys. Rev. Lett. **79**, 2073 (1997).

[4] P. Brüesch, **Phonons: Theory and Experiments II**, Springer-Verlag, Berlin, 1986.

[5] S. J. L. Billinge, **Real-Space Rietveld: Full Profile Structure Refinement of the Atomic Pair Distribution Function**, in *Local Structure from Diffraction*, edited by S. J. L. Billinge and M. F. Thorpe, page 137, New York, 1998, Plenum.

[6] T. Egami, S. J. L. Billinge, S. Kycia, W. Dmowski, and A. S. Eberhardt, **Information stored in high Q-space: role of high energy scattering**, Unpublished.

[7] J. C. Phillips, **Bonds and Bands in Semiconductors**, Academic Press, 1973.

[8] P. Y. Yu and M. Cardona, **Funcamentals of Semiconductors: Physics and Materials Properties**, Springer, Berlin, 1996.

[9] N. W. Ashcroft and M. D. Mermin, **Solid State Physics**, chapter 28, 29, Saunders College Publishing, 1976.

[10] K. Seeger, **Semiconductor Physics: An Introduction**, Springer-Verlag, Berlin, 1985.

[11] M. Jaros, **Electronic properties of semiconductor alloy systems**, Rep. Prog. Phys. **48**, 1091 (1985).

[12] A.-B. Chen and A. Sher, **Semiconductor Alloys: Physics and Materials Engineering**, Plenum Press, New York, 1995.

[13] S. Takeuchi and K. Suzuki, **Stacking Fault Energies of Tetrahedrally Coordinated Crystals**, phys. Stat. sol. (a) **171**, 99 (1999).

[14] V. Ozoli and A. Zunger, **Theory of Systematic Absence of NaCl-Type (β-Sn-Type) High Pressure Phases in Covalent (Ionic) Semiconductors**, Phys. Rev. Lett. **82**, 767 (1999).

[15] Mikkelson and J. B. Boyce, **Extended X-ray-absorption fine-structure study of** $Ga_{1-x}In_xAs$ **random solid solution**, Phys. Rev. B **28**, 7130 (1983).

[16] R. Asokamani, R. M. Amirthakumari, R. Rita, and C. Ravi, **Electronic structure calculations and physical properties of ABX$_2$ (A=Cu, Ag; B=Ga, In; X=S, Se, Te) ternary chalcopyrite systems.**

[17] V. Swaminathan, **Encyclopedia of Applied Physics**, volume 17, chapter Semiconductors, Compound-Material Properites, page 335, VCH Publishers, Inc., 1996.

[18] V. Narayanamurti, **Artificially Structured Thin-Film Materials and Interfaces**, Science **235**, 1023 (1985).

[19] D. Paul, **Silicon germanium makes its mark**, Physics World , Feb. 27 (2000).

[20] M. F. Ling and D. J. Miller, **Band structure of semiconductor alloys**, Phys. Rev. B **38**, 6113 (1988).

[21] S. N. Ekpenuma, C. W. Myles, and J. R. Gregg, **Alloy disorder effects on the electronic properties of III-V quaternary semiconductor alloys**, Phys. Rev. B **41**, 3582 (1990).

[22] W. L. Bragg, Philos. Mag. **40**, 169 (1920).

[23] L. Pauling, **The nature of the Chemical Bond**, Cornell Univ. Press, Ithaca, 1967.

[24] J. C. Woolley, **Compound Semiconductors**, page 3, Reinhold Publishing Corp., New York, 1962.

[25] J. C. Mikkelson and J. B. Boyce, **Atomic scale structure of random solid solutions: extended x-ray-absorption fine-structure study of $Ga_{1-x}In_xAs$**, Phys. Rev. Lett. **49**, 1412 (1982).

[26] Y. Cai and M. F. Thorpe, **Length mismatch in random semiconductor alloys. II. Structural characterization of pseudobinaries**, Phys. Rev. B **46**, 15879 (1992).

[27] A. Balzarotti, N. Motta, A. Kisiel, M. Zimnal-Starnawska, M. T. Czyżyk, and M. Podgórny, **Model of the local structure of random ternary alloys: experiment vs. theory**, Phys. Rev. B **31**, 7526 (1985).

[28] J. B. Boyce and J. C. Mikkelson, **Local structure of pseudobinary semiconductor alloys: An x-ray absorption fine structure study**, J. Crys. Grow. **98**, 37 (1989).

[29] Z. Wu, K. Lu, Y. Wang, J. Dong, H. Li, C. Li, and Z. Fang, **Extended x-ray-absorption fine-structure study of $GaAs_xP_{1-x}$ semiconducting random solid solutions**, Phys. Rev. B **48**, 8694 (1993).

[30] J. S. Chung and M. F. Thorpe, private communication.

[31] I.-K. Jeong, Th. Proffen, F. Mohiuddin-Jacobs, and S. J. L. Billinge, **Measuring correlated atomic motion using x-ray diffraction**, J. Phys. Chem. A **103**, 921 (1999).

[32] R. Kaplow, B. L. Averbach, and S. L. Strong, **Pair Correlations in Solid Lead Near the Melting Temperature**, J. Phys. Chem. Solids **25**, 1195 (1964).

[33] R. Kaplow, S. L. Strong, and B. L. Averbach, **Radial Density Functions for Liquid Mercury and Lead**, Phys. Rev. **138**, 1336 (1965).

[34] Y. Waseda, **The structure of non-crystalline materials**, McGraw-Hill, New York, 1980.

[35] S. R. Elliott, **Physics of Amorphous Materials**, Longman Scientific & Technical, second edition, 1990.

[36] B. E. Warren, **X-Ray Diffraction**, Dover, New York, 1990.

[37] H. P. Klug and L. E. Alexander, **X-RAY DIFFRACTION PROCEDURES**, A Wiley-Interscience Publication, 1974.

[38] C. N. J. Wagner, **Direct methods for the determination of atomic-scale structure of amorphous solids (x-ray, electron, and neutron scattering)**, J. Non-cryst. Solid **31**, 1 (1978).

[39] S. J. L. Billinge, **Local Atomic Structure and Superconductivity of $Nd_{2-x}Ce_xCuO_{4-y}$: A Pair-Distribution-Function Study**, PhD thesis, Univ. Pennsylvania, 1992.

[40] S. Billinge and M. F. Thorpe, editors, **Local Structure from Diffraction**, Plenum, New York, 1998.

[41] V. Petkov, I-K. Jeong, J. S. Chung, M. F. Thorpe, S. Kycia, and S. J. L. Billinge, **High real-space resolution measurement of the local structure of $Ga_{1-x}In_xAs$ using x-ray diffraction**, Phys. Rev. Lett. **83**, 4089 (1999).

[42] E. S. Božin, S. J. L. Billinge, H. Takagi, and G. H. Kwei, **Neutron diffraction evidence of microscopic charge inhomogeneities in the CuO_2 plane of superconducting $La_{2-x}Sr_xCu_4$ ($0 \leq x \leq 0.30$)**, Phys. Rev. Lett. **84**, 5856 (2000).

[43] S. J. L. Billinge, R. G. DiFrancesco, G. H. Kwei, J. J. Neumeier, and J. D. Thompson, **Direct Observation of Lattice Polaron Formation in the Local Structure of $La_{1-x}Ca_xMnO_3$**, Phys. Rev. Lett. **77**, 715 (1996).

[44] J. I. Langford and D. Louër, **Powder Diffraction**, Rep. Prog. Phys. **59**, 131 (1996).

[45] H. M. Rietveld, **A profile refinement method for nuclear and magnetic structure**, Jour. Appl. Cryst. **2**, 65 (1969).

[46] F. Frey, **Diffuse scattering from periodic and aperiodic crystals**, Z. Kristallogr. **212**, 257 (1997).

[47] G. E. Ice and C. J. Sparks, **Modern resonant x-ray studies of alloys: Local Order and Displacements**, Annu. Rev. Mater. Sci. **29**, 25 (1999).

[48] T. Egami, **PDF Analysis Applied to Crystalline Materials**, in *Local Structure from Diffraction*, edited by S. J. L. Billinge and M. F. Thorpe, page 1, New York, 1998, Plenum.

[49] P. Debye, Ann. Physik **46**, 809 (1915).

[50] J. Chung and M. F. Thorpe, **Local atomic structure of semiconductor alloys using pair distribution function**, Phys. Rev. B **55**, 1545 (1997).

[51] V. Petkov, I-K. Jeong, F. Mohiuddin-Jacobs, Th. Proffen, and S. J. L. Billinge, **Local structure of $In_{0.5}Ga_{0.5}As$ from joint high-resolution and differential pair distribution function analysis**, J. Appl. Phys. **88**, 665 (2000).

[52] A. Bienenstock, **Introduction to the application and limits of anomalous x-ray diffraction in the determination of partial structure factors**, in *Methods in the determination of partial structure factors of disordered matter by neutron and anomalous x-ray diffraction*, edited by J. B. Suck, D. Raoux, P. Chieux, and C. Riekel, page 123, Singapore, 1992, World Scientific.

[53] G. E. Ice, C. J. Sparks, and L. B. Shaffer, **Chemical and displacement atomic pair correlations in crystalline solid solution recovered by resonant (anomalous) x-ray scattering**, in *Resonant anomalous x-ray scattering*, edited by G. Materlik, G. J. Sparks, and K. Fischer, page 256, North-Holland, 1994.

[54] D. Waasmaier and A. Kirfel, **New Analytical Scattering Factor Functions for Free Atoms and Ions for Free Atoms and Ions**, Acta Cryst. A **51**, 413 (1995).

[55] P. Eisenberger, **A 6-GeV Storage Ring - An Advanced Photon Research Facility**, Science **231**, 687 (1986).

[56] K. Laaziri, J. L. Robertson, S. Roorda, M. Chicoine, S. Kycia, J. Wang, and S. C. Moss, **Quantitative treatment for extracting coherent elastic scattering from X-ray scattering experiments**, Jour. Appl. Cryst. **32**, 322 (1999).

[57] I.-K. Jeong, J. Thompson, Th. Proffen, and S. J. L. Billinge, **PDFgetX, a program for obtaining the atomic pair distribution function from x-ray powder diffraction data**, http://www.pa.msu.edu/cmp/billinge-group/programs/PDFgetX.html; submitted .

[58] ftp://wuarchive.wustl.edu/languages/yorick/yorick-ad.html .

[59] M. Schwoerer-Böhning, A. T. Macrander, and D. A. Arms, **Phonon Dispersion of Diamond Measured by Inelastic X-ray Scattering**, Phys. Rev. Lett. **80**, 5572 (1998).

[60] T. Ruf, J. Serrano, M. Cardona, P. Pavone, M. Pabst, M. Krisch, M. D'Astuto, T. Suski, I. Grzegory, and M. Leszczynski, **Phonon Dispersion Curves in Wurtzite-Structure GaN Determined by Inelastic X-Ray Scattering**, Phys. Rev. Lett. **86**, 906 (2001).

[61] M. Holt, Z. Wu, H. Hong, P. Zschack, P. Jemian, J. Tischler, H. Chen, and T.-C. Chiang, **Determination of Phonon Dispersions from X-Ray Transmission Scattering: The Example of Silicon**, Phys. Rev. Lett. **83**, 3317 (1999).

[62] C. H. Booth, F. Bridges, E. D. Bauer, G. G. Li, J. B. Boyce, T. Claeson, C. W. Chu, and Q. Xiong, **XAFS measurements of negatively correlated atomic displacements in $HgBa_2CuO_{4+\delta}$**, Phys. Rev. B **52**, R15 745 (1995).

[63] R. Lagneborg and R. Kaplow, **Radial Distribution Function in Solid Cobalt**, Acta Metall. **15**, 13 (1967).

[64] Th. Proffen and S. J. L. Billinge, **PDFFIT, a program for full profile structural refinement of the atomic pair distribution function**, J. Appl. Crystallogr. **32**, 572 (1999).

[65] J. M. Ziman, **Principles of the Theory of Solids**, Cambridge University Press, Cambridge, U. K., 1973.

[66] M. F. Thorpe, J. S. Chung, S. J. L. Billinge, and F. Mohiuddin-Jacobs, **Advances in Pair Distribution Profile Fitting in Alloys**, in *Local Structure from Diffraction*, edited by S. J. L. Billinge and M. F. Thorpe, page 157, New York, 1998, Plenum.

[67] J. G. Kirkwood, J. Chem. Phys. **7**, 506 (1939).

[68] M. F. Thorpe, private communication.

[69] G. Beni and P. M. Platzman, **Temperature and polarization dependence of extended x-ray absorption fine-structure spectra**, Phys. Rev. B **14**, 1514 (1976).

[70] E. Sevillano and H. Meuth, **Extended x-ray absorption fine structure Debye-Waller factors. I. Monatomic crystals**, Phys. Rev. B **20** (1979).

[71] H. L. Kharoo, O. P. Gupta, and M. P. Hemkar, **Angular forces and normal vibration in nickel**, Phys. Rev. B **19**, 2986 (1979).

[72] P. Pavone, Lattice Dynamics of Semiconductors from Density-Functional Perturbation Theory, PhD thesis, SISSA ISAS, 1991.

[73] J. L. Martins and A. Zunger, **Bond lengths around isovalent impurities and in semiconductor solid solutions**, Phys. Rev. B **30**, 6217 (1984).

[74] C. K. Shih, W. E. Spicer, W. A. Harrison, and A. Sher, **Bond-length relaxation in pseudobinary alloys**, Phys. Rev. B **31**, 1139 (1985).

[75] A.-B. Chen and A. Sher, **Semiconductor pseudobinary alloys: Bond-length relaxation and mixing enthalpies**, Phys. Rev. B **32**, 3695 (1985).

[76] M. C. Schabel and J. L. Martins, **Structural model for psuedobinary semiconductor alloys**, Phys. Rev. B **43**, 11,873 (1991).

[77] M. Podgorny, M. T. Czyzyk, A. Balzarotti, P. Letardi, N. Motta, A. Kisiel, and M. Zimnal-Starnawska, **Crystallographic structure of ternary semiconducting alloys**, Solid State Commun. **455**, 413 (1985).

[78] A. Sher, M. van Schilfgaarde, A.-B. Chen, and W. Chen, **Quasichemical approximation in binary alloys**, Phys. Rev. B **36**, 4279 (1987).

[79] W. Zhonghua and L. Kunquan, **Local structures in zincblende-type random solid solution**, J. Phys: Condens. Matter **6**, 4437 (1994).

[80] F. A. Cunnel and J. B. Schroeder, **Compound Semiconductors**, page 207 and 222, Reinhold Publishing Corp, New York, 1962.

[81] K. A. Jones, W. Porod, and D. K. Ferry, **Clustering in ternary III-V semiconductors**, J. Phys. Chem. Solids **44**, 107 (1983).

[82] P. A. Fedders and M. W. Muller, **Mixing enthalpy and composition fluctuations in ternary III-V semiconductor alloys**, J. Phys. Chem. Solids **45**, 685 (1984).

[83] A. S. Martins, B. Koiller, and R. B. Capa, **An elastic model for the In-In correlations in $In_xGa_{1-x}As$ semiconductor alloys**, Solid State Commun. **115**, 287 (2000).

[84] M. W. Muller and A. Sher, **Mesoscopic composition fluctuations in semiconductor alloys: Effect on infrared devices**, Appl. Phys. Lett. **74**, 2343 (1999).

[85] L. Bellaiche, S.-H. Wei, and A. Zunger, **Bond-length distribution in tetrahedral versus octahedral semiconductor alloys: The case of $Ga_{1-x}In_xN$**, Phys. Rev. B **56**, 13872 (1997).

[86] L. Vegard, Z. Phys. **5**, 17 (1921).

[87] M. R. Weidmann, J. R. Gregg, and K. E. Newman, **Local-Structure in $Zn_{1-x}Mn_xSs$ Alloys**, J. Phys: Condens. Matter **4**, 1895 (1992).

[88] Th. Proffen and R. Neder, **DISCUS a Program for Diffuse Scattering and Defect Structure Simulations - Update**, Jour. Appl. Cryst. **30**, 171 (1997).

[89] A. Silverman, A. Zunger, R. Kalish, and J. Adler, **Atomic-scale structure of disordered $Ga_{1-x}In_xP$ alloys**, Phys. Rev. B **51**, 10795 (1995).

[90] C. N. J. Wagner, **Direct methods for the determination of atomic-scale structure of amorphous solids (x-ray, electron and neutron scattering)**, J. Non-Crystalline Solids **31**, 1 (1978).

[91] J. C. Woicik, **Random-cluster calculation of bond lengths in strained-semiconductor alloys**, Phys. Rev. B **57**, 6266 (1998).

[92] J. S. Chung and M. F. Thorpe, **Local atomic structure of semiconductor alloys using pair distribution functions II**, Phys. Rev. B **59**, 4807 (1999).

[93] R. I. Barabash, J. S. Chung, and M. F. Thorpe, **Lattice and continuum theories of Huang scattering**, J. Phys: Condens. Matter **11**, 3075 (1999).

[94] F. Glas, C. Gors, and P. Henoc, **Diffuse scattering, size effect and alloy disorder in ternary and quaternary III-V compounds**, Phil. Mag. B **62**, 373 (1990).

[95] D. L. Bolloc'h, J. L. Robertson, H. Reichert, S. C. Moss, and M. L. Crow, **X-ray and neutron scattering study of Si-rich Si-Ge single crystals**, unpublished.

[96] F. Glas, **Correlated static atomic displacements and transmission-electron-microscopy contrast in compositionally homogeneous disordered alloys**, Phys. Rev. B **51**, 825 (1995).

[97] P. F. Peterson, Th. Proffen, I.-K. Jeong, S. J. L. Billinge, K. Choi, M. G. Kanatzidis, and P. G. Radaelli, **Local atomic strain in $ZnSe_{1-x}Te_x$ from high real space resolution neutron pair distribution function measurements**, Phys. Rev. B (2001), in press, cond-mat/0009364.

[98] Th. Proffen, **Analysis of Occupational and Displacive Disorder using the Atomic Pair Distribution Function: a Systematic Investigation**, Z. Krist. **215**, 661 (2000),

[99] G. S. Knapp, H. K. Pan, and J. M. Tranquada, Phys. Rev. B **32**, 2006 (1985).

[100] G. Dalba, P. Fornasini, F. Rocca, and S. Mobilio, **Correlation effects in the extended x-ray-absorption fine-structure Debye-Waller factors of AgI**, Phys. Rev. B **41**, 9668 (1990).

[101] J. M. Tranquada and C. Y. Yang, **EXAFS Measurements of bond-stretching force constants in arsenic and arsenic compounds**, Solid State Commun. **63**, 211 (1987).

[102] D. Dimitrov, D. Louca, and H. Röder, **Phonons from neutron powder diffraction**, Phys. Rev. B **60**, 6204 (1999).

[103] M. F. Thorpe, unpublished.

[104] C. T. Chantler, J. Phys. Chem. Ref. Data **24**, 71 (1995).

[105] R. L. McGreevy and L. Pusztai, Mol. Simul. **1**, 357 (1988).

[106] I.-K. Jeong, F. Mohiuddin-Jacobs, V. Petkov, and S. J. L. Billinge, **Local structure of $In_xGa_{1-x}As$ semiconductor alloys by high energy synchrotron x-ray diffraction**, Phys. Rev. B (2001), in press, cond-mat/0008079.

[107] C. W. Dwiggins, Jr and D. A. Park, **Calculation of the intensity of secondary scattering of x-rays by non-crystalline materials**, Acta Cryst. A **27**, 264 (1971).

[108] C. W. Dwiggins, Jr, **Calculation of the intensity of secondary scattering of x-rays by non-crystalline materials. II. Moving sample transmission geometry**, Acta Cryst. A **28**, 155 (1972).

[109] R. Serimaa, T. Pitkanen, S. Vahvaselka, and T. Paakkari, **Multiple scattering of x-rays in the case of isotropic samples**, Jour. Appl. Cryst. **23**, 11 (1990).

[110] S. Ergun, in *Chemistry and Physics of Carbon*, edited by J. P. L. Walker, chapter Vol. 3, pages 211–288, Marcel Dekker, New York, 1968.

[111] B. J. Thijsse, **The accuracy of experimental radial distribution functions for metallic glasses**, Jour. Appl. Cryst. **17**, 61 (1984).

[112] A. J. C. Wilson, editor, **International tables for crystallography**, volume C, Kluwer Academic Publishers, 1995.

[113] W. Ruland, **The separation of coherent and incoherent Compton x-ray scattering,**
Brit. J. Appl. Phys. **15,** 1301 (1964).

[114] B. H. Toby and T. Egami, **Accuracy of Pair Distribution Function Analysis Applied to Crystalline and Non-Crystalline Materials,** Acta Cryst. A **48,** 336 (1992).